Reliable Wind Turbine Control Design

A Study of Achievable Control Performance under Design Uncertainty

V. Pascu

June 2015
ECN-E–15-023

Abstract

Wind power has proven to be one of the most versatile forms of renewable energy. Similarly, offshore wind is currently emerging as the most promising method of meeting the global target for low cost of renewable energy production, given the massive potential of wind at sea. However, from the wind turbine design point of view, the requirement of having a low cost offshore plant implies both that the energy yield of the system is maximized and that the associated operational and maintenance costs are minimized over its entire lifespan. Control systems, while certainly required for safe wind turbine operation, can also help in addressing these challenges. Offshore wind turbines are especially subject to large variations of their physical parameters due to heavy environmental conditions and the pronounced passage of time. This report provides an overview of the research approach taken towards ensuring that wind turbine control system performance, while always affected by several introduced factors that cause deviations of the model parameters from their nominal values, remains in some sense optimal. An analysis of the extent to which typical control loops within a wind turbine control system are affected by design uncertainty is first presented; subsequently, an improved design problem is formulated based on the analysis results and solved within the framework of linear parameter-varying control theory; the presented design methodology for the formulated practical problem has the potential of reducing typical design safety factors considerably thus allowing for a decrease in wind turbine production costs by up to 9%. The document is concluded with several qualitative remarks and possibilities for further development resulting from the presented information.

Academic Research Review Committee:

dr. ir. Jan-Willem van Wingerden (Associate Professor, Delft Center for Systems and Control - TU Delft)
dr. ir. Stoyan Kanev (Senior Control Scientist and Project Manager, Wind Energy Unit - ECN)
dr. ir. Simone Baldi (Assistant Professor, Delft Center for Systems and Control - TU Delft)
ir. Yasin Gunes (PhD Researcher, Delft Center for Systems and Control - TU Delft)

Applied Research Review Committee:

dr. ir. Stoyan Kanev (Senior Control Scientist and Project Manager, Wind Energy Unit - ECN)
dr. Marc Langelaar (Group Manager, Wind Energy Unit - ECN)
ir. Aart van der Pal (Unit Director, Wind Energy Unit - ECN)

The work presented in this report has been funded by the Energy Research Centre of the Netherlands (ECN) as part of the Design for Reliable Power Performance (D4REL) project granted by the Dutch Top Consortium for Knowledge and Innovation in Offshore Wind (TKI Wind op Zee) under number TKIW02007.

Contents

List of Abbreviations

AC	Alternative Current
ACC	Tower Top Acceleration
ACT	Advanced Control Tool ®
AoA	Angle-of-Attack
a.u.	arbitrary units
DC	Direct Current
deg	angle degree
DEL	Damage Equivalent Load
DFIG	Double-Fed Induction Generator
DriD	Active Drivetrain Damping Control
HAWT	Horizontal-Axis Wind Turbine
kW	kiloWatt
LFT	Linear Fractional Transformation
LMI	Linear Matrix Inequality
LPV	Linear Parameter-Varying
LQG	Linear Quadratic Gaussian
LQR	Linear Quadratic Regulator
LTI	Linear Time-Invariant
LTV	Linear Time-Varying
MAX	Maximum
MW	MegaWatt
MWh	MegaWatt Hour
NF	Tower Natural Frequency
NOM	Nominal
PA	(Blade) Pitch Angle
PDF	Probability Density Function
PDLF	Parameter-Dependent Lyapunov Function
PI	Proportional-Integral
PD	Proportional-Derivative
PoW	Produced Electrical Power
POS	Tower Top Position
PR/RSC	Rower Regulation/Rotor Speed Control
RFC	Rainflow-Counting
PSD	Power Spectral Density
RS	Rotor Speed/Rotational Sampling (case-dependent)
ROT	Rotor
rpm	revolutions per minute
SCIG	Squirrel-Cage Induction Generator
SDP	Semi-Definite Programming
STD	Standard Deviation
SVD	Singular Value Decomposition
TowD	Active Tower Damping Control
TQ	Generator Torque
TWr/TOWr	Turbine Support Structure (Tower)
VS-VP	Variable-Speed Variable-Pitch
WS	Wind Speed
ZOH	Zero-Order Hold Discretization

“One just principle from the depths of a cave is more powerful than an army.”

José Martí

Acknowledgements

The work presented in this report has been performed at the Energy Research Centre of the Netherlands under the close supervision of Stoyan Kanev, who I would like to thank for his guidance, patience and friendship - I have truly enjoyed every single day of our collaboration. I am equally grateful to Jan-Willem van Wingerden for having coordinated this work and also for teaching me two of my favourite subjects taken as part of the Master's study curriculum at the Delft Center for Systems and Control; most of all, I would like to thank Jan-Willem for his continued support during my entire period as an MSc student. Thank you Xavier Bombois and Ton van den Boom for our interesting technical discussions and for answering the many questions that I have had regarding the research aspects of the topics covered in your courses at the Delft University of Technology. I would like to express my gratitude to all the members of my defense committee and especially to Simone Baldi and Yasin Gunes for participating in the final assessment of this project. Kitty, thank you very much for all the help provided during my time at the Delft Center for Systems and Control and for organizing my final defense.

From the Energy Research Centre of the Netherlands, Özlem Ceyhan, Feike Savenije, Wouter Engels, Maryam Soleimanzadeh and Dennis Wouters are acknowledged for their ideas and contributions to the project. Special thanks to Roland Tóth from the Eindhoven University of Technology for his advice and feedback regarding discrete-time LPV synthesis. Boris Fischer from the Fraunhofer Institute for Wind Energy and Wind Technology Systems is acknowledged for a very interesting discussion regarding the mitigation of support structure fatigue loads. Additionally, I would like to thank Sachin Navalkar and Edwin van Solingen from Delft University of Technology for their helpful suggestions regarding various aspects of the presented work.

Thank you Martijn and Anne, Paolo, Harsh, Ioannis and Anna, Marc, Ruxandra, Andrei, Raluca and Nicu you have all made the period of my Master's studies truly wonderful and my stay in Delft magical. Thank you Fulvio and Micaela for the amazing and inspirational weekend in Cambridge which set the tone for a change of vision. Thank you Koen, Stefanos and Athanasios for all the wonderful times that we have had in North-Holland. Special thanks go to my long-lasting friends Aura and Marian, Alexandru, Ionuţ and Andrei: your encouragements and kind words have always made the hardest of times less severe and the best of times even better. Few existing words could ever express the gratitude that I have towards my parents Mirela and Cristian, and grandparents Felicia, Florea, Cornelia, Georgeta and George for their continued love and support - this thesis and its contributions are dedicated to them. At last, this time around is owed to G. for bringing many rhymes and all the good reasons.

V. Pascu
24 June 2015
Delft, The Netherlands

1

Introduction and Project Approach

1.1 Background and Formulation of Research Objectives

While it is true that our planet has many energy resources on offer - amongst them coal, oil and gas currently exploited to inadmissible extents - the activity of the human race has to abide by the same unwritten rules as those for any other species: if these resources are to be used, this needs to be done in a fully sustainable way. Failing to do so can take its toll not only on the growth process intrinsic to the human society - it can also endanger our entire race. The idea of *harvesting* these energy resources rather than *exploiting* them has therefore naturally come into play towards the end of the 20th century. Although the treatment of energy like agricultural crops is more of an intention rather than a practical plan [3], one realistic method of implementing this new philosophy is to make use of renewable or almost-inexhaustible sources such as wind, solar and hydro energy. These are not equally spread across all geographical areas and moreover, even if present, the amount of available power in each of these depends on many factors such as the season of the year and the time of the day. Of these, wind has been claimed to be the most reliable [70], due to its high degree of consistency on large time scales. Although wind energy can be extracted in many different ways, conventional horizontal-axis wind turbines are predominantly used and largely accepted due to their versatility [10].

The earliest use of wind as a source of energy has been in the sail boats of the Ancient times - our predecessors learned by observation that the wind's force can be harnessed for transportation by using properly-dimensioned sails. The same principle has later been applied in the first wind mills, supplying both force for grain-grinding and also automating the process to some extent. Horizontal-axis wind mills appeared in the Middle Ages and were soon preferred over their vertical-axis counterparts which had been exclusively used up to that time, due to their higher structural efficiency. Their improvement process has been almost continuous and up to the late 18th century they have evolved from traditional post mills to highly-advanced tower mills where full treatment of the grains could be achieved, story by story. Plenty of engineered knowledge had already been derived regarding the design of the mechanical components and the blades; this made the entire design relatively efficient, yet these were not able to compete with the performance provided by the steam engine and hence their use began to decline. A breakthrough occurred in 1888, when Charles F. Brush coupled an electric machine to a multi-bladed rotor to generate electricity: the first *wind turbine* (Figure 1) had been created.

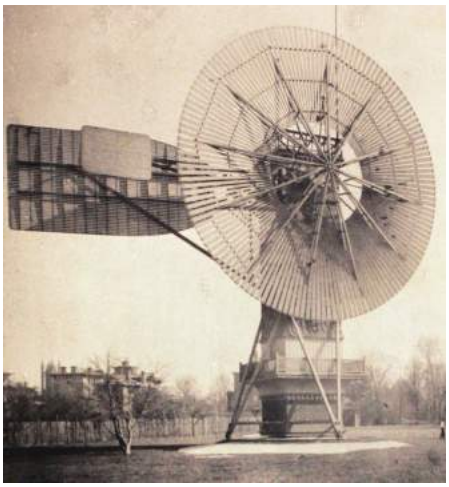

Figure 1: The Brush Wind Turbine in Cleveland, Ohio (photo: cca. 1888)

The Brush wind turbine was in operation for 20 years, but its power capture performance was severely limited by its high-solidity rotor. It was three years later that another inventor by the name of Poul la Cour created the first full wind turbine design by integrating system-level knowledge of blade aerodynamics, mechanical transmissions and electric machinery. However, the wider spread of such turbines was still limited before the 1940s due to non-constant availability, either because of their relative incapability of making the most out of the available wind resource or due to their many failures. In the post-World War I period it had become obvious that rural areas supplying the gross food resources in the United States needed to comply with electrical grid regulations so that they could directly receive the necessary electrical energy for producing and processing their crops to deliver their goods faster and in larger amounts. It has, therefore, been imposed on farmers of the time to no longer rely on the sole use of their turbines for electrical supply - this, in turn, lead to another period of absence of technological development in wind energy.

Figure 2: The Smith-Putnam Wind Turbine in Castleton, Vermont (photo: cca. 1942)

This was all about to change in 1931 when the first 100 kW wind generator was created in Russia and showed potential of utility-scale wind energy production. The United States also followed and delivered in 1941 a 1.25 MW machine; designed by Palmer C. Putnam and produced by S. Morgan Smith Company, the Smith-Putnam wind turbine, shown in Figure 2, featured a two-bladed downwind rotor and allowed for collective blade pitch control to maintain steady rotor speed in above-rated wind conditions. The huge success, however, was overshadowed by a critical failure that occurred only after several hundreds of hours of operation: this was caused by the immense mechanical loads on the blades, completely disregarded during the design phase, which lead to early fatigue in the blade materials. The challenges of designing a large-scale machine that could withstand such high mechanical loads had been too big to allow for higher penetration of wind-based generated electricity until the late 1960s. Many new technologies had, nonetheless, been proposed for the realization of more reliable components - one such example lies in the works of Ulrich Hutter, who brought forward the idea of equally-spreading the aerodynamic loads on the rotor over the surface of the blades, rather than withstanding them: this could be done by using elastic materials such as fibre glass and plastic. Similarly, the small wind energy community began around this time to understand the need for some form of automatic control in order to achieve all the different requirements for the reliable operation of wind turbines.

It may be fairly stated that government-funded development in wind turbine technology dawned with the 1973 oil crisis - the United States would lead the way in providing financial support for both fundamental and applied research pertaining to multi-megawatt wind energy systems. As a matter of fact, so pioneering was this approach of the American government that they even considered funding improvements for vertical-axis machines, which were very unpopular at that time - and all this despite their well-known limitations. Moreover, even their National Aeronautics and Space Administration (NASA) decided to take part in the developments aimed at. The few implemented horizontal-axis experimental designs performed exclusively by NASA, namely the 200 kW MOD-0A, the 2 MW MOD-1, the 2.5 MW MOD-2, the 3.2 MW MOD-5B and the 4 MW WTS4 helped the United States energy programme progress rapidly. All these designs brought forward more challenges than solutions, yet by 1981 this federal programme had already been deemed a success due to the amount of expertise developed and made available to potential industries.

The European Union took unexpectedly long to react firmly to the United States Wind Energy Programme - in the wind energy community this is a fact often shown as an example of how big a role energy policy plays in the advancement for higher penetration of renewables and how this is relevant also from a geopolitical point of view. Nonetheless, both the European and the American energy markets were ready by mid-1980s for wind energy conversion systems. Predominantly built at first in United States and then in Europe, the turbines erected in the late 20th century were multi-hundred kilowatt machines placed in *wind farms* in unpopulated areas with increased wind potential. Just as

the technical challenges of designing reliable large-scale wind turbines had been acknowledged less than one hundred years earlier, the difficulties in operating high-performance wind farms also became visible after their construction. Overall, the wind energy sector is still far from having reached its full potential to this day.

Figure 3: An Offshore Wind Turbine in the North Sea (photo: 2014)

Current trends in the advancement of wind energy systems aim at bringing forward only technological developments that allow for the reduction of the cost of produced energy. Wind turbines are very expensive machinery and the return of investment in wind farms is intimately related not only to high energy production over the system lifetime: maintaining mechanical loads within acceptable bounds during operation, preventing unnecessary turbine downtime in case of extreme events, as well as regulating the quality of generated power are topics that also receive special attention from an early design phase. The cost of wind energy might, moreover, be further lowered if wind farms could actively support the AC power grids [63, 1]. A major trend in recent years for the large-scale production of wind energy is to construct wind turbines in offshore locations, where the wind has increased availability throughout the year and higher power. Moreover, offshore wind is less turbulent which naturally leads to reduced dynamic mechanical loads on turbine components such as blades, support structure and drivetrain. Nonetheless, the maintenance, installation, foundation and infrastructure costs associated with offshore wind energy production are higher. Given that a large amount of factors come into play when the cost of offshore wind energy is evaluated, it is necessary to develop methods for cost of energy reduction by lowering all system production and operation costs triggered by design uncertainty and improving upon system reliability - this is the direction in which the Design for Reliable Power Performance (D4REL) research project follows closely [66]. From the point of view of automatic control, wind turbines are challenging systems to operate such that the return of investment for even a single system is maximal - on the other hand, without feedback control it is likely that wind turbine operation is not even safe in most cases [74].

Despite the fact that modern wind turbines can be controlled better - because they are constructed as variable-speed variable-pitch (VS-VP) machines, on one hand, and due to the advances in associated actuators and sensors technologies, on the other - many solutions fail to be as good in practice as they are attractive in theory. It is the goal of D4REL to ensure that all proposed solutions are scientifically and technologically sound. The D4REL project aims to decrease the cost of produced energy in offshore wind turbines/farms by reducing the design uncertainties thus allowing for a re-assessment of the implied design safety factors. As an essential part of *Work Package 4: System Identification for Robust Control*, the goal associated with this thesis is to propose a robust or self-adapting wind turbine control design methodology that can enable the achievement of the aims of D4REL:

> The **goal of this thesis** is to develop a **wind turbine control design algorithm** for **reducing the cost of energy** by **fully exploiting the uncertain nature of offshore wind turbine behaviour** in terms of its **aerodynamics** due to **manufacturing, ice accretion, blade erosion and dirt build-up** and **support structure dynamics** due to **installation, marine sand dunes, scour and biofouling**.

This is achieved by first analyzing and quantifying the effects of uncertainties on the performance of wind turbine control systems with a reference control design tool [52] and, subsequently, by addressing the relevant issues by means of matured modern advanced control design methods known to be practically-applicable to uncertain systems, without severe limitations or shortcomings: to this extent, linear matrix inequalities (LMIs) approaches to robust and linear parameter-varying (LPV) control synthesis are considered. Comparison with current implementations of the relevant control loops [52] is provided together with a quantification of the added benefit of any proposed solutions at system

level for a generic three-bladed VS-VP upwind horizontal-axis wind turbine (HAWT) [48, 58]. The solutions proposed in this thesis need to also be sufficiently realistic and attractive for the wind turbine manufacturing industry, allowing for a proper balance between design optimality, design conservatism and implementability as well as for relative ease in system certification. An outline of these goals is given schematically in Figure 4.

1.2 Thesis Outline

The work performed in approaching the formulated goal is described in the current report in a step-by-step manner. Consequently, the thesis is comprised of two parts. In the first one, attention is given to the analysis of design uncertainty and the corresponding effects on control systems performance. In **Chapter 2**, an overview is given regarding the control-relevant aspects of wind turbines: the wind resource is described in connection with wind turbine operation, a framework for wind turbine modeling is offered and the project-relevant state-of-the-art in wind turbine control systems, as part of the reference advanced control design tool (ACT), is discussed from both a design and simulation point of view. In **Chapter 3**, the proposed sources of uncertainty in wind turbine operation are investigated starting from the reported results in the recent technical literature; the effects of these uncertainty factors are translated for the case of the employed wind turbine model and quantified towards the worst-case performance outcomes. The chapter gives an accurate perspective on the amount to which design uncertainty plays a role on control system performance and further defines a clear direction towards addressing the project-relevant issues.

The focus in the second part of the thesis is on creating a practical framework for the synthesis of advanced wind turbine controllers that can potentially cope with the described design uncertainty. In **Chapter 4**, a linear parameter-varying control design methodology is applied for the improved design of one of the wind turbine control loops. In **Chapter 5** conclusions are drawn from the directions explored in the report and the associated observed results and, eventually, recommendations for further improvements are made in relation to the formulated research objectives. Additionally, in **Appendix A** robust and LPV control theory is presented from an LMI viewpoint - use is made exclusively of linear matrix inequality techniques for optimization-based synthesis; as a project-relevant example, the derivation of the LPV dynamic output-feedback solution to the $\mathcal{H}_2$ control synthesis problem for discrete-time systems for use in **Chapter 4** is shown. Finally, **Appendix B** provides essential information regarding the reference HAWT used for the simulations presented throughout the report.

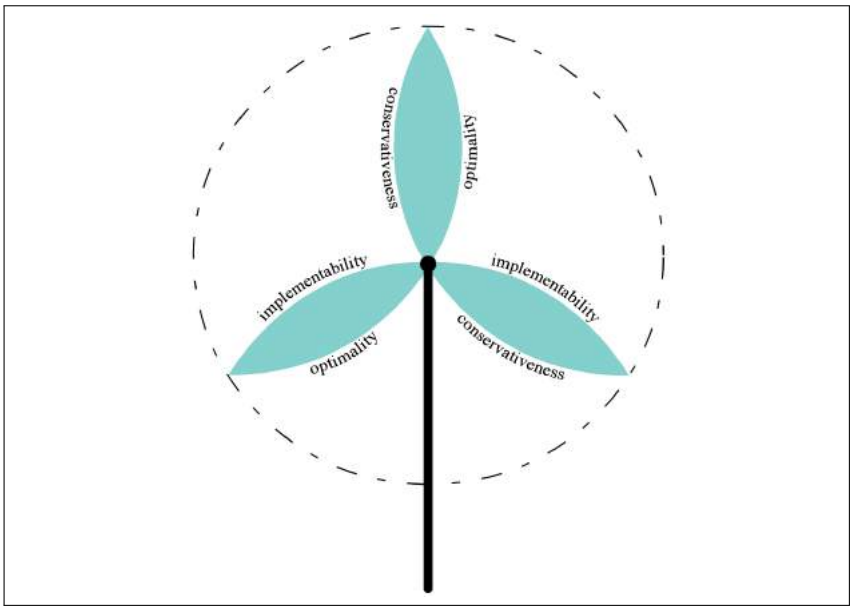

Figure 4: Schematic Summary of Desired Characteristics for the Proposed Controls Solutions as part of the D4REL Research Project

2

Wind Turbine Dynamics and Model-Based Control

This chapter presents one possible state-of-the-art approach to model-based wind turbine control design in relation to the mentioned goals of this thesis. The wind is first described as an essential aspect for turbine operation and several remarks are made regarding its effects on power production, power quality and system lifetime. Secondly, the dynamic behaviour of three-bladed VS-VP upwind HAWTs is reviewed from an analytical point of view - for model-based control, as well as for simulation, mathematical models represent the *real* system up to some extent and important remarks are made regarding the choices taken in this characterization. Finally, the control loops that are relevant for the formulated goals of the thesis are described together with their associated design methodologies, as part of the proposed reference control design tool ACT [52].

2.1 General Characteristics of the Wind

The wind constitutes both a *raison d'être* for wind turbines and also the main source of disturbance to their operation; whereas the former aspect is positive and directly associated with power production, the latter is negative and closely related to both inferior power quality and limited wind turbine lifetime. The wind, in a large scale meteorological sense, is the movement of large masses of air inside the Earth's atmosphere; these movements are caused by differences between regional atmospheric pressures which are, in turn, triggered by uneven heating from the Sun [63].

On a smaller scale, the coordinated movement of these masses of air is characterized within *wind fields* [21]; these describe the spatial properties of the wind - they are fictitious hexahedrons in the three-dimensional space where every point is characterized by a specific wind speed v; to properly describe the wind also from a temporal perspective, the wind fields would change with time, which naturally implies that the wind speed at any given point in space x will be time-dependent, thus denoted by $v(x,t)$. The variability of the wind speed can be appropriately described by certain power spectra; the most-widely used class for such purposes is the empirical van der Hoven spectrum [90] which emphasizes the existence of two separate peaks that catch the essence of wind's fluctuation: a high peak corresponding to some low-frequency region (i.e. slowly-varying wind speeds) and a lower peak corresponding to some high-frequency region (i.e. quickly-varying wind speeds); these two peaks are separated by a spectral gap and, because of this fact, any *local* wind speed for a given wind field of arbitrary size is suitable to be looked at as a summation of two main components [17]:

$$v(x,t) = v_{mean}(x,t) + v_{turb}(x,t) \tag{2.1}$$

namely the *mean wind speed* denoted by $v_{mean}(x,t)$ and the *(atmospheric) turbulence* $v_{turb}(x,t)$; generally speaking, the former component contributes to the energy production in wind turbines, whereas the latter is the main source of both fatigue loads in the mechanical components and possible violation of electrical grid power requirements. As mentioned, the $v_{mean}(x,t)$ component is slowly-varying and its relation to $v(x,t)$ is also given by:

$$v_{mean}(x,t) = \frac{1}{T_p}\int_{t-T_p/2}^{t+T_p/2} v(x,\tau)d\tau \tag{2.2}$$

for some large time interval T_p. The mean wind speed is, as a matter of fact, not only a method of describing the average temporal characteristic of the wind for the defined wind field but also the spatial one; this is because the movement of the mentioned air masses is indeed *coordinated*. For a given wind field and a particular time interval, v_{mean} is statistically described by a Weibull distribution [94]:

$$P(v_{mean}) = \frac{k}{c}\left(\frac{v_{mean}}{c}\right)^{k-1} e^{-(v_{mean}/c)^k} \tag{2.3}$$

parametrized by constants k and c, called shape factor and scale factor, respectively. An example of such a distribution is depicted graphically in Figure 5; as can be seen, certain mean wind speeds v_{mean} within a wind field at a particular time instant are typically more probable to occur than others; in general, the occurrence of high and low mean wind speeds is less likely. The statistical Weibull distribution for a specific geographical site is one important factor in choosing a wind turbine model that will enable a high return of the cost of investment.

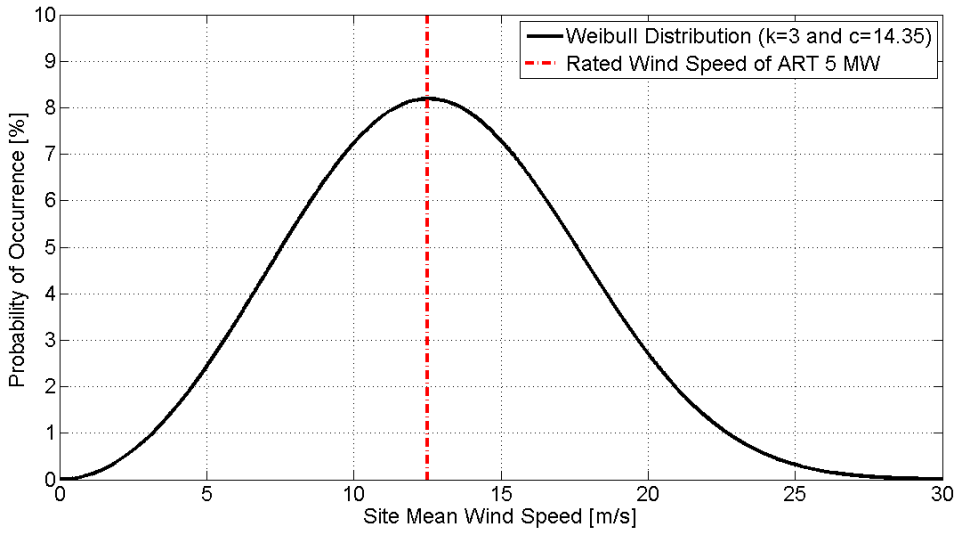

Figure 5: Fictitious Weibull Mean Wind Speed Distribution of a Potential Site for the ART 5 MW

The turbulent component of the wind speed $v_{turb}(t)$ is also comprised of two parts [17]:

$$v_{turb}(t) = v_{sto}(t) + v_{det}(t) \tag{2.4}$$

of which one is stochastic $v_{sto}(t)$ and one deterministic $v_{det}(t)$. The stochastic part of the turbulent component could be described as a filtered version of a random signal $w(t)$ with Gaussian probability density function (PDF) and constant

power spectral density (PSD) [17]; one example of such a filter that produces a stochastic component of the turbulence $v_{sto}(t)$ with a realistic spectrum is [52]:

$$H_{turb}(s) = \frac{k_{sto}}{(1 + sT_{sto})^{5/6}} \tag{2.5}$$

parametrized in terms of k_{sto} and T_{sto}, called the magnitude factor and the time constant of the stochastic components, respectively; these typically depend also on $v_{mean}(t)$ amongst other variables; the introduced $H_{turb}(s)$ leads to the so-called Kaimal spectrum [49] of turbulence. The deterministic components, on the other hand, are *wind shear* i.e. the effect of increasing mean wind speeds as a function of altitude [21, 72] and *wind shadow* i.e. the effect of disturbed natural air flows due to the presence large obstacles such as a wind turbine support structure [63, 72], in this case also known as the *tower shadow*.

Although very realistic, the description of wind based on wind fields is not especially suitable for many practical reasons concerning wind turbine control design and/or simulation; this is due to its unreasonably high computational and descriptional complexity. Two suitable alternatives are usually preferred for such purposes. One of them is a description in terms of blade-effective wind speeds [52, 54, 89, 92] - a three-bladed wind turbine experiences the wind from the perspective of three separate wind speeds $v_i(t)$, one per blade, with their associated mean wind speeds $v_{mean_i}(t)$ and turbulent components $v_{turb_i}(t)$ with $i = \overline{1,3}$; whereas the blade-effective mean wind speeds are typically all equal to some value $v_{mean}(t)$, the turbulent components differ among the blades [52]. The other alternative is to use a rotor-effective wind description where the wind speed $v_{rot}(t)$ shows the way in which the turbine rotor would perceive a wind field at its hub rotational-axis level; in the remaining part of this thesis it will be assumed that the rotor-effective wind speed is the average of the blade-effective wind speeds.

Furthermore, the turbine rotor and the turbine blades will experience their corresponding *apparent* wind speeds that account for tower top movement, for additional blade deformation and for the rotational sampling (RS) effect caused by the rotation of the turbine blades through the wind field [21]; this latter factor gives rise to additional peaks in the power spectrum of a rotor-effective wind realization (i.e. positive integer multiples of the rated rotor speed 1P e.g. 3P, 6P, etc. for a three-bladed wind turbine); in Figure 6 the power spectrum of one viable realization of the rotor-effective wind speed is shown as an example. Within the reported work, blade-effective wind speeds are used for wind turbine simulation whereas rotor-effective wind speeds are used for wind turbine control.

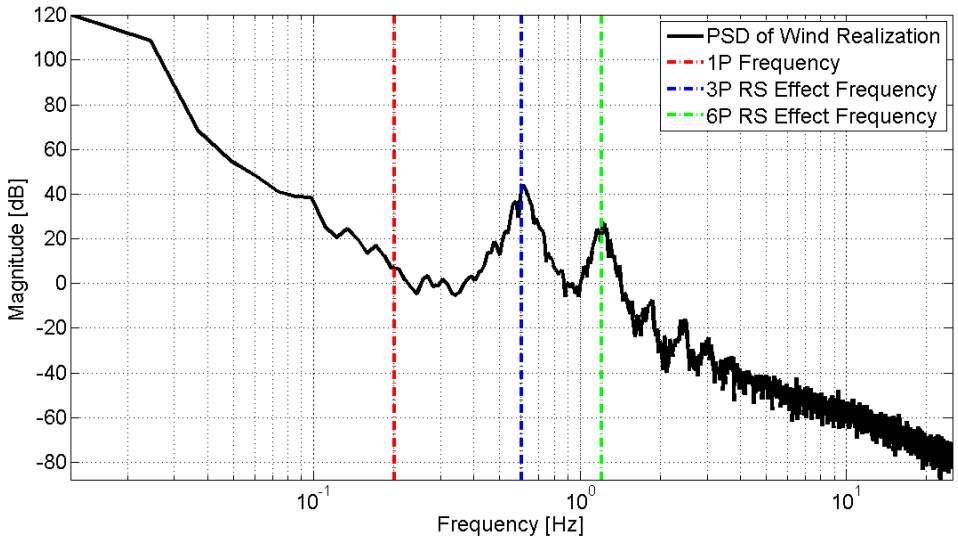

Figure 6: Power Spectrum of a Rotor-Effective Wind Realization for the ART 5 MW

2.2 Control-Oriented Wind Turbine Modeling

Wind turbines can be modeled in many different ways, depending on what purpose any particular model has to serve [21, 63]. Whereas typically for simulations higher-fidelity models are necessary to capture their behaviour, for control design it is necessary to have more simple models that represent this behaviour only up to some extent that is relevant for the control purposes [83]. The main components of a wind turbine physically interact with each other as shown in Figure 7; as can be seen, the different subsystems that correspond to these components will share variables that describe the various interactions. A natural step further is to also characterize the dynamic behaviour of each subsystem individually, as will be done next.

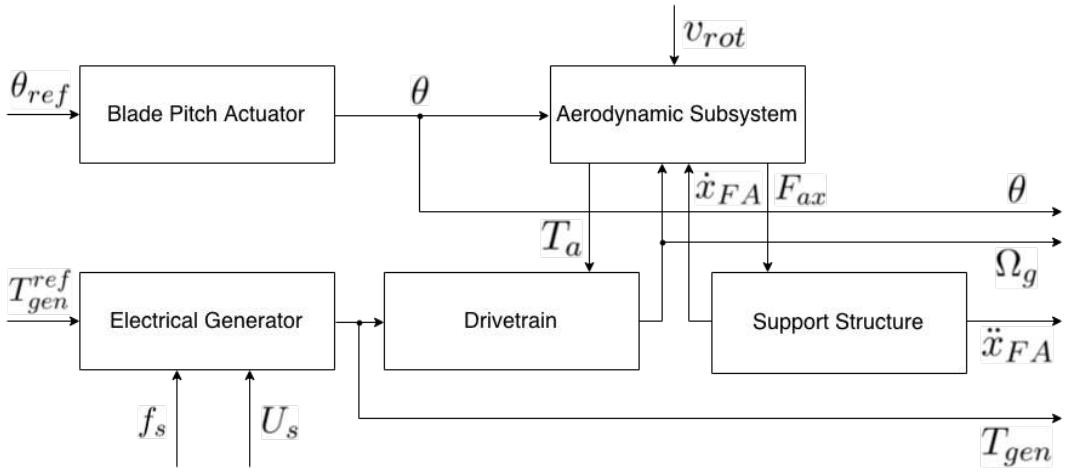

Figure 7: Main Subsystems within a Wind Turbine

The Aerodynamic Subsystem

The wind turbine captures energy from the wind by means of its rotor, which is comprised of a certain number of identical blades, to this extent three. By assuming equal aerodynamic efficiency along each turbine blade supposed to be rigid throughout this analysis, and that the wind speed is the same for an entire rotor-swept area of radius R, the rotor will experience an axial aerodynamic thrust force:

$$F_{ax}(t) = \frac{1}{2}\rho\pi R^2 v_{rot}^2(t) C_T(\lambda(t), \theta(t)) \tag{2.6}$$

as well as an aerodynamic torque:

$$T_a(t) = \frac{1}{2}\rho\pi R^3 v_{rot}^2(t) C_Q(\lambda(t), \theta(t)) \tag{2.7}$$

both proportional to the air density ρ, the rotor-effective wind speed $v_{rot}(t)$ and the thrust $C_T(\lambda(t), \theta(t))$ or torque $C_Q(\lambda(t), \theta(t))$ coefficients; these coefficients depend on the tip-speed-ratio $\lambda(t)$ and $\theta(t)$ which represents the pitch angle of the blades, sometimes called the collective blade pitch angle. The former term, defined as a time-dependent ratio between the tangential speed of the tip of the blades and the rotor-effective wind speed:

$$\lambda(t) = \frac{\Omega_r(t) R}{v_{rot}(t)} \tag{2.8}$$

represents the achieved aerodynamic efficiency i.e. what portion of the energy in the wind is indeed captured by the turbine rotor. Although different from rotor to rotor, depending on blade and rotor geometries as well as their

corresponding surface roughness, the $C_T(\lambda(t), \theta(t))$ and $C_Q(\lambda(t), \theta(t))$ coefficients will both generally have similar appearances between different rotors, as shown for example in Figure 8 and Figure 9; note that these have been plotted only for positive values of the corresponding coefficients. Similarly, the rotor-effective aerodynamic power $P_{rot}(t)$ is given by:

$$P_{rot}(t) = \frac{1}{2}\rho\pi R^2 v_{rot}^3(t) C_P(\lambda(t), \theta(t)) \tag{2.9}$$

The power coefficient $C_P(\lambda(t), \theta(t))$ is generally used to describe the achieved energy capture efficiency of the entire rotor; this coefficient, also similar between different turbine rotors is shown as an example in Figure 10; it is also a function of $\lambda(t)$ and $\theta(t)$ and has a maximum value whose location with respect to these two variables is very important for wind turbine control, as will be discussed later on; the relation between $C_P(\lambda(t), \theta(t))$ and $C_Q(\lambda(t), \theta(t))$ is defined [21] as $C_P(\lambda(t), \theta(t)) = C_Q(\lambda(t), \theta(t))\lambda(t)$. Further modeling of the aerodynamic subsystem for simulation purposes needs to account for aeroelasticity as the assumption that the blades are rigid is not realistic, blade-effective forces and torques due to blade-effective wind speeds, as well as various other aerodynamic phenomena [52].

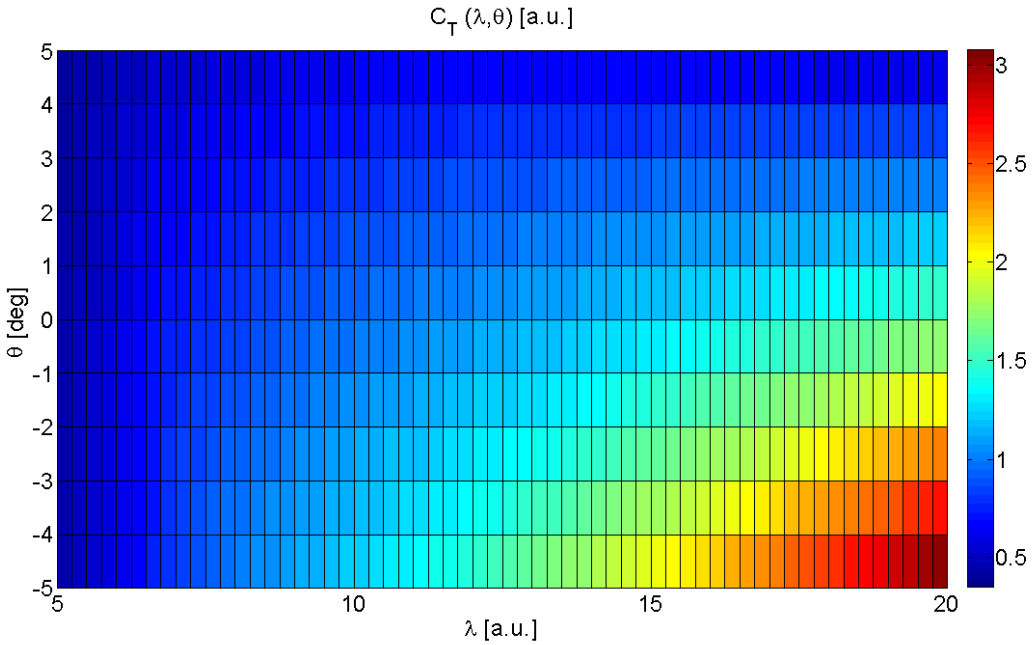

Figure 8: Rotor Thrust Coefficient Curve for the ART 5 MW

The Blade Pitch Actuator

The blade pitch angles can be adjusted by wind turbine controllers through the pitch actuation mechanisms; their pitch angle, assumed to be the same for all blades will be denoted by $\theta(t)$. The pitch actuation mechanisms are linear servomechanisms that can be modelled by second-order time-delayed linear models:

$$\ddot{\theta}(t) + 2\zeta_{pt}\omega_{pt}\dot{\theta}(t) + \omega_{pt}^2\theta(t) = \omega_{pt}^2\theta_{ref}(t - \tau_{pt}) \tag{2.10}$$

with natural frequency ω_{pt}, damping ratio ζ_{pt} and pure delay τ_{pt}. These actuator mechanisms will dynamically deliver the required pitch angles only up to a certain extent, which can be modeled through the constraints:

$$\begin{aligned}\theta_{min}(t) \leq \theta(t) \leq \theta_{max}(t)\\ \dot{\theta}_{min}(t) \leq \dot{\theta}(t) \leq \dot{\theta}_{max}(t)\\ \ddot{\theta}_{min}(t) \leq \ddot{\theta}(t) \leq \ddot{\theta}_{max}(t)\end{aligned} \tag{2.11}$$

on the pitch angles and their first- and second-order derivatives. The unconstrained model of the actuator (2.10) can be used in the model for control design, although it is in general disregarded due to its faster dynamics when compared to those of other subsystems; for system simulation the constrained model (2.10) and (2.11) is, nonetheless, used [52].

The Drivetrain

The drivetrain, composed of two shafts connected through a gearbox with transmission ratio i_{tr}, is fixed to the turbine nacelle. The fast shaft is generally assumed to be rigid, whereas the slow shaft is realistically considered flexible and modeled by the first associated lead-lag mode with torsional stiffness s_{dt} and damping d_{dt}. The transmission ratio is defined to be positive when the rotation of both shafts is in the same direction and opposite otherwise. Overall the drivetrain dynamics are modelled as [52]:

$$\frac{i_{tr}^2 J_r J_g}{(1-T_T)J_r + i_{tr}^2 J_g}\ddot{\gamma}(t) + d_{dt}\dot{\gamma}(t) + s_{dt}\gamma(t) = \frac{i_{tr}^2 J_g}{(1-T_T)J_r + i_{tr}^2 J_g}T_a(t) + \frac{J_r}{(1-T_T)J_r + i_{tr}^2 J_g}\,|i_{tr}|\,T_{gen}(t) + \frac{J_r}{(1-T_T)J_r + i_{tr}^2 J_g}\left(T_C + T_V\frac{1}{i_{tr}\Omega_g}\right) \tag{2.12}$$

where $\gamma(t)$ is the angular difference between the two ends of the drivetrain whose evolution can be represented as $\dot{\gamma}(t) = \Omega_r(t) - \frac{1}{i_{tr}}\Omega_g(t)$ with rotor speed $\Omega_r(t)$ and electrical generator speed $\Omega_g(t)$; J_r and J_g are the rotor and generator inertia, respectively, while $T_{gen}(t)$ is the electrical generator torque; the rotational speed of the turbine rotor and of the electrical generator are related through $\gamma(t)$ and $T_a(t)$ by:

$$J_r\dot{\Omega}_r(t) = T_a(t) - s_{dt}\gamma(t) - d_{dt}\frac{\Omega_g(t) - i_{tr}\Omega_r(t)}{i_{tr}} \tag{2.13}$$

The following additional torques have been defined in (2.12) to model various drivetrain losses due to friction: Coulomb friction torque T_C, viscous friction torque T_V and generalized friction torque T_T.

The Electrical Generator as a Torque Actuator

Regardless of whether the generator itself is of stator-controlled squirrel-cage induction generator (SCIG) type or of rotor-controlled double-fed induction generator (DFIG) type, the electrical generator torque can also be adjusted by wind turbine controllers through power electronics; for this reason the electrical generators can be seen from a controls viewpoint as torque actuation mechanisms and, as in the case of the pitch actuators, these are linear servomechanisms modelled as second-order linear models:

$$\ddot{T}_{gen}(t) + 2\zeta_g\omega_g\dot{T}_{gen}(t) + \omega_g^2 T_{gen}(t) = \omega_g^2 T_{gen}^{ref}(t) \tag{2.14}$$

with natural frequency ω_g and damping ratio ζ_g. Due to their wide range of delivered torques and fast dynamics, the torque actuators are in general not considered to be constrained. The generator terminal voltage $U_s(t)$ and grid frequency $f_s(t)$ from Figure 7 are assumed to be fixed and stable variables [17], and hence have no dynamic effects on $T_{gen}(t)$. Similarly, the electrical generator is a subsystem that can supply a torque based on a given demand $T_{gen}^{ref}(t)$

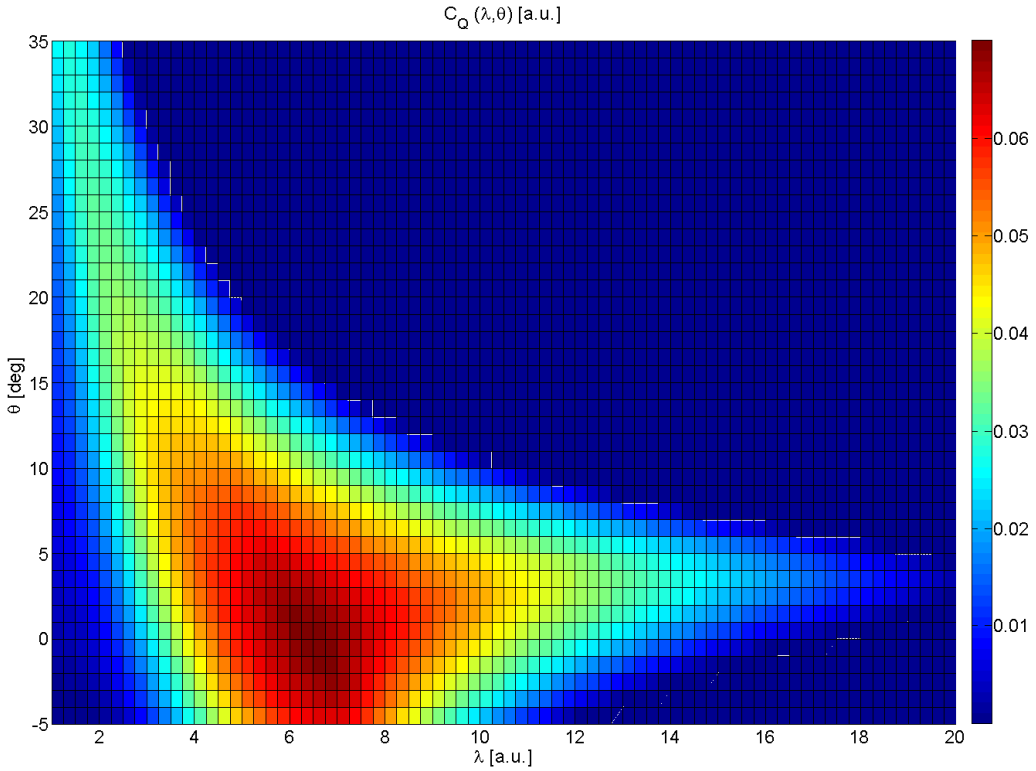

Figure 9: Rotor Torque Coefficient Curve for the ART 5 MW

therefore no torque-related dynamic effect due to the generator speed $\Omega_g(t)$ resulting from the rotational motion of the fast shaft is taken into account [52]. For control design the torque actuator model is not considered due to its mentioned fast dynamics, yet in simulation it is used as defined by (2.14).

The Wind Turbine Support Structure

Although seemingly rigid, the turbine support structure will deform during operation; the associated motion is mostly visible at the tower top which can be seen to change position in both the longitudinal plane defined by the axial rotor-effective wind speed $v_{rot}(t)$ (the so-called *fore-aft direction*) and the lateral one (the *side-to-side direction*), perpendicular to $v_{rot}(t)$. For control purposes it is common to model only the first structural modes in these two directions, as these are the main contributors to the tower top motion. Within this thesis, however, only the fore-aft motion of the tower top is considered.

The equation that defines the tower top motion dynamics is then:

$$m_t\ddot{x}_{FA}(t) + d_t\dot{x}_{FA}(t) + s_t x_{FA}(t) = F_{ax}(t) \tag{2.15}$$

given in terms of tower top equivalent mass m_t, stiffness s_t and damping d_t and the rotor-effective axial aerodynamic thrust force $F_{ax}(t)$. For simulation, more realistic and nonlinear dynamics for the tower motion are considered i.e. multibody dynamics models [52].

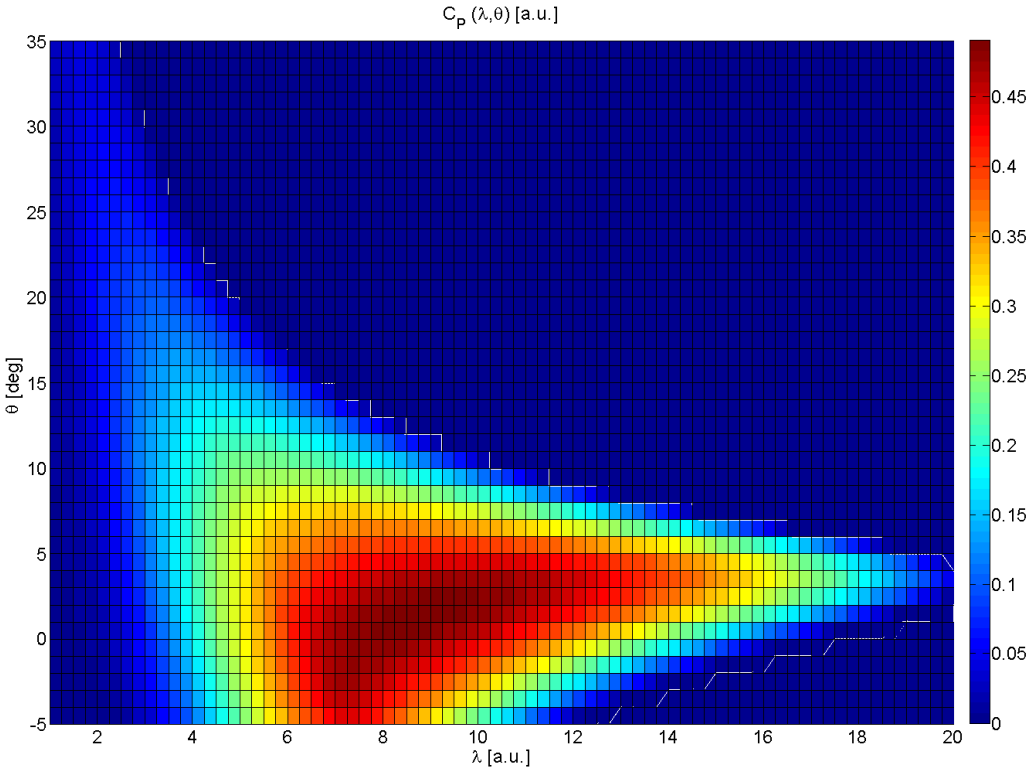

Figure 10: Rotor Power Coefficient Curve for the ART 5 MW

2.3 Wind Turbine Control Systems

In the previous section several models of the wind turbine subsystems have been described; as has been mentioned, their modeling has followed control-relevant criteria suitable for the goals of this thesis. Now, based on these models the control loops that pertain to the same objectives will be described; their layout, as well as their associated design methodologies covered in the remaining part of this chapter are implemented in the considered reference control design tool [52]. As will be explained, all these control loops have two main components: one that provides estimates of the unknown but required variables for control (called either *estimator* or *observer* depending on the reconstruction algorithm type) and one that uses these estimates as well as other information for computing a feedback control signal for each control loop.

From Measurements to Estimates

In a wind turbine, although many measurements are usually taken for different purposes, not all of them can be used for control [21, 63]. For the control loops investigated in this thesis, measurements of the generator speed $\Omega_g(t)$, the collective blade pitch angle $\theta(t)$ and the tower-top fore-aft acceleration $\ddot{x}_{fa}(t)$ are used; nonetheless, these measurements themselves do not represent all the necessary information that is needed for the feedback control loops that will be presented. Based on certain algorithms that are depicted schematically in Figure 11, additional required states can be estimated. Note that all these algorithms run in discrete-time; however, for the current exposition, they will be assumed to deliver continuous-time estimates based on received continuous-time inputs [52].

Due to the fact that neither the rotor-effective wind speed measurement nor the rotor speed measurement are generally available [21], within ACT [52] one first needs to estimate the aerodynamic torque $T_a(t)$ and the rotor speed $\Omega_r(t)$ by using the available measurements $T_{gen}(t)$ and $\Omega_g(t)$. For feedback control, it will also be necessary to have access to an estimate of the shaft torsion angle $\gamma(t)$, as will become visible later in this chapter. One possible method of

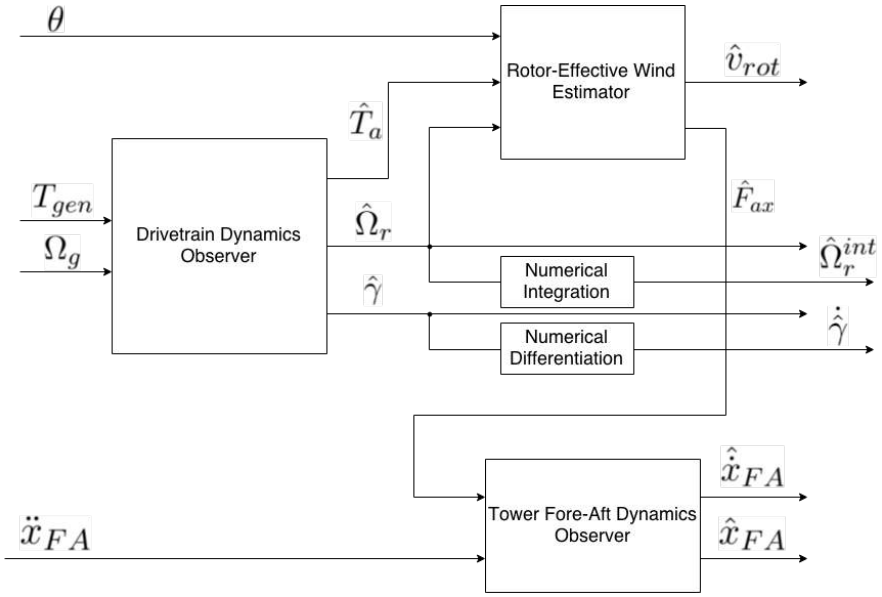

Figure 11: Overview of the Required Wind Turbine Information Reconstruction Algorithms

estimating these variables dynamically is to use the modeled information about the drivetrain dynamics and get a one-shot estimate of all three [52]. To this extent, based on the drivetrain dynamics in (2.12) and (2.13), now formulated as a standard state-space model:

$$\begin{aligned}
\begin{bmatrix} \dot{\gamma}(t) \\ \dot{\Omega}_r(t) \\ \dot{\Omega}_g(t) \end{bmatrix} &= \underbrace{\begin{bmatrix} 0 & 1 & -\frac{1}{i_{tr}} \\ -\frac{s_{dt}}{J_r} & -\frac{d_{dt}}{J_r} & \frac{d_{dt}}{i_{tr}J_r} \\ \frac{(1-T_T)s_{dt}}{i_{tr}J_g} & \frac{(1-T_T)d_{dt}}{i_{tr}J_g} & -\frac{(1-T_T)d_{dt}+T_V}{i_{tr}^2 J_g} \end{bmatrix}}_{A_{dt}^{cont}} \begin{bmatrix} \gamma(t) \\ \Omega_r(t) \\ \Omega_g(t) \end{bmatrix} + \underbrace{\begin{bmatrix} 0 \\ \frac{1}{J_r} \\ 0 \end{bmatrix}}_{B_{dt,Ta}^{cont}} T_a(t) - \underbrace{\begin{bmatrix} 0 \\ 0 \\ \frac{\text{sign}(i_{tr})}{J_g} \end{bmatrix}}_{B_{dt,Tgen}^{cont}} (T_{gen}(t) + \tfrac{1}{|i_{tr}|} T_C) \\
\Omega_g(t) &= \underbrace{\begin{bmatrix} 0 & 0 & 1 \end{bmatrix}}_{C_{dt}^{cont}} \begin{bmatrix} \gamma(t) \\ \Omega_r(t) \\ \Omega_g(t) \end{bmatrix}
\end{aligned} \tag{2.16}$$

one can reconstruct $\Omega_r(t)$ and $\gamma(t)$ by making use of some linear observer [4]; for this, however, the aerodynamic torque $T_a(t)$ would need to be available which is, unfortunately, not the case; nonetheless, it could be arrived at from a random walk model, typically applied in discrete-time:

$$T_a(k+1) = T_a(k) + T_s \nu_{dt}(k) \tag{2.17}$$

which has been deemed relevant for such purposes [64, 68, 78, 53] if a suitable covariance $Q_{dt} > 0$ for the Gaussian zero-mean white noise random signal $\nu_{dt}(k)$ is defined empirically. By formulating a discrete-time state-space model $(A_{dt}^{dis}, B_{dt,T_a}^{dis}, B_{dt,T_{gen}}^{dis}, C_{dt}^{dis})$ of (2.16) through e.g. zero-order hold (ZOH) discretization [11] with sampling time T_s, extending it with (2.17) and scaling the discretized inputs as $T_{gen}^{sc}(k) = T_{gen}(k)/J_g$ and $T_a^{sc}(k) = T_a(k)/J_r$ for

improved numerical conditioning [52], an augmented-state model is arrived at:

$$\begin{aligned}\begin{bmatrix} x_{dt}^{dis}(k+1) \\ T_a^{sc}(k+1) \end{bmatrix} &= \begin{bmatrix} A_{dt}^{dis} & B_{dt,T_a}^{dis} J_r \\ 0 & 1 \end{bmatrix} \begin{bmatrix} x_{dt}^{dis}(k) \\ T_a^{sc}(k) \end{bmatrix} + \begin{bmatrix} B_{dt,T_{gen}}^{dis} J_g \\ 0 \end{bmatrix} (T_{gen}^{sc}(k) + \tfrac{1}{|i_{tr}|} T_c) + \begin{bmatrix} 0 \\ 1 \end{bmatrix} \nu_{dt}(k) \\ \Omega_g^m(k) &= \begin{bmatrix} C_{dt}^{dis} & 0 \end{bmatrix} \begin{bmatrix} x_{dt}(k) \\ T_a^{sc}(k) \end{bmatrix} + \eta_{dt}(k) \end{aligned} \tag{2.18}$$

for which a steady-state linear Kalman filter (denoted in Figure 11 by the block *Drivetrain Dynamics Observer*) can be designed [4], providing the necessary estimates $\hat{T}_a(k)$, $\hat{\Omega}_r(k)$ and $\hat{\gamma}(k)$. Note that the discrete-time measurement $\Omega_g^m(k)$ of the physical variable $\Omega_g(t)$ is affected by the additive Gaussian zero-mean white noise signal $\eta_{dt}(k)$ with covariance $R_{dt} > 0$.

Subsequently, based on the estimates $\hat{T}_a(t)$ and $\hat{\Omega}_r(t)$ of the aerodynamic torque and rotor speed, respectively, rotor-effective wind speed $\hat{v}_{rot}(t)$ and axial thrust force $\hat{F}_{ax}(t)$ estimates can also be arrived at [52]. The rotor-effective wind speed estimate $\hat{v}_{rot}(t)$ can be used for determining the estimate of the axial aerodynamic thrust force from:

$$\hat{F}_{ax}(k) = \frac{1}{2} \rho \pi R^2 \hat{v}_{rot}^2(k) C_T(\hat{\lambda}(k), \theta(k)) \tag{2.19}$$

These functions are performed by the *Rotor-Effective Wind Estimator* block in Figure 11. For further details regarding the algorithms's implementation and numerical sensitivity, see [52]. As a final estimation task, it is also necessary to derive estimates $\hat{x}_{FA}(k)$ and $\hat{\dot{x}}_{FA}(k)$ of the fore-aft tower-top position $x_{FA}(t)$ and velocity $\dot{x}_{FA}(t)$; this can be done by making use of the discretized model:

$$\begin{aligned}\begin{bmatrix} x_{FA}(k+1) \\ x_{FA}(k+2) \end{bmatrix} &= A_{t,FA}^{dis} \begin{bmatrix} x_{FA}(k) \\ x_{FA}(k+1) \end{bmatrix} + B_{t,FA}^{dis} \hat{F}_{ax}(k) \\ \ddot{x}_{FA}^m(k) &= C_{t,FA}^{dis} \begin{bmatrix} x_{FA}(k) \\ x_{FA}(k+1) \end{bmatrix} + D_{t,FA}^{dis} \hat{F}_{ax}(k) + \eta_t(k) \end{aligned} \tag{2.20}$$

obtained from (2.15) through ZOH sampling with the same interval T_s; this model is driven by the obtained discretized estimate $\hat{F}_{ax}(k)$ of the axial rotor wind force and includes the Gaussian additive zero-mean white noise $\eta_t(k)$ of covariance $R_t > 0$ for the discretized measurement $\ddot{x}_{FA}^m(k)$ of the fore-aft tower top acceleration $\ddot{x}_{FA}(t)$; a steady-state linear Kalman filter can be derived for (2.20) which achieves the current goal; this is denoted by the *Tower Fore-Aft Dynamics Observer* in Figure 11.

Aerodynamic Subsystem Linearization

In the reference control tool [52], the aerodynamic model is linearized by approximating the axial rotor-effective thrust force $F_{ax}(t)$ and aerodynamic torque $T_a(t)$ in (2.6) and (2.7), respectively. These are nonlinear functions of the collective pitch angle $\theta(t)$, rotor speed $\Omega_r(t)$ and rotor-effective wind speed $v_{rot}(t)$, now parametrized in terms of $p(t) \triangleq \begin{bmatrix} \theta(t) & \Omega_r(t) & v_{rot}(t) \end{bmatrix}^T$, the *operating point*. The linearization is performed by approximating these functions by their first order terms in their associated Taylor series expansion around a given *equilibium operating point* $\bar{p}(t)$. This

is achieved as follows [40]:

$$\begin{array}{rcl} \delta F_{ax}(p(t)) & \cong & \nabla_\theta F_{ax}(\bar{p}(t))\delta\theta(t) + \nabla_{\Omega_r} F_{ax}(\bar{p}(t))\delta\Omega_r(t) + \nabla_{v_{rot}} F_{ax}(\bar{p}(t))\delta v_{rot}(t) \\ \delta T_a(p(t)) & \cong & \nabla_\theta T_a(\bar{p}(t))\delta\theta(t) + \nabla_{\Omega_r} T_a(\bar{p}(t))\delta\Omega_r(t) + \nabla_{v_{rot}} T_a(\bar{p}(t))\delta v_{rot}(t) \end{array} \tag{2.21}$$

where $\delta F_{ax}(p(t))$ and $\delta T_a(p(t))$ represent small deviations of $F_{ax}(p(t))$ and $T_a(p(t))$ from their values at the equilibrium operating point $\bar{p}(t)$:

$$\begin{cases} \delta F_{ax}(p(t)) \triangleq F_{ax}(p(t)) - F_{ax}(\bar{p}(t)) \\ \delta T_a(p(t)) \triangleq T_a(p(t)) - T_a(\bar{p}(t)) \end{cases} \tag{2.22}$$

and, similarly, the small deviations $\delta p(t) = \begin{bmatrix} \delta\theta(t) & \delta\Omega_r(t) & \delta v_{rot}(t) \end{bmatrix}^T$ of the operating point itself around the equilibrium are given by:

$$\begin{cases} \delta\theta(t) \triangleq \theta(t) - \bar{\theta}(t) \\ \delta\Omega_r(t) \triangleq \Omega_r(t) - \bar{\Omega}_r(t) \\ \delta v_{rot}(t) \triangleq v_{rot}(t) - \bar{v}_{rot}(t) \end{cases} \tag{2.23}$$

Note that the following notations have been introduced for the resulting partial derivatives of $F_{ax}(p(t))$ and $T_a(p(t))$ with respect to the considered operating point components:

$$\begin{cases} \nabla_\theta F_{ax}(\bar{p}(t)) \triangleq \left.\frac{\partial F_{ax}(p(t))}{\partial\theta(t)}\right|_{\bar{p}(t)} = \frac{1}{2}\rho\pi R^2 \bar{v}_{rot}(t)^2 \left.\frac{\partial C_T(\lambda(t),\theta(t))}{\partial\theta(t)}\right|_{\bar{p}(t)} \\ \nabla_{\Omega_r} F_{ax}(\bar{p}(t)) \triangleq \left.\frac{\partial F_{ax}(p(t))}{\partial\Omega_r(t)}\right|_{\bar{p}(t)} = \frac{1}{2}\rho\pi R^3 \bar{v}_{rot}(t) \left.\frac{\partial C_T(\lambda(t),\theta(t))}{\partial\lambda(t)}\right|_{\bar{p}(t)} \\ \nabla_{v_{rot}} F_{ax}(\bar{p}(t)) \triangleq \left.\frac{\partial F_{ax}(p(t))}{\partial v_{rot}(t)}\right|_{\bar{p}(t)} = \frac{1}{2}\rho\pi R^2 \bar{v}_{rot}(t) \left.\frac{\partial C_T(\lambda(t),\theta(t))}{\partial v_{rot}(t)}\right|_{\bar{p}(t)} \\ \nabla_\theta T_a(\bar{p}(t)) \triangleq \left.\frac{\partial T_a(p(t))}{\partial\theta(t)}\right|_{\bar{p}(t)} = \frac{1}{2}\rho\pi R^3 \bar{v}_{rot}^2 \left.\frac{\partial C_Q(\lambda(t),\theta(t))}{\partial\theta(t)}\right|_{\bar{p}(t)} \\ \nabla_{\Omega_r} T_a(\bar{p}(t)) \triangleq \left.\frac{\partial T_a(p(t))}{\partial\Omega_r(t)}\right|_{\bar{p}(t)} = \frac{1}{2}\rho\pi R^4 \bar{v}_{rot}(t) \left.\frac{\partial C_Q(\lambda(t),\theta(t))}{\partial\lambda(t)}\right|_{\bar{p}(t)} \\ \nabla_{v_{rot}} T_a(\bar{p}(t)) \triangleq \left.\frac{\partial T_a(p(t))}{\partial v_{rot}(t)}\right|_{\bar{p}(t)} = \frac{1}{2}\rho\pi R^3 \bar{v}_{rot}(t) \left.\frac{\partial C_Q(\lambda(t),\theta(t))}{\partial v_{rot}(t)}\right|_{\bar{p}(t)} \end{cases} \tag{2.24}$$

evaluated at the equilibrium working point $\bar{p}(t)$. Following this linearization procedure of the aerodynamic model, the overall entire turbine model described previously becomes suitable for linear controller design [40].

The Power Regulation and Rotor Speed Control Loop (PR/RSC)

The power regulation and rotor speed control loop is the most important loop in any wind turbine control system; it is aimed at ensuring that the wind turbine produces as much power as possible for partial-load conditions where, because of low rotor-effective wind speeds the rotor speed is below its rated value, and that it maintains the produced power to the maximum value allowed by the electrical generator for full-load conditions, where the variations in the

rotor speed around its defined rated value are restricted also for compliance with standards regarding associated loads and excessive noise generation. In Figure 12 a practical method of achieving this loop's goals is presented. In region Ø the rotor is idling i.e. the rotor speed is $\Omega_r(t) \cong \Omega_{r,min}$; this region can be interpreted as a range of wind speeds $v_{rot}(t)$ below some value v_{cutin} called the cut-in wind speed; when the turbine is in this regime, the pitch angle $\theta(t)$ is obtained from a look-up table as a function of the generator speed $\Omega_g(t)$ and the generator torque $T_{gen}(t)$ is kept at zero. When $v_{rot}(t)$ increases above v_{cutin} the rotor speed will also increase $\Omega_r(t) > \Omega_{r,min}$; then, the pitch angle $\theta(t)$ is fixed to the value corresponding to the maximum power coefficient $C_P(\lambda(t), \theta(t))$ and the controller starts modifying the generator torque so as to allow the rotor speed to reach an appropriate value corresponding to the tip-speed-ratio $\lambda(t) = \lambda_{opt}$ which allows for an optimum power coefficient to be achieved for the given fixed value of $\theta(t)$. This regime is denoted in Figure 12 by region I. Note that in terms of the rotor-effective wind speed, this regime can be thought of as the region where $v_{rot}(t)$ is between the values v_{cutin} and $v_{excl,low}$ as will be explained next.

Region II is arranged such that the transition between the individual control strategies corresponding to regions I and III is done as smoothly as possible so as to prevent excessive excitation of structural natural frequencies in the mechanical components. This is done by taking both strategies into account; because the PR/RSC control loop uses feedback on the estimated generator speed, the region's limits are defined in terms of some low and high exclusion rotor speeds, $\Omega_{r_{ex,l}}$ and $\Omega_{r_{ex,h}}$, respectively. For more details regarding the implemented strategy see [52]. For an interpretation of this region in terms of the rotor-effective wind speed, the values $\Omega_{r_{ex,l}}$ and $\Omega_{r_{ex,h}}$ can be (approximately) translated to $v_{excl,low} = \Omega_{r_{ex,l}} R/\lambda_{opt}$ and $v_{excl,high} = \Omega_{r_{ex,h}} R/\lambda_{opt}$, called low and high exclusion wind speeds, respectively.

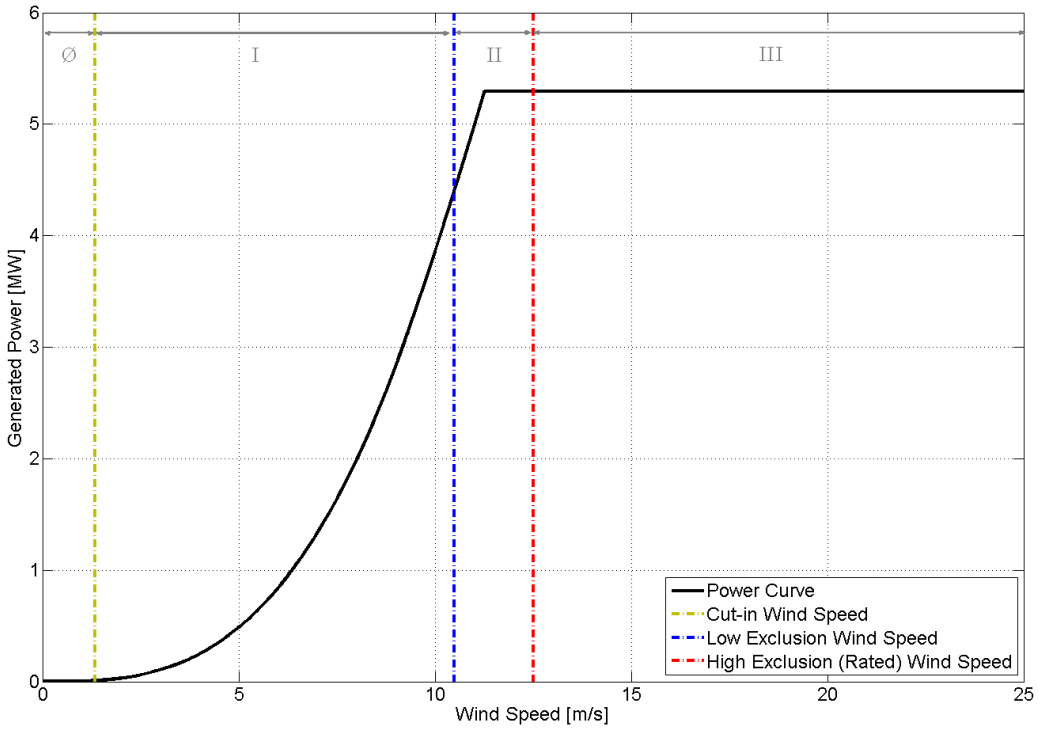

Figure 12: Power Curve and Possible Operation Regions for the ART 5 MW

In region III the rotor speed $\Omega_r(t)$ needs to be maintained at its rated value. The generator torque $T_{gen}(t)$ is already fixed at its maximum for the high power production. Here, the collective pitch angle of the blades $\theta(t)$ is controlled to maintain the amount of captured aerodynamic torque. In terms of the rotor-effective wind speed, this region could be interpreted as the zone where $v_{rot}(t)$ is between the values $v_{excl,high}$ and v_{cutout}.

By using the presented linearization technique, the following combined drivetrain and aerodynamic linear model arises for designing a controller that meets the mentioned goals of the PR/RSC control loop:

$$\begin{bmatrix} \delta\dot{\Omega}_r(t) \\ \delta\dot{\Omega}_r^{int}(t) \end{bmatrix} = A_{PR/RSC}(\bar{p}(t)) \begin{bmatrix} \delta\Omega_r(t) \\ \delta\Omega_r^{int}(t) \end{bmatrix} + B_{u,PR/RSC}(\bar{p}(t)) \begin{bmatrix} \delta\theta(t) \\ \delta T_{gen}(t) \end{bmatrix} + B_{w,PR/RSC}(\bar{p}(t))(\delta v_{rot}(t) - \delta\dot{x}_{FA}(t)) \tag{2.25}$$

with matrices:

$$\begin{cases} A_{PR/RSC}(\bar{p}(t)) &= \begin{bmatrix} \frac{(1-T_T)\nabla_{\Omega_r} T_a(\bar{p}(t)) - T_V}{i_{tr}^2 J_g + J_r} & 0 \\ 1 & 0 \end{bmatrix} \\ B_{u,PR/RSC}(\bar{p}(t)) &= \begin{bmatrix} \frac{(1-T_T)\nabla_\theta T_a(\bar{p}(t))}{i_{tr}^2 J_g + J_r} & -\frac{|i_{tr}|}{i_{tr}^2 J_g + J_r} \\ 0 & 0 \end{bmatrix} \\ B_{w,PR/RSC}(\bar{p}(t)) &= \begin{bmatrix} \frac{(1-T_T)\nabla_{v_{rot}} T_a(\bar{p}(t))}{i_{tr}^2 J_g + J_r} \\ 0 \end{bmatrix} \end{cases} \tag{2.26}$$

As mentioned, two separate controllers are built based on this model by taking into account the necessities of their corresponding operating regions, as previously described. Due to the fact that all signals in this model are available as measurements or through the presented observers, the control architecture that will be most suitable is state-feedback control; in [52] the design is performed by using the linear quadratic regulator (LQR) methodology [5]. For region I the control signal will be given by:

$$T_{gen}(t) = \begin{bmatrix} K_P^{I,PR/RSC} & K_I^{I,PR/RSC} \end{bmatrix} \begin{bmatrix} \delta\hat{\Omega}_r(t) \\ \delta\hat{\Omega}_r^{int}(t) \end{bmatrix} \tag{2.27}$$

whereas for region III this will be:

$$\theta(t) = \begin{bmatrix} K_P^{III,PR/RSC} & K_I^{III,PR/RSC} \end{bmatrix} \begin{bmatrix} \delta\hat{\Omega}_r(t) \\ \delta\hat{\Omega}_r^{int}(t) \end{bmatrix} \tag{2.28}$$

In both cases, $\delta\hat{\Omega}_r^{int}(t) = \int_0^t \delta\hat{\Omega}_r(\tau)dt$ while $\delta\hat{\Omega}_r(t)$ is obtained from the estimates provided by the *Drivetrain Dynamics Observer*. As can be observed, both (2.27) and (2.28) are PI controllers with respect to the estimated rotor speed. Notice that as the operating equilibrium point changes $\bar{p}(t)$, some of the parameters in the state-space model (2.26) will also change. To account for this in the control design, the controller parameters would need to be scheduled based on the variation of the equilibrium operating point. For the controller (2.27) this is not necessary as it operates in a sufficiently narrow region to consider the model computed at:

$$\bar{p}(t) = p_{cutin} = \begin{bmatrix} \theta(v_{cutin}) & \Omega_r(v_{cutin}) & v_{cutin} \end{bmatrix}^T \tag{2.29}$$

representative for the entire region; however, the controller (2.28) is designed for some $v_{high} \gg v_{excl,high}$ yielding:

$$\bar{p}(t) = p_{high} = \begin{bmatrix} \theta(v_{high}) & \Omega_r(v_{high}) & v_{high} \end{bmatrix}^T \tag{2.30}$$

and gain-scheduled between $v_{excl,high}$ and v_{cutout}.

The Active Drivetrain Damping Control Loop (DriD)

The active drivetrain damping control loop is aimed at reducing fatigue loads in the components of the drivetrain; this can be achieved by controlling the generator torque $T_{gen}(t)$ so as to reduce the magnitude of the shaft torsion angle $\gamma(t)$; note that since estimates of both $\gamma(t)$ and $\dot{\gamma}(t)$ are available from the *Drivetrain Dynamics Observer* this can be achieved through the state-feedback PD control law with respect to the estimated shaft torsion angle:

$$\delta T_{gen}(t) = \begin{bmatrix} K_P^{DriD} & K_D^{DriD} \end{bmatrix} \begin{bmatrix} \delta\hat{\gamma}(t) \\ \delta\dot{\hat{\gamma}}(t) \end{bmatrix} \tag{2.31}$$

with small deviations $\delta T_{gen}(t)$ around the values of $T_{gen}(t)$ set by the PR/RSC controller. The state-feedback controller is arrived at by using the LQR design methodology [5], based on the linear model:

$$\begin{bmatrix} \delta\dot{\gamma}(t) \\ \delta\ddot{\gamma}(t) \end{bmatrix} = A_{DriD} \begin{bmatrix} \delta\gamma(t) \\ \delta\dot{\gamma}(t) \end{bmatrix} + B_{u,DriD}\delta T_{gen}(t) + B_{w,DriD}(\bar{p}(t))\delta v_{rot}(t). \tag{2.32}$$

with matrices:

$$\begin{cases} A_{DriD} & = & \begin{bmatrix} 0 & 1 \\ -\frac{s_{dt}}{m_{dt}} & -\frac{d_{dt}}{m_{dt}} \end{bmatrix} \\ B_{u,DriD} & = & \begin{bmatrix} 0 \\ \frac{|i_{tr}|}{i_{tr}^2 J_g} \end{bmatrix} \\ B_{w,DriD}(\bar{p}(t)) & = & \begin{bmatrix} 0 \\ \frac{\nabla_{v_{rot}} T_a(\bar{p}(t))}{J_r} \end{bmatrix} \end{cases} \tag{2.33}$$

Note that although $B_{w,DriD}(\bar{p}(t))$ does change with the equilibrium operating point, no further design measure is taken [52].

The Active Fore-Aft Tower Damping Control Loop (TowD)

Finally, the active fore-aft tower damping control loop is aimed at reducing fatigue loads in the wind turbine support structure; this is done by controlling the collective blade pitch angle $\theta(t)$ and adjusting the aerodynamic damping so as to reduce the motion of the tower top; given that estimates of the fore-aft tower top position $x_{FA}(t)$ and the fore-aft tower top velocity $\dot{x}_{FA}(t)$ are available from the *Tower Fore-Aft Dynamics Observer* this can be achieved through the state-feedback PD control law with respect to the estimated tower top position:

$$\delta\theta(t) = \begin{bmatrix} K_P^{TowD} & K_D^{TowD} \end{bmatrix} \begin{bmatrix} \delta\hat{x}_{FA}(t) \\ \delta\dot{\hat{x}}_{FA}(t) \end{bmatrix} \tag{2.34}$$

by small deviations $\delta\theta(t)$ around the values of $\theta(t)$ set by the PR/RSC controller. The state-feedback controller arrived at is again designed using the LQR methodology [5], based on the linear model:

$$\begin{bmatrix} \delta\dot{x}_{FA}(t) \\ \delta\ddot{x}_{FA}(t) \end{bmatrix} = A_{TowD}(\bar{p}(t)) \begin{bmatrix} \delta x_{FA}(t) \\ \delta\dot{x}_{FA}(t) \end{bmatrix} + B_{u,TowD}(\bar{p}(t))\delta\theta(t) + B_{w,TowD}(\bar{p}(t))\delta v_{rot}(t). \tag{2.35}$$

with matrices:

$$\begin{cases} A_{TowD}(\bar{p}(t)) &= \begin{bmatrix} 0 & 1 \\ -\frac{s_t}{m_t} & -\frac{d_t+\nabla_{v_{rot}}F_{ax}(\bar{p}(t))\left(1+\frac{R^2}{2H^2}\right)}{m_t} \end{bmatrix} \\ B_{u,TowD}(\bar{p}(t)) &= \begin{bmatrix} 0 \\ \frac{\nabla_\theta F_{ax}(\bar{p}(t))}{m_t} \end{bmatrix} \\ B_{w,TowD}(\bar{p}(t)) &= \begin{bmatrix} 0 \\ \frac{\nabla_{v_{rot}} F_{ax}(\bar{p}(t))}{m_t} \end{bmatrix} \end{cases} \tag{2.36}$$

where H represents the tower top height. Note that some of the parameters of the matrices (2.36) change with the equilibrium operating point $\bar{p}(t)$, thus for efficient tower damping control gain-scheduling on the control gains computed at a given operating point (2.30) may be applied [52].

Note that some of the frequency content of the control signal $\delta\theta(t)$ given by the active tower damping controller needs to be filtered before adding it to $\theta(t)$. One of the reasons for this is that it is not desirable to have pitching activity at the main frequency peaks (e.g. 3P, 6P and 9P for the considered case) in the power spectra of the estimates $\delta\hat{x}_{FA}(t)$ and $\delta\hat{\dot{x}}_{FA}(t)$, introduced by the rotational sampling effect and tower shadow; to this end, this is achieved by using notch filters. Furthermore, these estimates are biased and their average value also needs to be removed, which can be achieved by making use of a (high-pass) lead-lag filter. For more details regarding the design of the filters see [52].

2.4 Conclusions

In this chapter one approach towards wind turbine control has been presented, from both the conceptual and the design point of view. The exposition has been triggered by the control-relevant aspects of the wind. Subsequently, models for the main subsystems within a wind turbine have been given with remarks being made regarding their suitability for feedback control and also for simulation. Based on these models, several important algorithms that can reconstruct missing information regarding wind turbine operation have been described. Finally, it has been shown how the closed-loop control can be achieved using by making explicit use of this retrieved information. Figure 13 gives an overview of the presented material.

Although state-of-the-art in terms of implementation as well as very accessible for design, the presented framework could provide suboptimal results if the employed models do not accurately represent the wind turbine behaviour. This can occur in many practical situations given the fact that design uncertainty regarding this behaviour always exists as would be, for instance, if the aerodynamic properties of the rotor would differ from the design due to e.g. manufacturing, ice accretion, blade erosion or dirt-buildup; as a similar case, the support structure dynamics considered during the design could be different from the real-life ones due to e.g. installation, marine sand dunes, scour or biofouling. Because these situations, all formulated in the goals of the thesis, are usually disregarded during the design phase and, in general, control systems do not make explicit use of online-available information regarding the wind turbine behaviour, it can be said that *uncertainty* regarding the operational performance is introduced through *design*. The next chapter is focused on analyzing such situations from the introduced controls perspective.

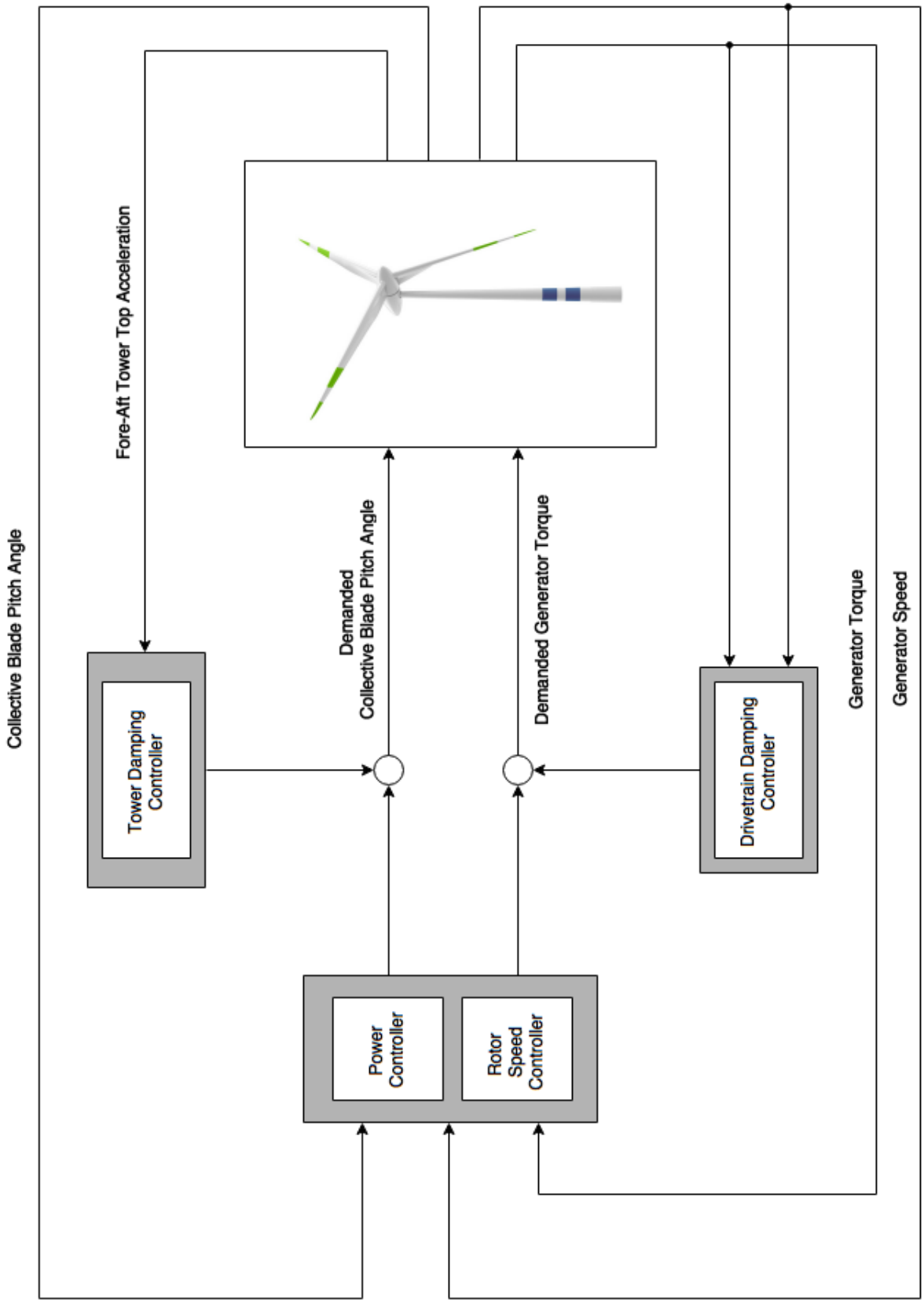

Figure 13: Overview of the Proposed Wind Turbine Control Loops

3

Design Uncertainty and Wind Turbine Control Performance

In this chapter, the potential effects of wind turbine design uncertainty on control system performance are presented in relation to the formulated goals of the project. An overview of the design process followed by manufacturers and the subsequent certification procedure is first given to show when such uncertainty arises and how it is typically dealt with. The discussion is then moved to analyzing the behaviour of the aerodynamic subsystem and the wind turbine support structure, whose properties can change during the operational lifetime of the turbine. The chapter is concluded with a firm solution choice towards addressing the identified problems within the framework of this project.

3.1 Wind Turbine Design and Certification

The process of designing a wind turbine is started by the formulation of a set of detailed technical specifications that describe the desired performance of the final product; some of these specifications are firm, whereas others can be adjusted during the design. Additional to these, more generic system requirements regarding e.g. safe operation and environmental compliance that arise from standardization organizations such as Germanischer Lloyd (GL), Det Norske Veritas (DNV) or, more recently, the International Electrotechnical Commission (IEC), are translated into extra specifications; examples are the IEC 61400-1 standard that applies for large onshore wind turbines [24], the IEC 61400-3 for offshore wind turbines [27], the 61400-13 TS that stipulates the measurement of generic mechanical loads for wind turbines [23] and the IEC 61400-25 concerned with monitoring and control of wind turbines [25]. During the entire design process, which itself is very involved, many choices and trade-offs are made to satisfy all the specifications as well as possible, especially the ones regarding safe operation; in turn, all these decisions do have an effect of the performance of the final product when used in real life [21].

After the design is finished, the product needs to be certified according to e.g. [59, 2, 93, 26] before it can be marketed or even built and installed for power production purposes [63]. For certification, both simulation data and test data, especially from laboratory testing, will be used. An overview of the combined typical design and certification process is offered in Figure 14. As shown, starting from the mentioned list of specifications, the design process is started. After successful completion of the first stage, the design arrived at is extensively simulated to ensure that it satisfies the specifications; based on the simulation results, the design is re-iterated until the specifications are met as well as possible. Because during this initial design stage limited information regarding the expected behaviour of the final product over its entire lifetime is available, on one hand, and because the simulations will not fully represent the future

product's real-life behaviour, turbine designers will typically use large safety factors to have some *a priori* guarantee that in practice the product will also meet the performance seemingly indicated by the design and simulation codes; the use of such conservative safety factors will consequently either increase the production costs for the wind turbine due to e.g. use of more or different materials, decrease its performance due to e.g. larger inertias or even both.

Subsequent to the first design and simulation stage is laboratory testing and system certification. First, based on a scale-model of the designed wind turbine, laboratory tests are made to ensure that the simulated behaviour has indeed been somewhat representative of the important aspects of the real-life behaviour. The success of this stage could allow turbine designers to reduce the mentioned safety factors *a posteriori*, although not considerably as this would imply extensive re-iterations. As mentioned, together with the initial product specifications, relevant collected data from simulations and practical tests is used further for system certification. The final product development stage is typically aimed to take place in a setting as close as possible to the one of the final product; these tests can only rarely introduce further design re-iterations. After the successful completion of this final stage, the product can be manufactured on large-scale and used for power production. Notice that the cost of the final product is largely fixed by the early design phases and the associated safety factors.

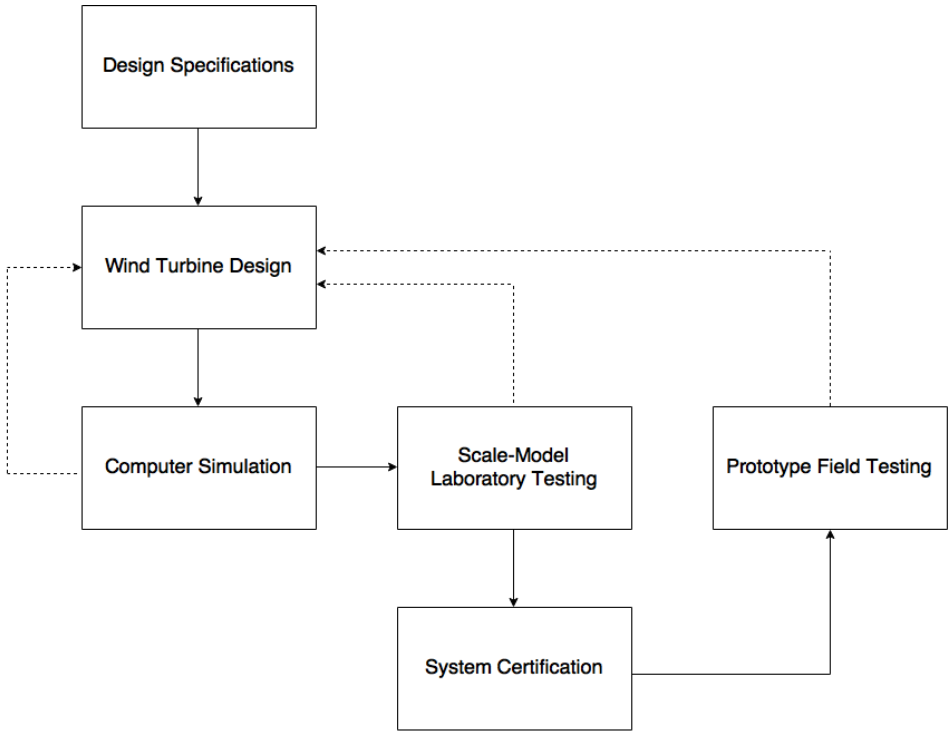

Figure 14: Overview of the Wind Turbine Design and Certification Process

What is more, the design of wind turbines placed in hostile environments such as e.g. at sea or in deserted mountainous areas is generally known to imply the use of much larger safety factors than the ones for normal environments [63, 62]; this is because of the fact that the turbines need to have some extra form of robustness in operation in such environments so as to allow for increased uptime and limited maintenance. These safety factors can potentially be reduced if during the early phases of the design knowledge regarding the environment itself is incorporated in the design process so as to understand to what extent system performance is affected by the physical factors that introduce uncertainty and to further refine the design algorithms. Furthermore, similarly incorporated information regarding how the different subsystems change their behaviour during the turbine lifetime due to e.g. aging can also help reduce the safety factors by an improved design. In general, it is the subsystems that are directly exposed to external factors i.e. the aerodynamic subsystem and the turbine support structure that will experience changes throughout the turbine lifetime, both due to environmental conditions as well as aging, as will be explained in this chapter.

3.2 Effects of Aerodynamic Design Uncertainty

The aerodynamic subsystem, although being one of the parts of a wind turbine whose development requires both the largest amount of coordinated engineering effort and state-of-the-art design and simulation codes, is also the subsystem whose behaviour is most uncertain [63]; this is due to the fact that the aerodynamic properties of the blades are sensitive to even small changes in blade geometry or atmospheric conditions [21]. Even though manufacturers aim to deliver blades that are as close as possible in terms of aerodynamic characteristics to the designs, in practice this is never perfectly achieved [66]. Moreover, throughout a wind turbine's lifetime, the blades will suffer the effects of being exposed to the environment: dust particles in the air and contact with insects will form layers of dirt on them changing the surface roughness, potential impact with larger objects or birds will cause blade erosion (Figure 16) and the blade geometry will change due to aging of the blade materials [62]. What is more, ice accretion on turbine rotors (Figure 15) is a phenomenon that can happen during the cold season of the year, at geographical locations close to the Arctic circle or in hostile environments such as offshore [85, 15]; this has been reported to be the one whose effects on wind turbine aerodynamics have the largest proportions [60].

Figure 15: Ice Accretion on a Turbine Rotor

Figure 16: Erosion on a Turbine Blade

Currently, wind energy research institutes are concerned with understanding the atmospheric conditions that enable the appearance of ice on wind turbine blades [85]. In Figure 17 an ice formation risk map for European wind farms is presented and shows that whereas in a majority of locations there is some danger of ice formation, many places where dedicated measurement stations were part of wind farms do have an increased risk [15].

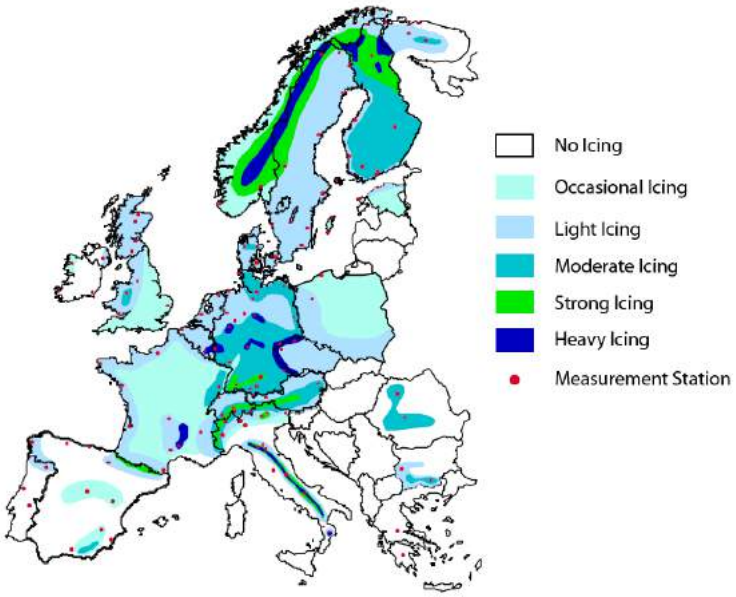

Figure 17: Map of Wind Turbine Ice Formation Risk in Europe

Ice formation on wind turbine rotors is known to be both very dangerous for the turbine operation and its surroundings due to e.g. ice throw and blade mass imbalance [18], respectively, as well as a contributing factor to suboptimal power performance [46, 45]. Recent studies [85, 56, 36] have shown the relation between the blade geometry and the expected associated ice accretion geometry if the atmospheric conditions are favourable for ice formation and have concluded that for any given blade, two ice accretion profiles are possible regarding the blade leading edge shape, namely the *elongated leading edge ice profile* and the *branched leading edge ice profile*, see [36] for more information.

Analysis with the Elongated Leading Edge Ice Profile

The elongated leading edge ice profile (denoted from here onwards by ICE-01) represents the accretion of ice around the leading edge in each of the airfoils of a turbine blade in such a way that the aerodynamic chord becomes larger whereas the leading edge geometry as well as the airfoil thickness remains the same; the accretion is caused by cold water particles on the blade moving towards the leading edge due to the centrifugal force created by the blade rotation; for this case, the motion of the particles is undisturbed by wind turbulence which will give rise to the presented accretion geometry [36].

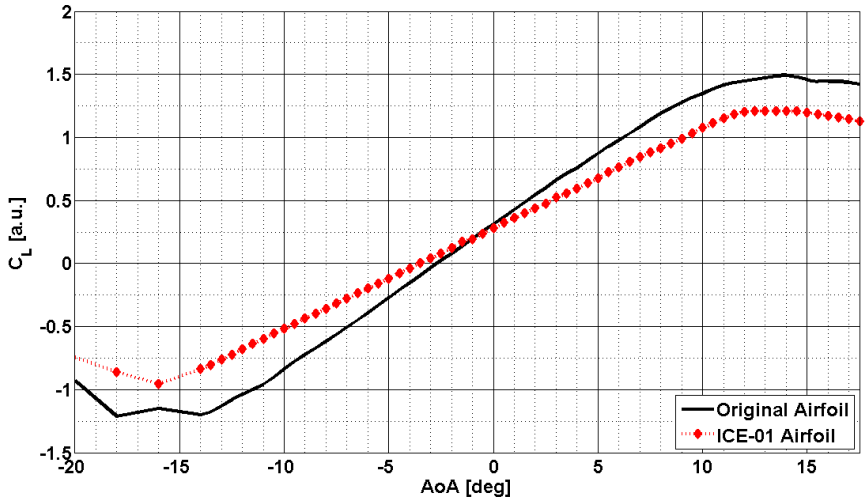

Figure 18: Comparison of Clean and Iced (ICE-01) Lift Characteristic $C_L(AoA)$ for the NACA63418 Airfoil

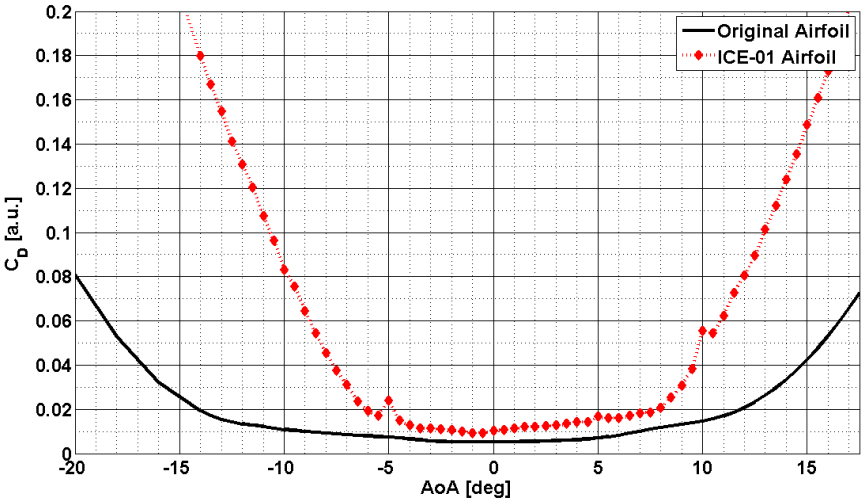

Figure 19: Comparison of Clean and Iced (ICE-01) Drag Characteristic $C_D(AoA)$ for the NACA63418 Airfoil

The effects on the airfoil lift coefficient and drag coefficient characteristic curves depends on both the amount of ice formation as well as the accretion geometry, however, for a proposed situation [36] it can be observed from Figure 18 and Figure 19 that in general, the airfoils will have less achievable lift in the positive angle-of-attack (AoA) region whereas the drag will tend to be more pronounced. Moreover, the airfoils will tend to stall at lower AoAs, although this effect is only mild. The airfoil moment coefficient characteristic curves is claimed to remain unchanged [36].

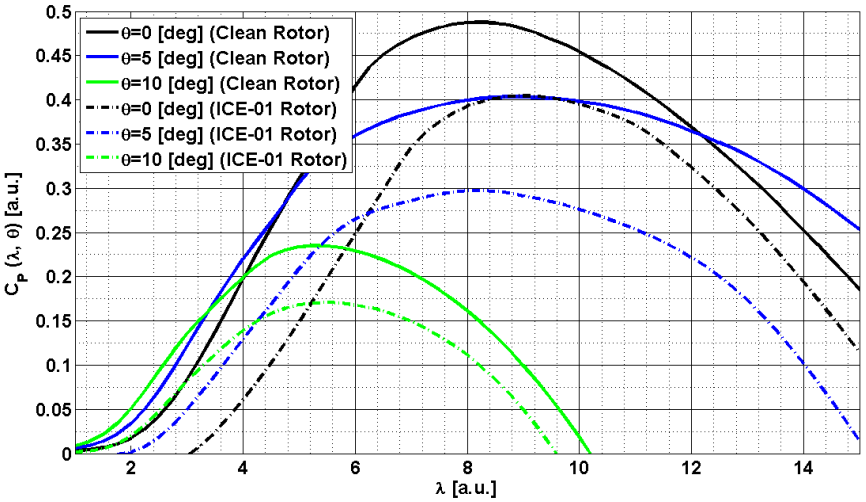

Figure 20: Comparison of Clean and Iced (ICE-01) Rotor Power Coefficient Curves $C_P(\lambda, \theta)$ for the ART 5 MW Rotor

For the ART 5 MW rotor (see [48] and **Appendix B** for details) the original C_L and C_D characteristics for each airfoil are modified similarly to the results shown in Figure 18 and Figure 19. Then using the aeroelastic simulation code FOCUS (see [58] and the references therein for further information and a full tutorial) the power C_P and thrust C_T coefficients are calculated for the iced rotor. These are shown in Figure 20 and Figure 21, respectively; as can be seen, both characteristics are affected by the accretion of ice.

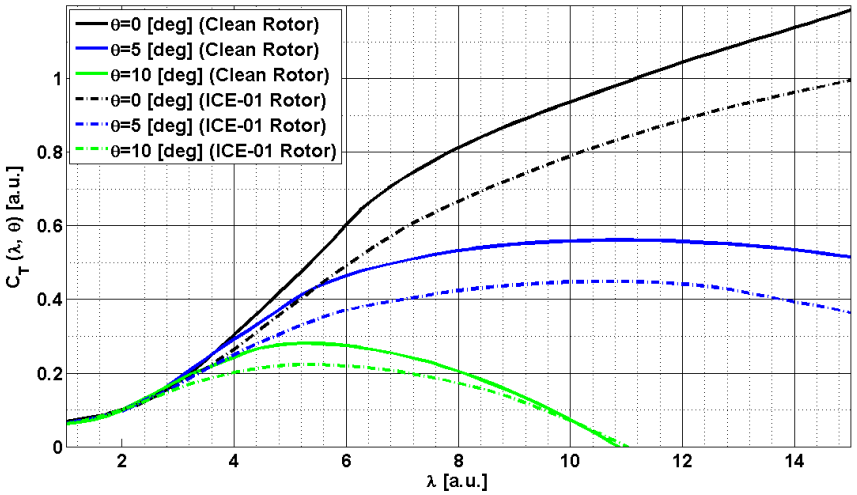

Figure 21: Comparison of Clean and Iced (ICE-01) Rotor Thrust Coefficient Curves $C_T(\lambda, \theta)$ for the ART 5 MW Rotor

In Table 1 these effects are summarized for the rotor power coefficient, especially relevant for control design. As indicated, the maximum power for the iced rotor (ICE-01 Rotor) is lower than for the nominal rotor (Clean Rotor); moreover, the location of the maximum is changed with respect to the collective blade pitch angle. Given the fact

that at below-rated rotor-effective wind speeds, the blade pitch angle is fixed to its supposed value that corresponds to the maximum C_P, this would seem to indicate that the power production in partial-load will drop by at least 17%. In Figure 22 a comparison between the derivatives of the aerodynamic torque with respect to variations in the collective pitch angle for the clean and iced rotor of the ART 5 MW are shown, as a function of the rotor-effective wind speed; as can be seen, these derivatives remain largely the same at below-rated wind speeds, yet differ significantly at above-rated wind speeds.

	Clean Rotor	ICE-01 Rotor
Maximum Value [a.u.]	0.4904	-17.35%
$\boldsymbol{\theta_{opt}}$ **[deg]**	$+1$	-1
$\boldsymbol{\lambda_{opt}}$ **[a.u.]**	8.75	8.75

Table 1: Comparison of Power Coefficient Curve Properties for the Clean Rotor and the Iced (ICE-01) Rotor of the ART 5 MW

In Figure 23 the ART 5 MW is simulated with one specific wind realization characterized by below-rated rotor-effective mean wind speeds. Indeed, in the case of an iced rotor, the power production is lower: the rotor speed will be lower than for the case of a clean rotor, on one hand because the PR/RSC control loop will keep the collective blade pitch angle to its considered optimum location and, on the other because the lower values of torque coefficient triggered by the mentioned changes in the C_P characteristic imply that the wind resource can be used less efficiently with such a rotor.

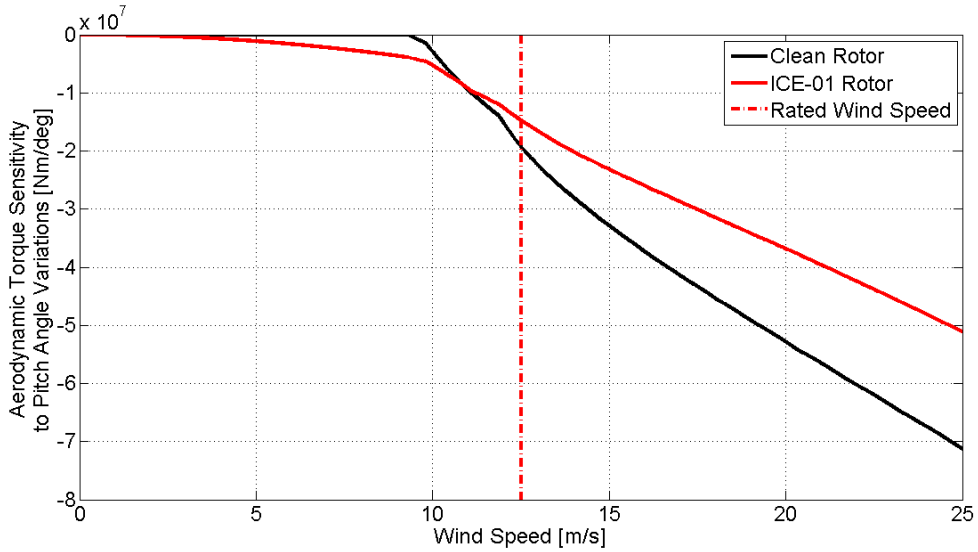

Figure 22: Aerodynamic Torque Derivatives with respect to Pitch Angle for the Clean and the Iced (ICE-01) Rotor of the ART 5 MW

By observing the simulation results presented in Figure 24 depicting full-load simulation of the same wind turbine, it can be noticed that even though the model used for the design of the PR/RSC loop (2.25) and (2.26) is more severely affected in this operating region by ice accretion, due to the aerodynamic torque derivative shown in Figure 22, the loop performs well and, in general, the difference in the yielded power is small compared to the case of a clean rotor. Hence, though the model used for the design of the PR/RSC loop in above-rated conditions (region III) is computed at some wind speed above-rated according to (2.30) and, as Figure 22 shows, the difference between the expected value of $\nabla_\theta T_a(\bar{p}(t))$ (clean rotor) and the true one (iced rotor) is around 25%, it is the fact that the values of $\nabla_\theta T_a(\bar{p}(t))$ are in fact higher for the iced rotor than for the clean rotor that still enables appropriate power production. Moreover, the small existing power production loss shown in Figure 24 is actually due to the PR/RSC controller reducing the generator torque when the rotor-effective wind drops below the rated value, so as to allow the rotor motion to be maintained close it its rated speed. For the ice profile ICE-01 it can be concluded that only the partial-load operation is affected due to the change in optimum C_P location with respect to the collective pitch angle.

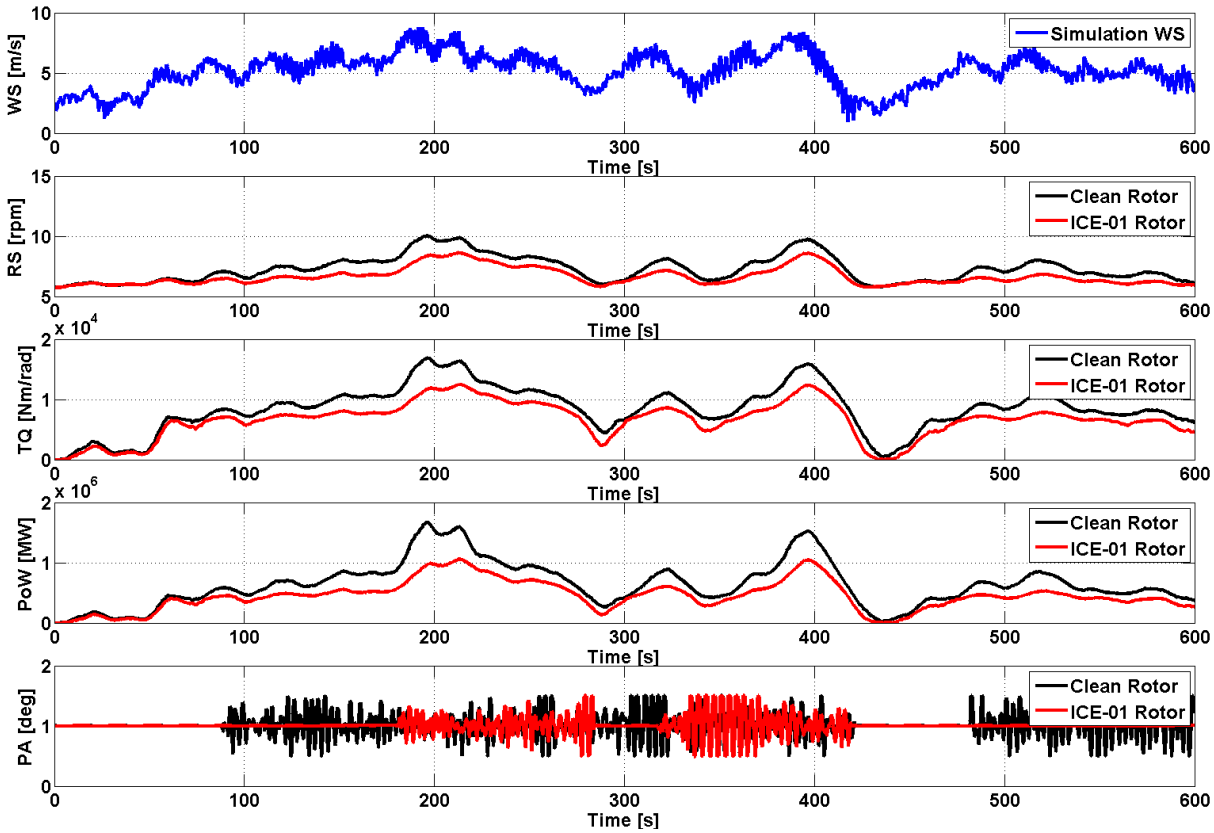

Figure 23: Time Series Simulation for Partial-Load Conditions with Clean and Iced (ICE-01) Rotor for the ART 5 MW

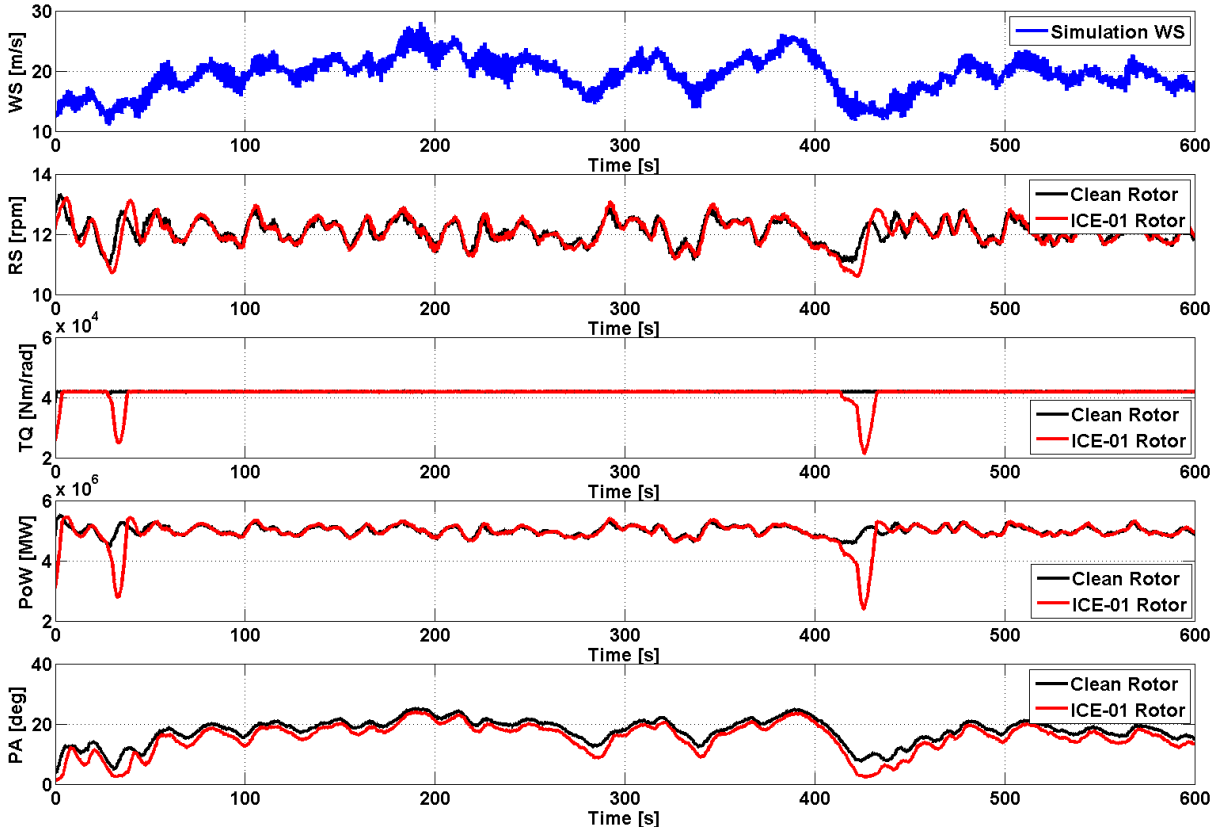

Figure 24: Time Series Simulation for Full-Load Conditions with Clean and Iced (ICE-01) Rotor for the ART 5 MW

Analysis with the Branched Leading Edge Ice Profile

Similar to the previous analysis, the bifurcated leading edge ice profile represents the accretion of ice around the leading edge in each of the airfoils of a turbine blade such that the aerodynamic chord as well as the airfoil thickness remain unchanged. However, here the leading edge geometry is severely affected as the cold water particles on the blade that move towards the leading edge during blade rotation are in this case considered to encounter wind turbulence which will cause a branched-type of ice geometry around the leading edge (in fact, two small portions of ice are formed around the bifurcated leading edge); this ice profile will further be denoted by ICE-02 and the analysis follows in the lines proposed in [36].

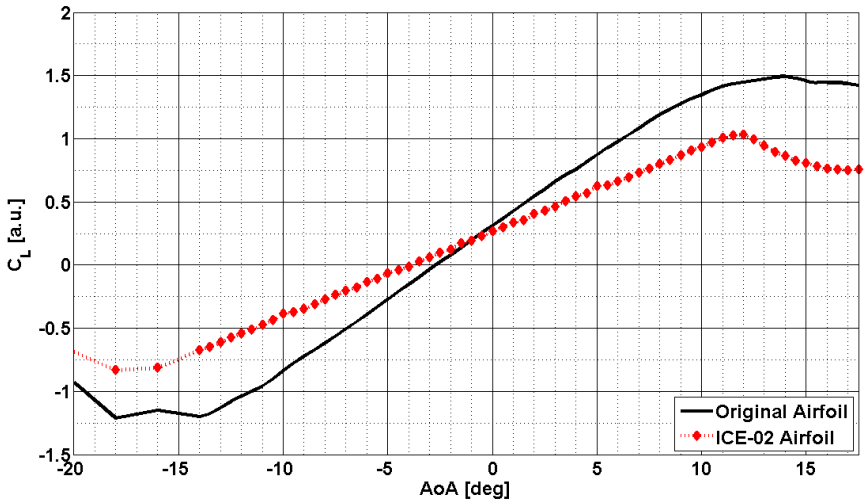

Figure 25: Comparison of Clean and Iced (ICE-02) Lift Characteristic $C_L(AoA)$ for the NACA63418 Airfoil

As can be observed in Figure 25 and Figure 26, for the case of this ice profile the lift and drag characteristics are more severely affected than in the case of the elongated leading edge ice profile. The C_L coefficient will have lower values for the positive AoA region important for turbine operation, yet the airfoils will stall at lower AoAs and the phenomenon will be more pronounced than in the case of the ICE-01 profile; yet again, the C_D characteristic will show that the airfoil drag is higher than the one for a clean airfoil for both positive and negative AoAs.

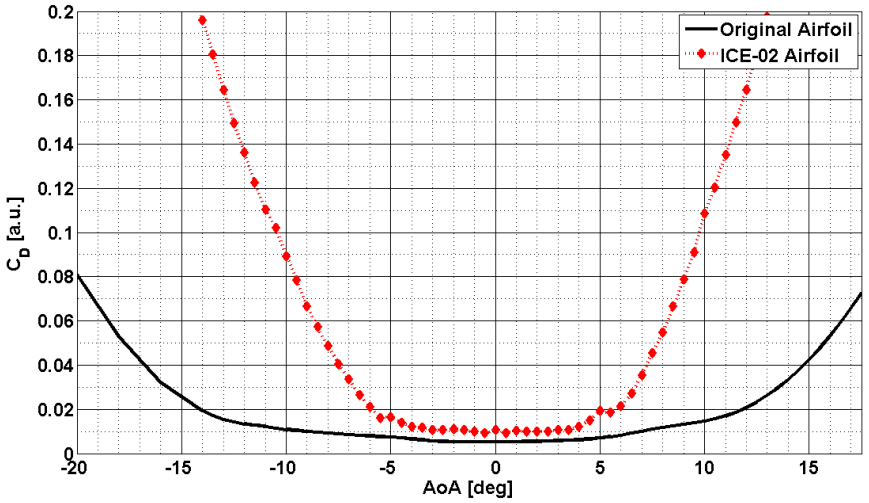

Figure 26: Comparison of Clean and Iced (ICE-02) Drag Characteristic $C_D(AoA)$ for the NACA63418 Airfoil

When the effect of branched leading edge ice accretion is applied to the ART 5 MW rotor airfoils and the C_P and C_T curves are calculated with FOCUS, it can be observed from Figure 27 and Figure 28 that the iced rotor behaviour in terms of the blade pitch angle and tip-speed-ratio is very different from the one of the nominal rotor. In general, both lower C_P and lower C_T are seen for the entire considered tip-speed-ratio range.

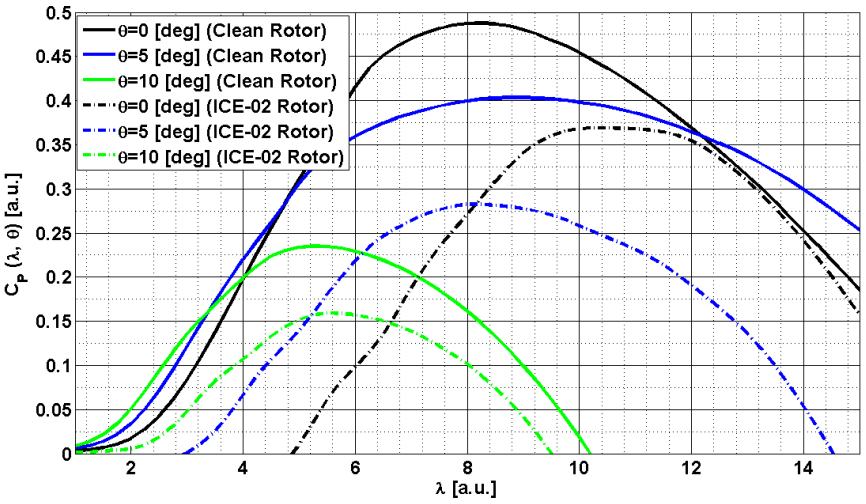

Figure 27: Comparison of Clean and Iced (ICE-02) Rotor Power Coefficient Curves $C_T(\lambda, \theta)$ for the ART 5 MW Rotor

The control-relevant aspects of the C_P curve are summarized in Table 2. As can be seen, for this ice profile the optimum pitch angle remains unchanged for the power coefficient curve, however the optimal tip-speed-ratio for the entire rotor will be changed to higher values. The magnitude of the maximum C_P is even smaller than in the case of the elongated leading edge ice profile. In Figure 29 a comparison between the aerodynamic torque derivatives with respect to the collective blade pitch angle is shown as a function of the rotor-effective wind speed. As can be observed, for the case of ICE-02 accretion profile, the values of $\nabla_\theta T_a(\bar{p}(t))$ are very different between the clean and the iced rotor for the entire range of operational wind speeds.

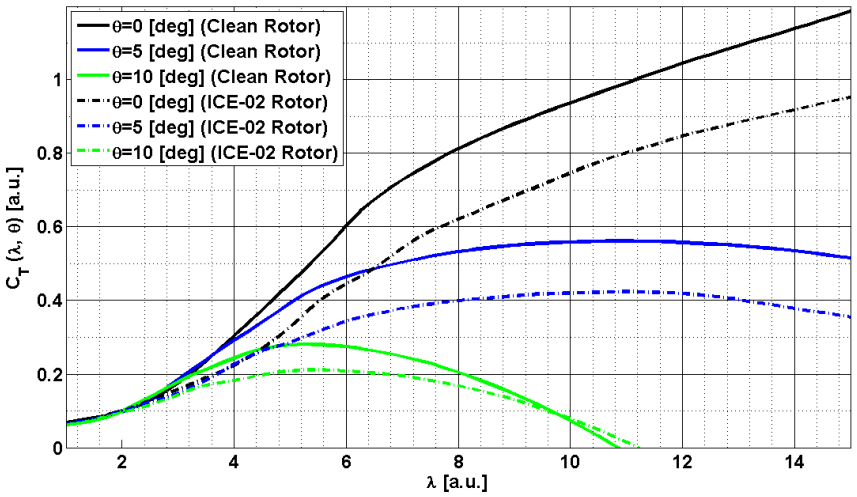

Figure 28: Comparison of Clean and Iced (ICE-02) Rotor Thrust Coefficient Curves $C_T(\lambda, \theta)$ for the ART 5 MW Rotor

In Figure 30, where the ART 5 MW is simulated with the same wind realization with below-rated rotor-effective mean wind speeds, the PR/RSC control loop designed for a turbine with clean rotor appears to keep the pitch angle to its

	Clean Rotor	ICE-02 Rotor
Maximum Value [a.u.]	0.4904	-22.35%
θ_{opt} **[deg]**	$+1$	$+1$
λ_{opt} **[a.u.]**	8.75	10.75

Table 2: Comparison of Power Coefficient Curve Properties for the Clean Rotor and the Iced (ICE-02) Rotor of the ART 5 MW

optimum value for the entire simulation: this is because the turbine rotor never reaches its rated speed. Moreover, overall power production is very low due to the reduced achieved rotor speed and, would be higher if the PR/RSC controller would be able to achieve higher values of the tip-speed-ratio. However, the new airfoil geometries do not seem to allow for sufficient aerodynamic torque.

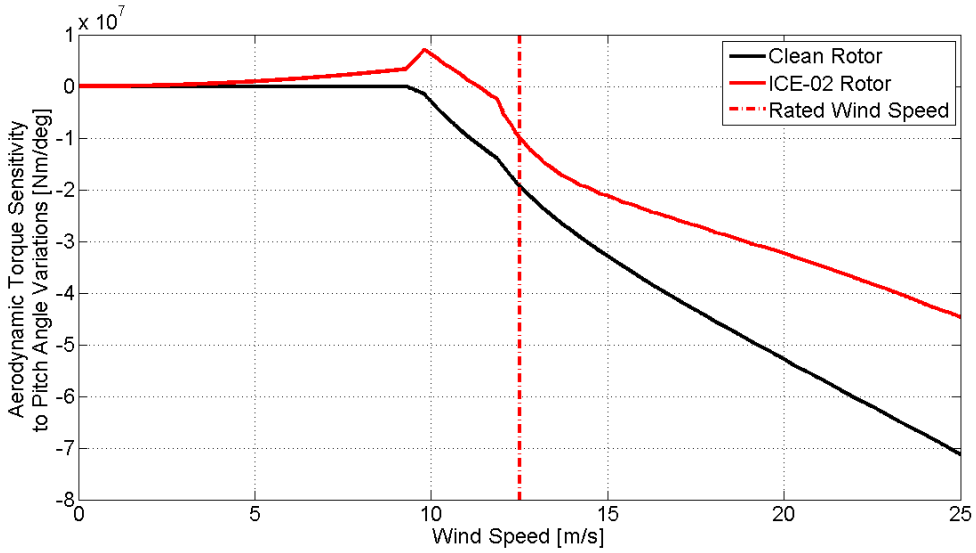

Figure 29: Aerodynamic Torque Derivatives with respect to Pitch Angle for the Clean and the Iced (ICE-02) Rotor of the ART 5 MW

It is interesting to observe that for full-load simulated rotor-effective mean wind-speeds, the rotor speed will also drop due to the severely limited energy capturing behaviour and, although the electrical generator torque is indeed kept low, the rotor speed will still not be able to become higher. The wind turbine, when close to idling, will try to start up due to the acknowledgment of appropriate wind potential. However, the start-up control algorithm [52] briefly introduced in the previous chapter will not be able to cope with such changes in the expected turbine behaviour and will, therefore, not be able to start the wind turbine.

As has been observed, ice accretion on wind turbine blades, either in the form of elongated leading edge accretion or branched leading edge accretion, will cause losses in terms of power production. Whereas for the elongated leading edge ice profile the losses, due to a change in the optimum pitch angle to some extent and also due to perturbed power coefficient characteristic, were prominent in partial-load conditions, for the branched leading edge ice profile the losses are present in partial-load operation and are even severe in full-load operation due to the more pronounced changes in the C_P characteristic, including the location of the optimum tip-speed-ratio. These indicate that the PR/RSC control loop could be redesigned so as to be able to cope with this situation. Similarly, these mentioned changes of the rotor characteristics also have the potential to alter the performance of the DriD and TowD control loops, given the fact that parameters that account for the aerodynamic properties of the turbine do appear in their respective models used for loop design. During the performed analysis, however, no problems have been found regarding these two loops. Several remarks regarding the possibilities for addressing the detected issues are made at the end of this thesis.

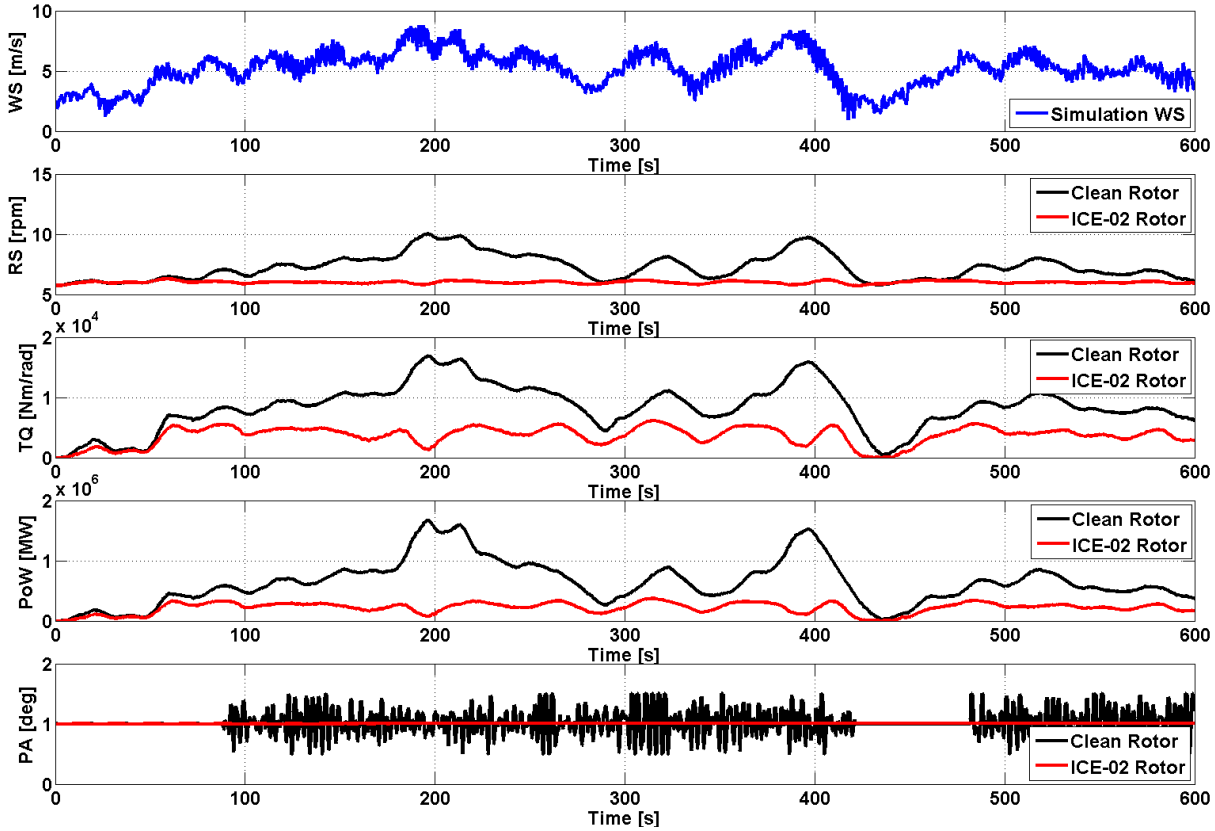

Figure 30: Time Series Simulation for Partial-Load Conditions with Clean and Iced (ICE-02) Rotor for the ART 5 MW

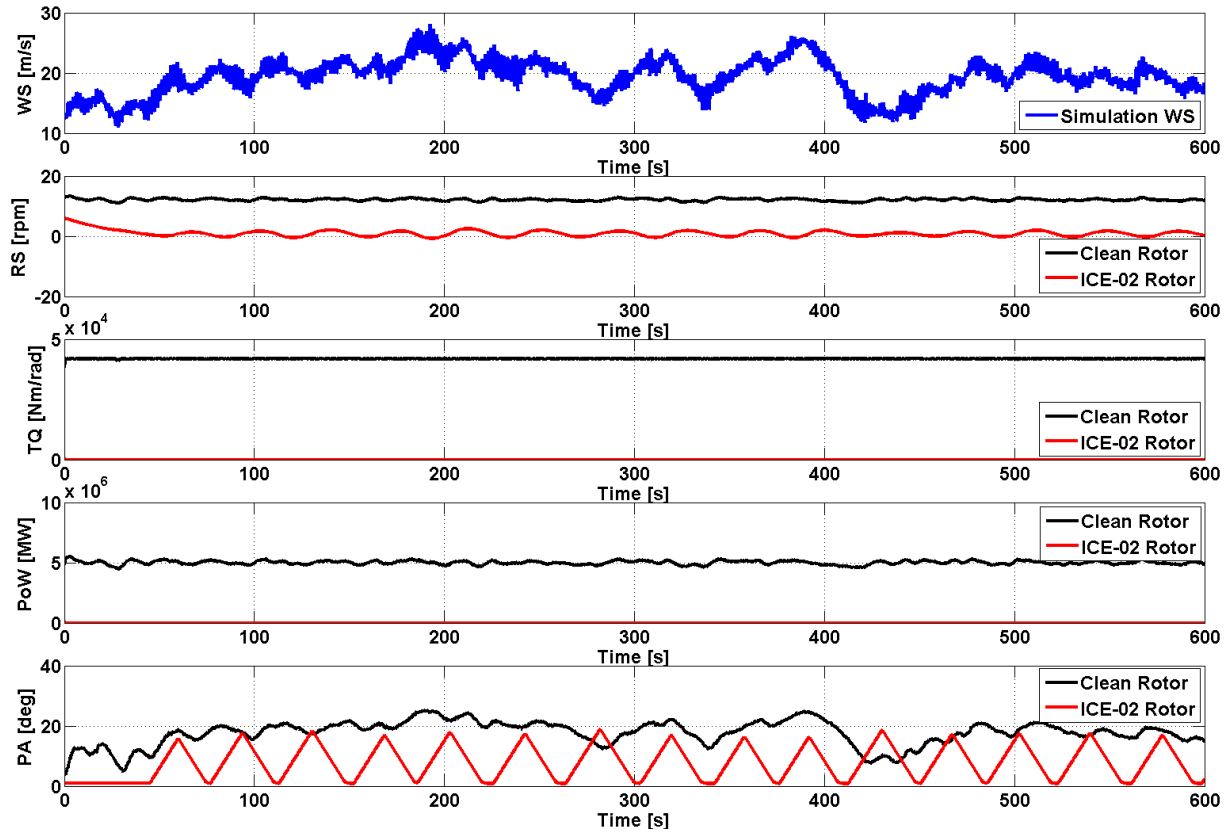

Figure 31: Time Series Simulation for Full-Load Conditions with Clean and Iced (ICE-02) Rotor for the ART 5 MW

3.3 Effects of Support Structure Design Uncertainty

Wind turbine support structures are designed to ensure safe operation of the entire system throughout its lifetime; for this they need to be solid and able to withstand the large forces that occur at the rotor during its lifetime [21, 63]. The support structure is comprised of a tower fixed inside a foundation. The towers are in general designed with large safety factors in mind such that their properties can be guaranteed throughout their lifetime; this implies the use of more material which, in turn, leads to increased overall production costs for the entire system [66]. As previously mentioned, to ensure that through wind turbine operation the structural properties of the tower are also maintained and fatigue loads are reduced, tower damping control loops can be included in the turbine control system for damping at least the first natural frequency of the tower [52], denoted here by NF.

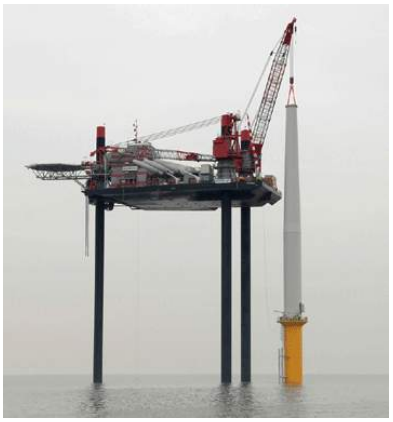

Figure 32: Support Structure Installation

Figure 33: Marine Growth on Offshore Support Structure

In practice, the efficiency of the active tower damping control loops is intimately related to both the structural properties of the tower and the accuracy of the model used throughout the design. Typically, these loops are designed using a nominal tower model i.e. a tower model that is available during the wind turbine design phase. However, some wind turbine manufacturers report that after installation (Figure 32), the modal properties of the wind turbine support structures can differ from the ones designed e.g. the tower natural frequency NF can deviate by as much as 15%. Moreover, during operation, the same modal properties of the tower can change, either due to aging [21, 71, 39] or, in the case of offshore wind turbines due to scour [66, 91], marine sand dunes [30, 29] or even marine growth [98] on the support structure (Figure 33). These, in general, will also have an effect on the tower natural frequency, although less severe.

In Table 3 the control-relevant effects that occur when a 20% lower tower natural frequency NF is present are given; the considered support structure is denoted by **Off-Spec TWr**. Note that for the simulation, an active tower damping controller designed for the support structure with nominal tower frequency, denoted by **NOM TWr** has been used. The presented results have been calculated based on three separate simulations, each with its own mean wind speed but with the same wind realization.

	Below-Rated (BR)		**Around-Rated (ArR)**		**Above-Rated (AbR)**	
	NOM TWr	**Off-Spec TWr**	**NOM TWr**	**Off-Spec TWr**	**NOM TWr**	**Off-Spec TWr**
MAX(Ω_r) [rpm]	10.04	-0.09%	12.91	$+0.10\%$	13.55	$+0.17\%$
STD(Ω_r) [rpm]	1.06	-0.00%	0.52	$+1.54\%$	0.38	$+1.32\%$
Energy [MWh]	5.32	$+0.04\%$	36.69	-0.14%	41.62	$+0.00\%$
Blade DELs [a.u.]	$\text{DEL}_{\text{BR}}^{\text{blade}}$	$+0.60\%$	$\text{DEL}_{\text{ArR}}^{\text{blade}}$	$+0.58\%$	$\text{DEL}_{\text{AbR}}^{\text{blade}}$	$+0.03\%$
Drivetrain DELs [a.u.]	$\text{DEL}_{\text{BR}}^{\text{dt}}$	-0.12%	$\text{DEL}_{\text{ArR}}^{\text{dt}}$	$+44.12\%$	$\text{DEL}_{\text{AbR}}^{\text{dt}}$	-37.24%
Tower DELs [a.u.]	$\text{DEL}_{\text{BR}}^{\text{tow}}$	$+50.92\%$	$\text{DEL}_{\text{ArR}}^{\text{tow}}$	$+107.63\%$	$\text{DEL}_{\text{AbR}}^{\text{tow}}$	$+97.63\%$

Table 3: Comparison of Simulation Results for the ART 5 MW with Nominal and Off-Spec Support Structure (-20% in NF)

As can be observed, if the support structure dynamics differ such that the natural frequency NF drops to such extents, although the performance of the PR/RSC control loop remains unaffected, the performance of the active TowD control loop is severely limited, as hinted by the great increase of tower damage equivalent loads (DELs); notice that the active DriD control loop is also potentially affected at around-rated wind speeds. Similarly, through Table 4 the control-relevant effects of a 20% higher tower natural frequency NF can be investigated; as opposed to the previous situation, in this case the TowD control loop appears not to be performing well only in partial-load. Nonetheless, the DELs in the drivetrain are still higher in the **Off-Spec TWr** case than for a nominal support structure **NOM TWr** for around-rated mean wind speed simulations.

	Below-Rated		Around-Rated		Above-Rated	
	NOM TWr	**Off-Spec TWr**	**NOM TWr**	**Off-Spec TWr**	**NOM TWr**	**Off-Spec TWr**
MAX(Ω_r) [rpm]	10.04	-0.13%	12.91	-0.07%	13.55	$+0.05\%$
STD(Ω_r) [rpm]	1.06	-0.14%	0.52	-0.45%	0.38	-0.73%
Energy [MWh]	5.32	-0.23%	36.69	$+0.04\%$	41.62	$+0.00\%$
Blade DELs [a.u.]	$\text{DEL}_{\text{BR}}^{\text{blade}}$	$+0.52\%$	$\text{DEL}_{\text{ArR}}^{\text{blade}}$	-0.28%	$\text{DEL}_{\text{AbR}}^{\text{blade}}$	-0.03%
Drivetrain DELs [a.u.]	$\text{DEL}_{\text{BR}}^{\text{dt}}$	-0.55%	$\text{DEL}_{\text{ArR}}^{\text{dt}}$	$+43.74\%$	$\text{DEL}_{\text{AbR}}^{\text{dt}}$	-37.48%
Tower DELs [a.u.]	$\text{DEL}_{\text{BR}}^{\text{tow}}$	$+37.95\%$	$\text{DEL}_{\text{ArR}}^{\text{tow}}$	-33.95%	$\text{DEL}_{\text{AbR}}^{\text{tow}}$	-32.55%

Table 4: Comparison of Simulation Results for the ART 5 MW with Nominal and Off-Spec Support Structure ($+20\%$ in NF)

In Figure 34 and Figure 35 the power spectra of the tower bottom moments corresponding to the presented simulation are shown. As can be seen, in the case of off-spec support structures (**Off-Spec TWr**), the nominally-designed TowD control loop is affected. Whereas typically the peaks in the power spectra of the tower bottom moments around the tower natural frequency NF would be damped if the TowD control loop would be performing well, for the cases when the support structure behaviour is away from the designed one (**NOM TWr**), this is no longer the case. Furthermore, by inspecting Figure 36 and Figure 37 it can noticed that indeed for the case of a lower tower natural frequency, the oscillations of the tower top position are larger. This holds true for both partial-load conditions and full-load conditions, but is more pronounced in the latter case and explains well both the results presented in Table 3 and the tower bottom moments spectra in Figure 34 and Figure 35. At last, in Figure 38 and Figure 39, the effects of a high tower natural tower frequency can be observed. For partial-load conditions the movement of the off-spec tower is reduced in amplitude, yet more oscillatory which will also cause higher DELs. For full-load operation the tower top oscillates with less ample movements; this is in agreement with the conclusions drawn based on Table 4. Based on the presented analysis, it can be concluded that a method of dealing with variations in the support structure dynamics would be necessary to improve the performance of the active tower damping control loop. Similarly, the drivetrain damping control loop design would also need to be re-investigated in view of around-rated mean wind speed turbine operation, yet this falls outside the scope of this thesis.

3.4 Conclusions

The analysis performed in this chapter regarding the main design uncertainty factors in the wind turbine aerodynamic subsystem and support structure has been related to up-to-date reported works from the technical literature. Ice accretion on wind turbine blades has been shown to be a factor of concern and worth taking into account for control design. The conclusions, however, have been different depending on the ice profile type: whereas one of the ice geometries introduces only mild problems for a nominally-designed power regulation and rotor speed control loop, the other one limits turbine power performance severely and also affects auxiliary control schemes such as the start-up control algorithm. A discussion regarding the effects of changed modal properties of the wind turbine support structure has also been given, in the latter part of the chapter. As concluded, the active tower damping control loop will not deliver satisfactory performance in the case of variations in the considered control-relevant tower properties, to this extent the first fore-aft tower natural frequency NF. Nonetheless, if appropriately accounted for during the design phase, these effects can potentially be reduced. This is the focus of the next chapter where one particular class of advanced control design tools is used for the improved design of the active tower damping control loop.

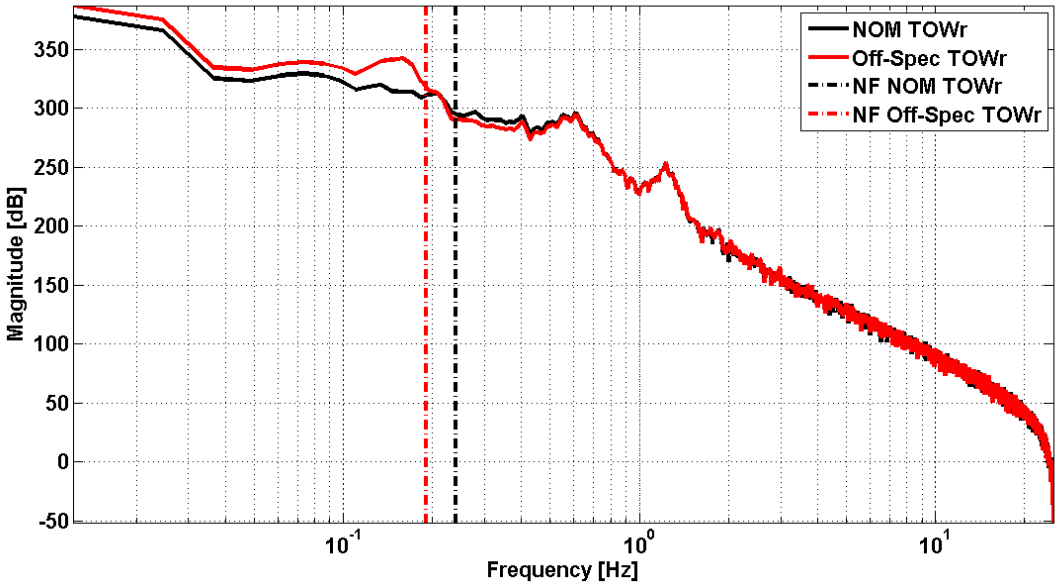

Figure 34: Spectra of Tower Bottom Moment based on Full-Load Simulation of the ART 5 MW with Nominal and Off-Spec ($+20\%$ in NF) Support Structure

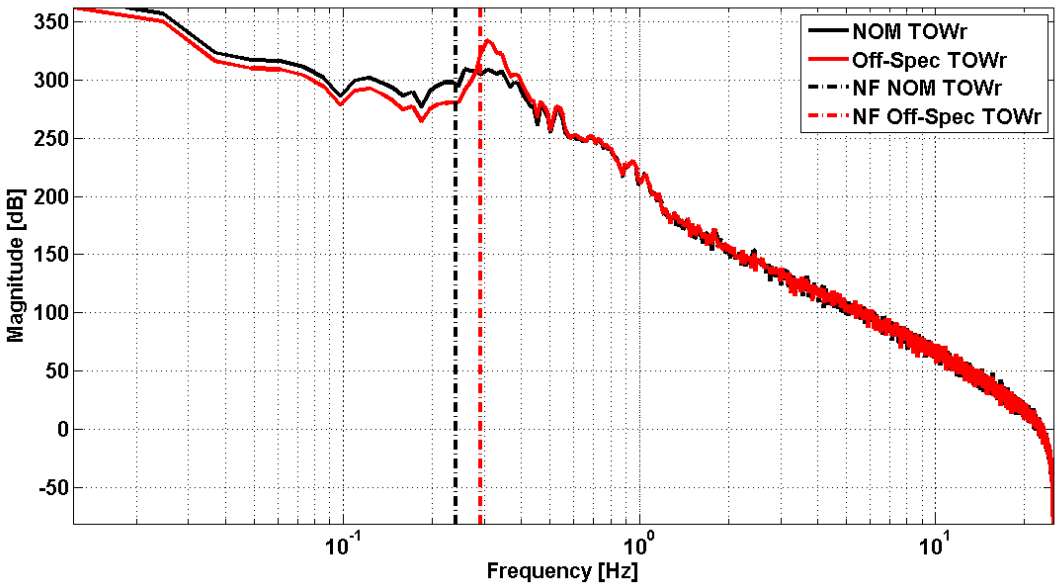

Figure 35: Spectra of Tower Bottom Moment based on Partial-Load Simulation of the ART 5 MW with Nominal and Off-Spec ($+20\%$ in NF) Support Structure

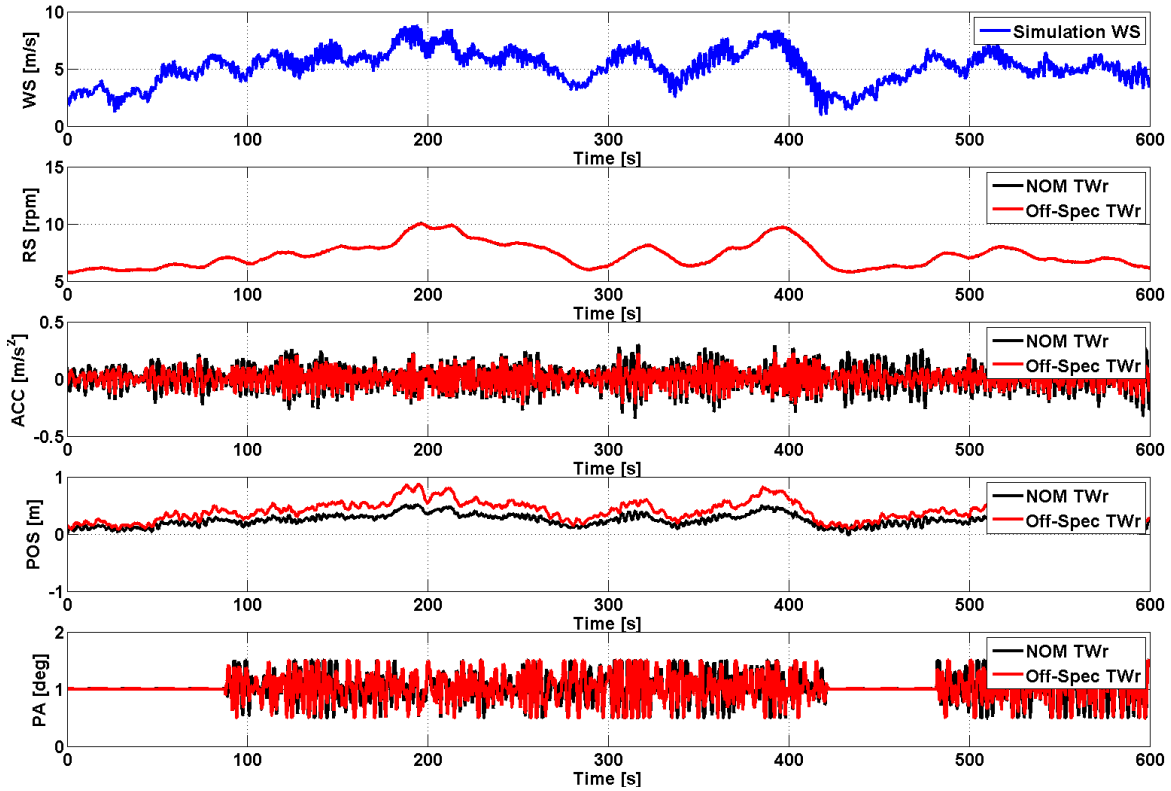

Figure 36: Time Series Simulation for Partial-Load Conditions with Nominal and Off-Spec (-20% in NF) Tower for the ART 5 MW

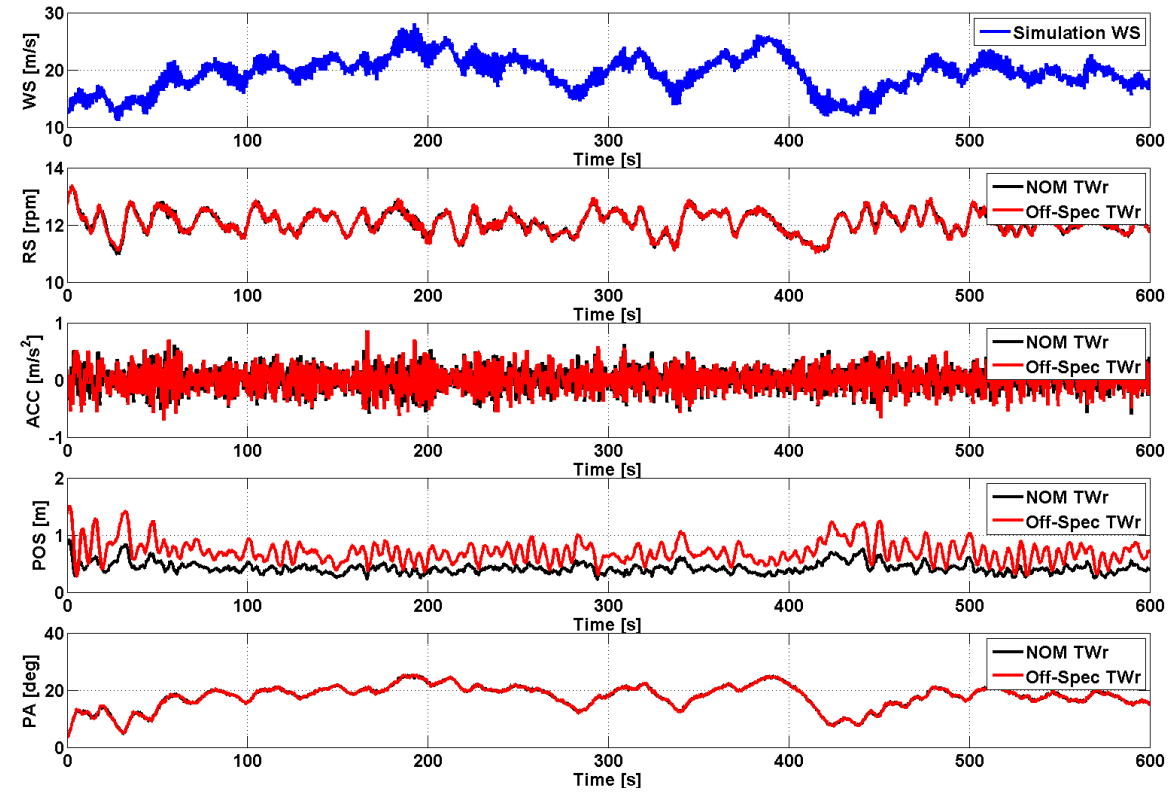

Figure 37: Time Series Simulation for Full-Load Conditions with Nominal and Off-Spec (-20% in NF) Tower for the ART 5 MW

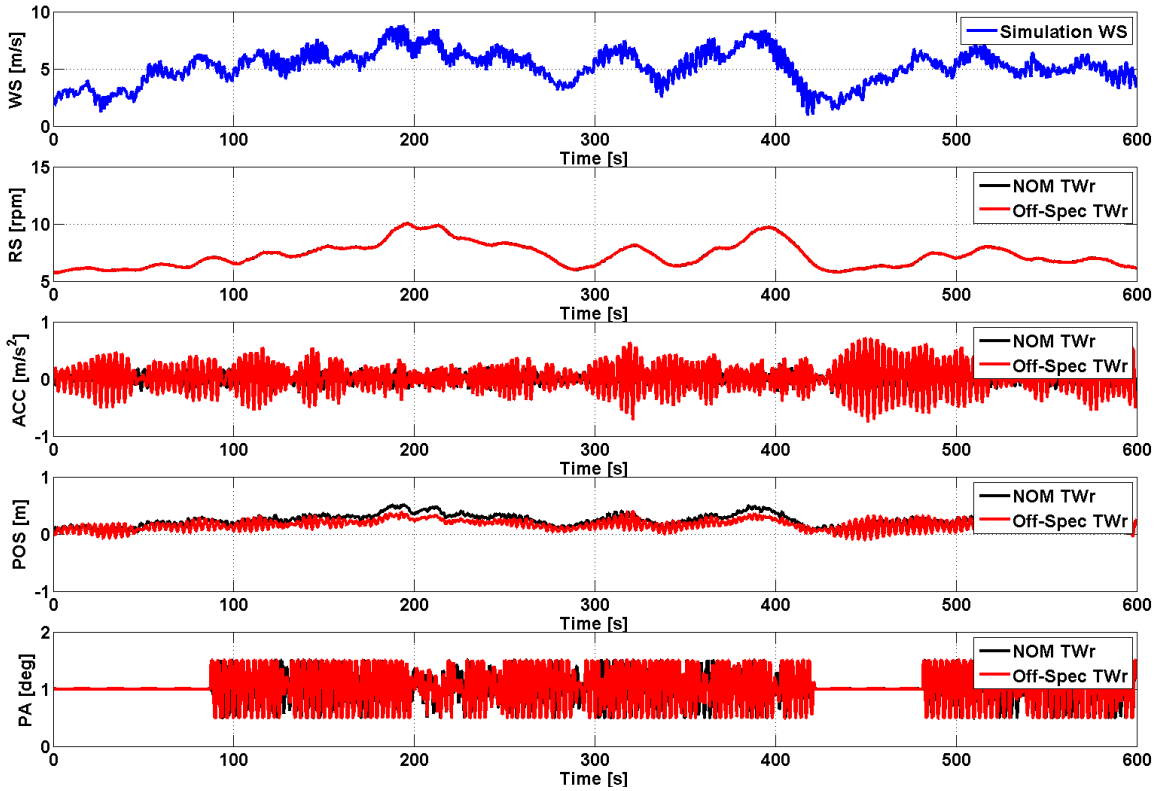

Figure 38: Time Series Simulation for Partial-Load Conditions with Nominal and Off-Spec ($+20\%$ in NF) Tower for the ART 5 MW

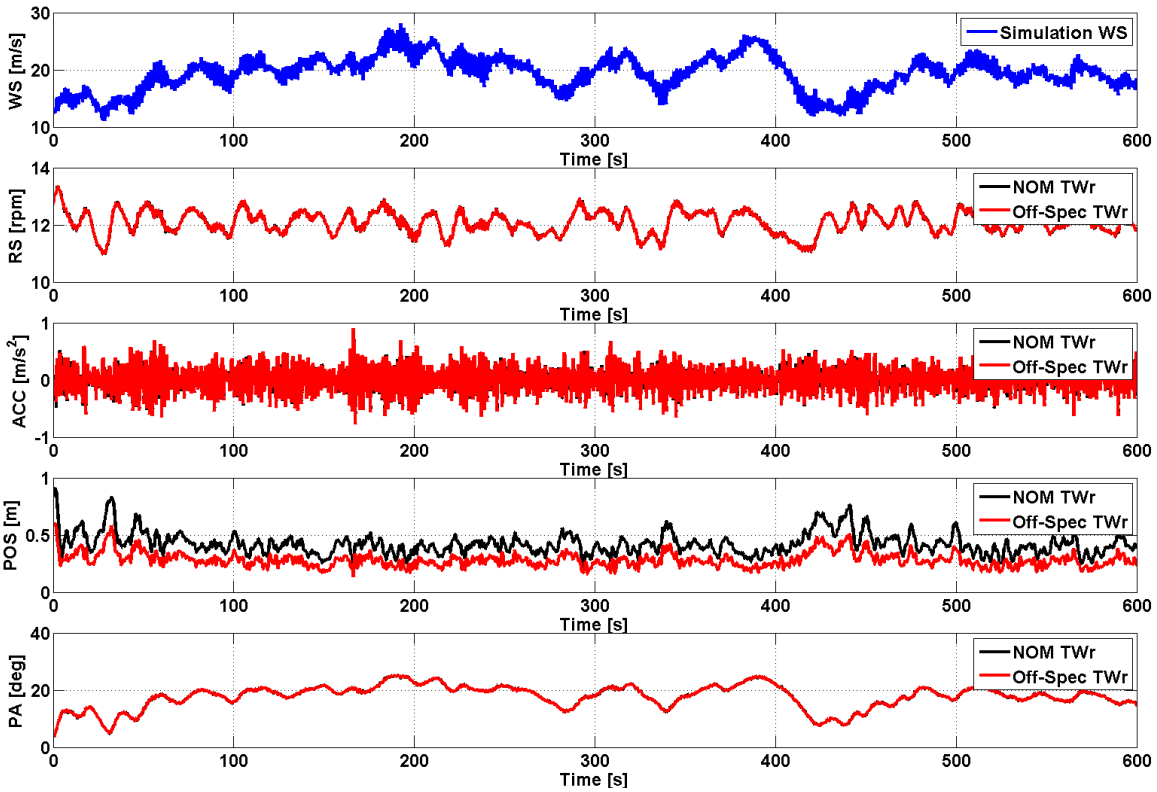

Figure 39: Time Series Simulation for Full-Load Conditions with Nominal and Off-Spec ($+20\%$ in NF) Tower for the ART 5 MW

4

Linear Parameter-Varying Active Tower Damping Control

This chapter presents the approach taken towards addressing the need for improved control design in the light of the mentioned uncertainty factors as well as the relation between their effects on control performance and the goals formulated for the project. Consequently, an improved active tower damping control design is developed in this chapter that can cope with changes in the parameters of the considered support structure model. The goals of the tower damping control loop are first revisited from the perspective of damage equivalent load mitigation. The associated control problem is then formulated and a design approach is developed. The method covered is successfully proven to work in a case study where the turbine is simulated with different off-spec tower natural frequencies. A series of conclusions regarding the presented material is finally drawn.

4.1 Motivation and Objectives

The goal of the active fore-aft tower damping control loop is to allow for support structure fatigue load reduction by means of collective pitch control. By modifying the pitch angle of the blades in response to the motions of the tower top, the fatigue loads can be reduced [52]. The tower bottom moment, considered to this extent to be the most important indicator of the existing mechanical loads in the support structure [21], is linearly related to the tower top displacement in the case of the considered simplified tower model. In practice, it is of special importance to have an estimate of how the mechanical loads in the tower relate to the support structure lifetime. This is generally evaluated starting from the time series of the tower bottom moment evolution and using this data within DEL calculation algorithms such as e.g. the rainflow-counting (RFC) algorithm to arrive at an estimate of the equivalent fatigue load for the entire lifetime of the wind turbine [21]. From a controls viewpoint, the problem of DEL load mitigation is not only challenging due to the fact that the calculation of damage equivalent loads can be done in many different ways, all yielding their separate results only correlated up to some extent [69] but also due to the fact that it is difficult, if not impossible, to formulate control objectives in terms of some desired DEL behaviour. The DEL reduction problem can be indirectly addressed through e.g. $\mathcal{H}_\infty$ or $\mathcal{H}_2$ approaches to active tower damping control loop design [82, 34, 38, 47, 35, 52]. Within this chapter, it has been chosen to use an $\mathcal{H}_2$ cost function minimization objective for the purpose of achieving DEL reduction [52]. However, an $\mathcal{H}_\infty$ approach could equally be used. The crucial aspect, however, is to allow the controller to adapt to changes in the support structure dynamics, as explained next.

4.2 Problem Formulation and Control Design Framework

The tower damping design control problem has been formulated in **Chapter 2** as a linear quadratic Gaussian (LQG) design problem for the linear time-invariant (LTI) system (2.35) defined by (2.36): the control signal $\delta\theta(t)$ is calculated at every time instant by using LQR-designed static state-feedback on the estimates of the tower top position and velocity delivered by the *Tower Fore-Aft Dynamics Observer*. As discussed in **Chapter 3**, the performance of the tower damping control loop deteriorates when the underlying LTI model:

$$\begin{bmatrix}\delta\dot{x}_{FA}(t)\\ \delta\ddot{x}_{FA}(t)\end{bmatrix} = A_{TowD}(\bar{p}(t),\omega_n^{tow})\begin{bmatrix}\delta x_{FA}(t)\\ \delta\dot{x}_{FA}(t)\end{bmatrix} + B_{u,TowD}(\bar{p}(t),\omega_n^{tow})\delta\theta(t) + B_{w,TowD}(\bar{p}(t),\omega_n^{tow})\delta v_{rot}(t)$$

$$\delta\ddot{x}_{FA}(t) = C_{TowD}(\bar{p}(t),\omega_n^{tow})\begin{bmatrix}\delta x_{FA}(t)\\ \delta\dot{x}_{FA}(t)\end{bmatrix} + D_{u,TowD}(\bar{p}(t),\omega_n^{tow})\delta\theta(t) + D_{w,TowD}(\bar{p}(t),\omega_n^{tow})\delta v_{rot}(t) \quad (4.1)$$

is no longer representative due to changes in the parameter $\omega_n^{tow} \triangleq \frac{s_t}{m_t}$, directly related to the first fore-aft tower natural frequency NF the support structure dynamics through $\sqrt{\omega_n^{tow}}$. The model in (4.1) is parametrized both by the equilibrium operating point $\bar{p}(t)$ and the parameter ω_n^{tow} that relates to fore-aft tower natural frequency. In this thesis, a dynamic output-feedback LPV gain-scheduled controller is designed such that the controller self-adapts its parameters to the changes in ω_n^{tow}. However, note that the equilibrium operating point $\bar{p}(t)$ will be considered fixed or very slowly changing throughout the design. The problem is solved in a dynamic output-feedback framework, as the state observer does not operate well under the considered changes in ω_n^{tow}. As further theoretical background for this reasoning, the reader is referred to [40].

In Figure 40 the magnitude Bode plot of the parametrized family of support structure dynamical models (4.1) is given for the range of tower natural frequencies considered throughout the design $\sqrt{\omega_n^{tow}} \in \left[0.8\sqrt{\omega_{n,nom}^{tow}}, 1.2\sqrt{\omega_{n,nom}^{tow}}\right]$. As can be observed, both the low-frequency side - close to the direct current (DC) gain - and the peak amplitude owed to the complex conjugate pole of (4.1) for a fixed ω_n^{tow} vary as the value of ω_n^{tow} is changed within the considered interval.

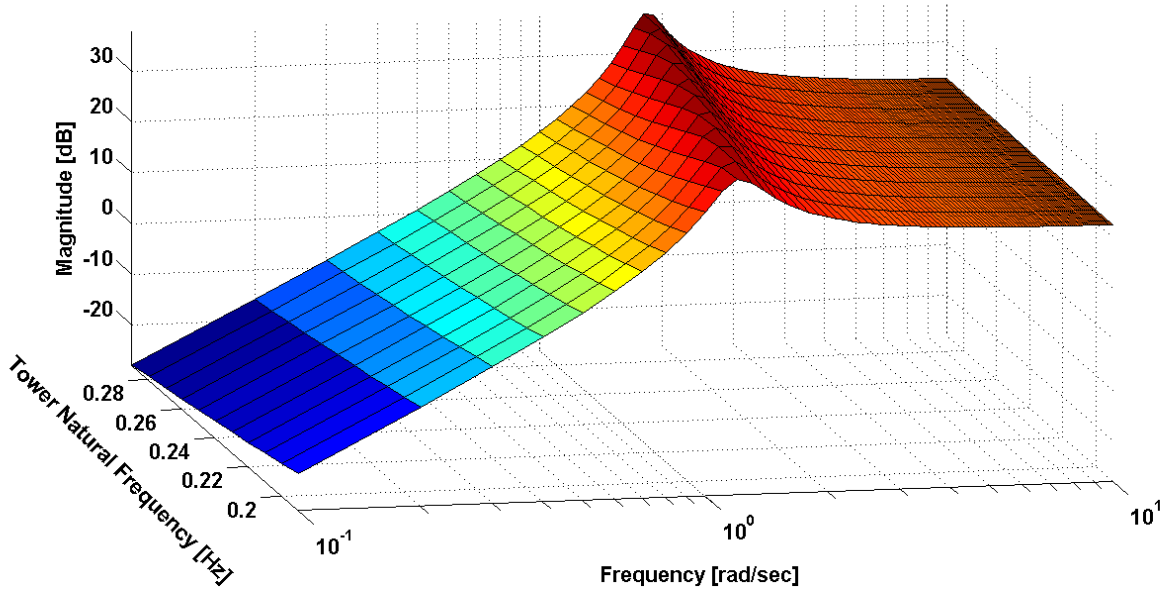

Figure 40: Magnitude Bode Plot of the $\delta\theta(t) \rightarrow \delta\ddot{x}_{FA}(t)$ Transfer from (4.1) for the Considered Range of Tower Natural Frequencies

Note that the proposed model for control design (4.1) is affine in the parameter ω_n^{tow}, which can be observed by simple inspection of (2.36) for the given definition of ω_n^{tow}. This allows the design of an LPV controller scheduled on ω_n^{tow} using tools from convex optimization theory (see **Appendix A** for details). Carrying the design in discrete-time allows for direct implementation without any need for online discretization as well as for the prevention of possible loss of achieved performance due to controller post-design discretization [87, 88]. The design algorithm chosen is the *generalized $\mathcal{H}_2$ dynamic output-feedback synthesis for discrete-time systems*, described extensively in **Appendix A**.

The final controller has the form:

$$\begin{aligned} x_K(k+1) &= A_K(\omega_n^{tow})x_K(k) + B_K(\omega_n^{tow})\delta\ddot{x}_{FA}(k) \\ \delta\theta(k) &= C_K(\omega_n^{tow})x_K(k) \end{aligned} \tag{4.2}$$

with all its state matrices depending on ω_n^{tow}. The controller is of the same order as the generalized plant and formulated by relating the previous LQR design problem with the current $\mathcal{H}_2$ design problem [37]. This is shown in Figure 42 for the sake of clarity. As can be seen in Figure 42, explicit account has been taken of the introduced tower damping control filters that prevent control action to occur at frequencies introduced by e.g. the rotational sampling effect [52].

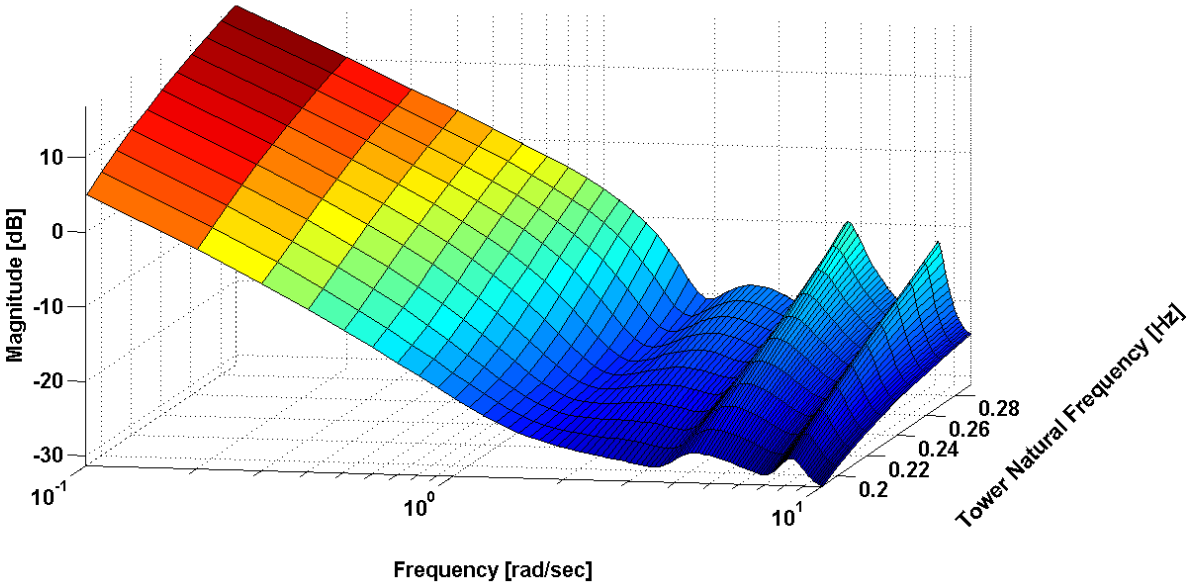

Figure 41: Magnitude Bode Plot of the $\delta\ddot{x}_{FA}(k) \rightarrow \delta\theta(k)$ Transfer of the LPV Tower Damping Controller for the Considered Range of Tower Natural Frequencies

The designed controller will in practice be of the same order as the formulated generalized plant. As can be seen in the Bode magnitude plot of Figure 41 given as a function of the parameter ω_n^{tow}, the controller can become of rather high-order due to the size of the generalized plant. It is interesting to observe that due to the formulated generalized $\mathcal{H}_2$ objective function, the controller will attempt to reduce the magnitude of the closed-loop system frequency response at all complex frequencies. Observe, for example, how the closed-loop system low-frequency behaviour will eventually be changed from that of the the open-loop system (4.1) behaviour by means of the LPV controller. Similarly, notice how several peaks do appear in Figure 41 due to the fact that for the minimization of generalized $\mathcal{H}_2$ objective function the controller will try to counteract the effect of the tower damping control filters.

In the next section, the proposed LPV design approach is demonstrated on a case study with the full ART 5 MW wind turbine model, whose tower dynamics is represented as (4.1), varying in terms of ω_n^{tow}.

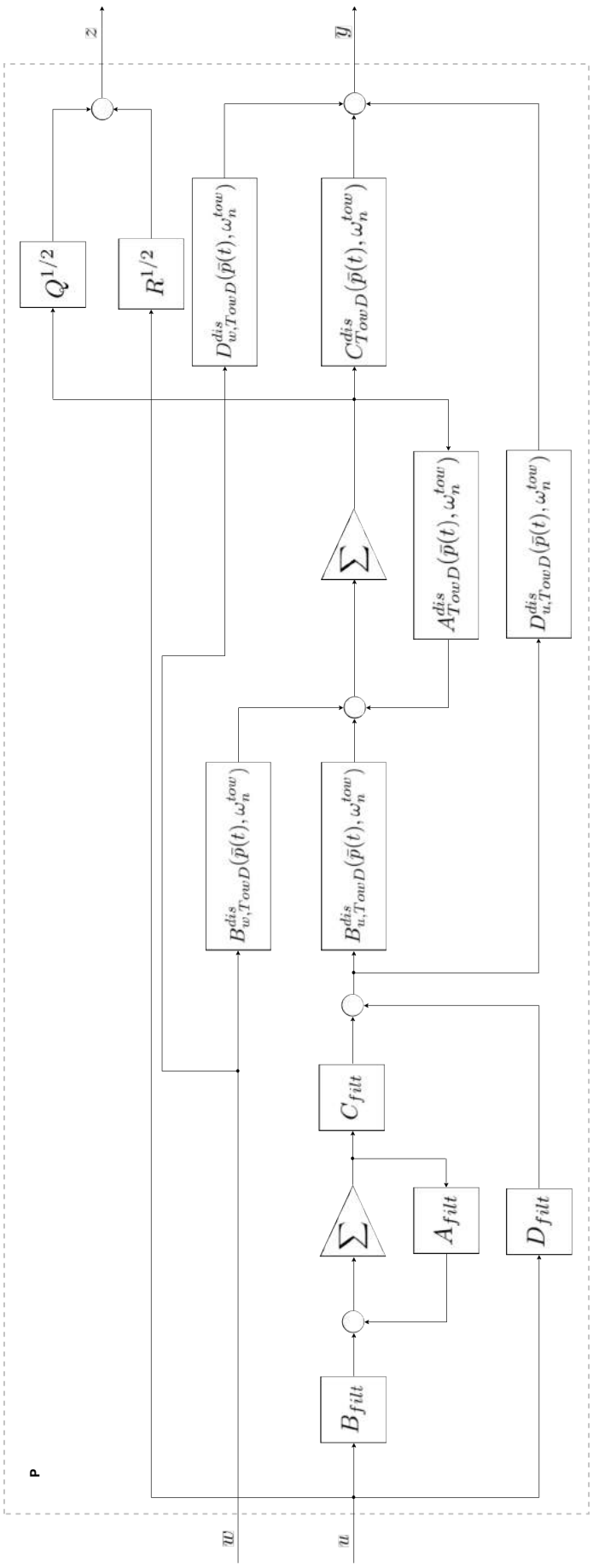

Figure 42: Generalized Plant for LPV Active Tower Damping Control

4.3 Evaluation of the Obtained Results

The LPV tower damping controller designed in the previous section will now be used for analyzing the achieved results in situations where the modal support structure characteristics are off-spec, following similar lines to the investigation presented in **Chapter 3**. The reported results are based on the following simulation setup:

- **Simulation time**: 650 seconds (data from the first 50 seconds unused);
- **Simulated wind**: one realization (same as previously); three wind speeds, as follows: 5.25 [m/s] - below-rated conditions, 12.5 [m/s] - around-rated conditions, 20 [m/s] - above-rated conditions;
- **Simulation model**: full ART 5 MW model (see **Appendix B** for details) with different tower natural frequencies NF given by $\sqrt{\omega_n^{tow}} \in \left[0.8\sqrt{\omega_{n,nom}^{tow}}, 1.2\sqrt{\omega_{n,nom}^{tow}}\right]$;
- **Active control loops**: PR/RSC (nominal design), DriD (nominal design) and TowD (two designs, one fixed and based on the nominal tower natural frequency - denoted by **LTI** and one based on the defined parameter ω_n^{tow} associated variation range, scheduled on the value that ω_n^{tow} takes during a particular simulation - denoted by **LPV**).

The obtained results for the worst-case variations of ω_n^{tow} with the **LPV** active tower damping controller are summarized in Table 5 and Table 6 as a comparison with the results that had been obtained in **Chapter 3** with the **LTI** tower damping controller. Note the values reported for the **LTI** controller are already scaled as defined by Table 3 and Table 4, respectively, so as to allow the comparison to be made with respect to them.

As can be observed in Table 5, adapting the **LPV** controller parameters to the change in the tower natural frequency NF allows for the tower damping control loop to perform better than in the **LTI** controller case. Note how for a 20% lower NF, the **LPV** controller is able of reducing the associated tower DELs by 3% for below-rated conditions and even up to approximately 8% for above-rated conditions, when compared to the **LTI** controller. It is especially the latter results that brings forward the extent of the improvement as this could allow wind turbine manufacturers to reduce the safety factor that would need to cover for the worst-case scenario by the same considerable amount of 8%. It is also worth mentioning that this improvement comes at no additional cost, given that the remaining assessed factors, reported in Table 5, remain approximately the same when comparing the performance of the **LPV** tower damping controller with that of the **LTI** one. For the computation of the presented data one wind realization has been used - the real-life performance will be only slightly different - if several more wind realizations are used for simulation and the associated obtained results are averaged, the confidence in the reported results can be increased [21, 63]. Finally, the time series that correspond to the partial-load and full-load simulations are summarized by Figure 47 and Figure 48.

	Below-Rated (BR)		**Around-Rated (ArR)**		**Above-Rated (AbR)**	
	LTI	**LPV**	**LTI**	**LPV**	**LTI**	**LPV**
MAX(Ω_r) [rpm]	10.03	$+0.09\%$	12.89	$+0.11\%$	13.57	-0.24%
STD(Ω_r) [rpm]	1.06	$+0.12\%$	0.52	$+0.57\%$	0.38	$+3.26\%$
Energy [MWh]	5.32	$+0.13\%$	36.63	-0.01%	41.62	-0.05%
Blade DELs [a.u.]	$1.006 \cdot \text{DEL}_{\text{BR}}^{\text{blade}}$	$+0.06\%$	$1.005 \cdot \text{DEL}_{\text{ArR}}^{\text{blade}}$	-0.09%	$1.000 \cdot \text{DEL}_{\text{AbR}}^{\text{blade}}$	$+0.06\%$
Drivetrain DELs [a.u.]	$0.998 \cdot \text{DEL}_{\text{BR}}^{\text{dt}}$	$+0.22\%$	$1.441 \cdot \text{DEL}_{\text{ArR}}^{\text{dt}}$	$+0.92\%$	$0.627 \cdot \text{DEL}_{\text{AbR}}^{\text{dt}}$	-0.01%
Tower DELs [a.u.]	$1.509 \cdot \text{DEL}_{\text{BR}}^{\text{tow}}$	-2.82%	$2.076 \cdot \text{DEL}_{\text{ArR}}^{\text{tow}}$	-1.97%	$1.976 \cdot \text{DEL}_{\text{AbR}}^{\text{tow}}$	-8.27%

Table 5: Comparison of LTI TowD Controller and LPV TowD Controller Simulation Results for the ART 5 MW with Off-Spec Support Structure (-20% in NF)

The presented results of Table 5 are in agreement with the spectra of the tower bottom moments for e.g. for the above-rated simulations, shown in Figure 43. Observe how, in this specific example, the LPV active tower damping controller (**LPV TowD**) performs better than the nominal LTI tower damping controller (**LTI TowD**) for the case when the tower natural frequency is 20% lower (**Off-Spec TOWr**) than its nominal specification (**NOM TOWr**): the appearing

peak in the power spectra of the tower bottom moment owed to the change in the tower natural frequency is reduced by **LPV TowD** compared to **LTI TowD** which explains the improvement shown in Table 5. Furthermore, in the case when the tower natural frequency is increased by 20% above its nominal designed value, the **LPV** tower damping controller does again perform better in terms of tower DELs than the nominal **LTI** controller, especially for below-rated conditions. Note how, based on Table 5, this improvement is again by up to approximately 9%. The power spectra of the tower bottom moments for this special situation are shown in Figure 44. The difference between the spectra of the moments with the nominal LTI controller (**LTI TowD**) and the LPV controller (**LPV TowD**) is far less pronounced in this case. At last, the time series that correspond to the partial-load and full-load simulations are summarized by Figure 49 and Figure 50.

	Below-Rated (BR)		Around-Rated (ArR)		Above-Rated (AbR)	
	LTI	LPV	LTI	LPV	LTI	LPV
MAX(Ω_r) [rpm]	10.02	+0.16%	12.90	+0.06%	13.55	−0.04%
STD(Ω_r) [rpm]	1.05	+0.08%	0.51	−0.12%	0.37	+0.62%
Energy [MWh]	5.30	+0.59%	36.70	−0.02%	41.62	+0.00%
Blade DELs [a.u.]	$1.005 \cdot \text{DEL}_{\text{BR}}^{\text{blade}}$	−0.18%	$0.997 \cdot \text{DEL}_{\text{ArR}}^{\text{blade}}$	+0.26%	$0.999\text{DEL}_{\text{AbR}}^{\text{blade}}$	+0.05%
Drivetrain DELs [a.u.]	$0.994 \cdot \text{DEL}_{\text{BR}}^{\text{dt}}$	+0.55%	$1.437 \cdot \text{DEL}_{\text{ArR}}^{\text{dt}}$	+0.14%	$0.625 \cdot \text{DEL}_{\text{AbR}}^{\text{dt}}$	+0.85%
Tower DELs [a.u.]	$1.379 \cdot \text{DEL}_{\text{BR}}^{\text{tow}}$	−8.62%	$0.660 \cdot \text{DEL}_{\text{ArR}}^{\text{tow}}$	−0.11%	$0.674 \cdot \text{DEL}_{\text{AbR}}^{\text{tow}}$	+0.61%

Table 6: Comparison of LTI TowD Controller and LPV TowD Controller Simulation Results for the ART 5 MW with Off-Spec Support Structure (+20% in NF)

In Figure 45 and Figure 46 the performance with **LPV** tower damping controller (**LPV TowD**) in terms of achieved DELs for different simulation cases, both partial-load and full-load, is shown in comparison to that obtained with the nominal **LTI** controller (**Nominal LTI TowD**) and to that achieved when the tower damping control loop is disabled (**TowD OFF**). Additionally, the performance obtained with a redesigned LTI tower damping controller based on the changed tower natural frequency is also shown (**Redesigned LTI TowD**). As can be seen, **LPV TowD** scheduled on the value of the parameter ω_n^{tow} does almost always perform better than **Nominal LTI TowD**, designed for the nominal tower natural frequency. The DEL performance with **LPV TowD** is, however, outperformed by **Redesigned LTI TowD** - the magnitude of the additional load reduction, though, depends on the considered values for the tower frequency. It can be observed that the worst-case loads i.e. loads occurring for tower natural frequencies lower than the design are further reduced by **Redesigned LTI TowD**. Notice, however, that **Nominal LTI TowD** can increase the DELs in some situations e.g. for below-rated conditions when the natural tower frequency happens to be higher than the designed one.

4.4 Conclusions

In this chapter an LPV approach towards improved active tower damping control design has been proposed. This has been motivated by the analysis presented **Chapter 3**. The goals of the active tower damping control loop have been revisited and remarks regarding the formulation of the control objective of the tower damping control loop have been made with respect to the possibility of increased mitigation of fatigue loads. Subsequently, a tower damping control problem that allows the controller to change its parameters based on the changes in the modal properties of the turbine support structure has been presented. The given formulation has allowed for an appropriate comparison with the approach of **Chapter 2**. The design results have been shown and an evaluation of the obtained results has been given. As indicated, the DEL performance of LPV tower damping control loop, scheduled on ω_n^{tow} allows for a reduction of fatigue loads of approximately 8% compared to the situation revealed in the analysis of **Chapter 3**. Nonetheless, as has been shown, the complete redesign of some nominal controller is more appropriate for some load cases, although not practical due to additional design work, load calculations and the wind turbine certification practices. Based on confidential information from wind turbine manufacturers, the reduction of fatigue loads in the turbine support structure is proportional to the reduction of combined manufacturing and maintenance costs. This makes the proposed solution very attractive for the industry.

The following chapter brings into discussion how the presented work can be further extended towards allowing for improved performance.

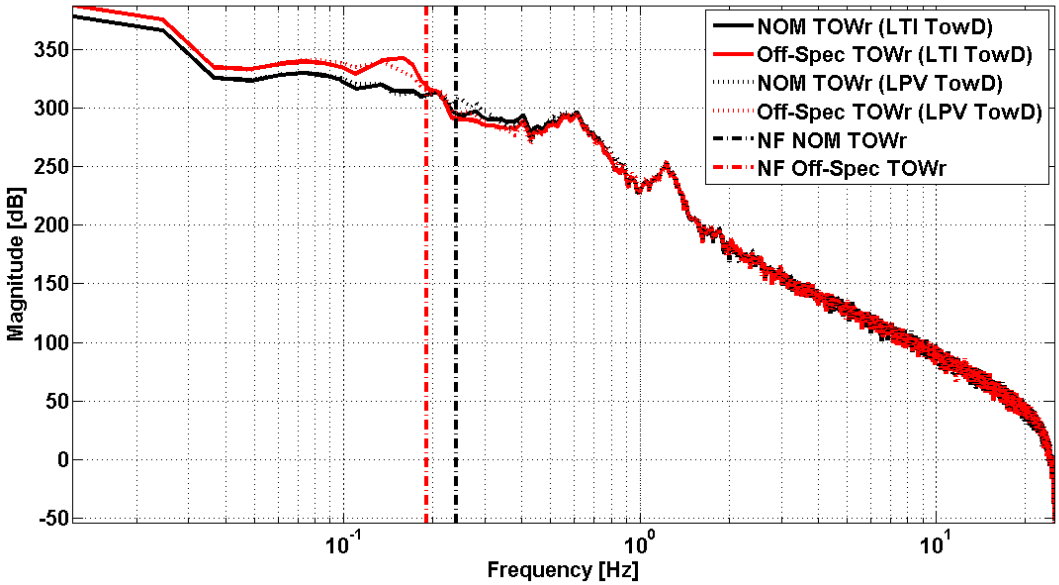

Figure 43: Comparative Spectra of Tower Bottom Moment based on Full-Load Simulation of the ART 5 MW with Nominal and Off-Spec (-20% in NF) Support Structure

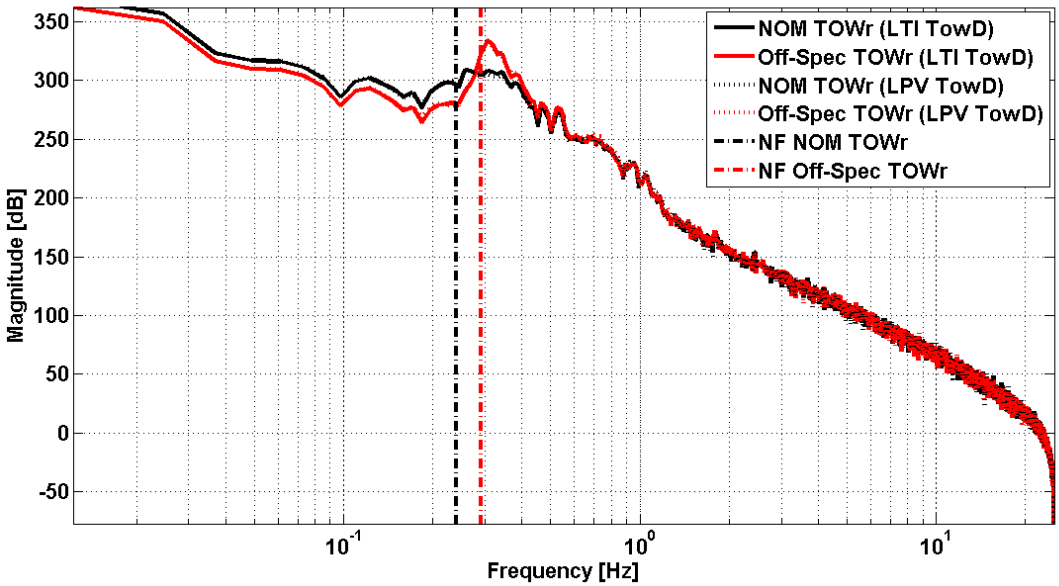

Figure 44: Comparative Spectra of Tower Bottom Moment based on Partial-Load Simulation of the ART 5 MW with Nominal and Off-Spec ($+20$% in NF) Support Structure

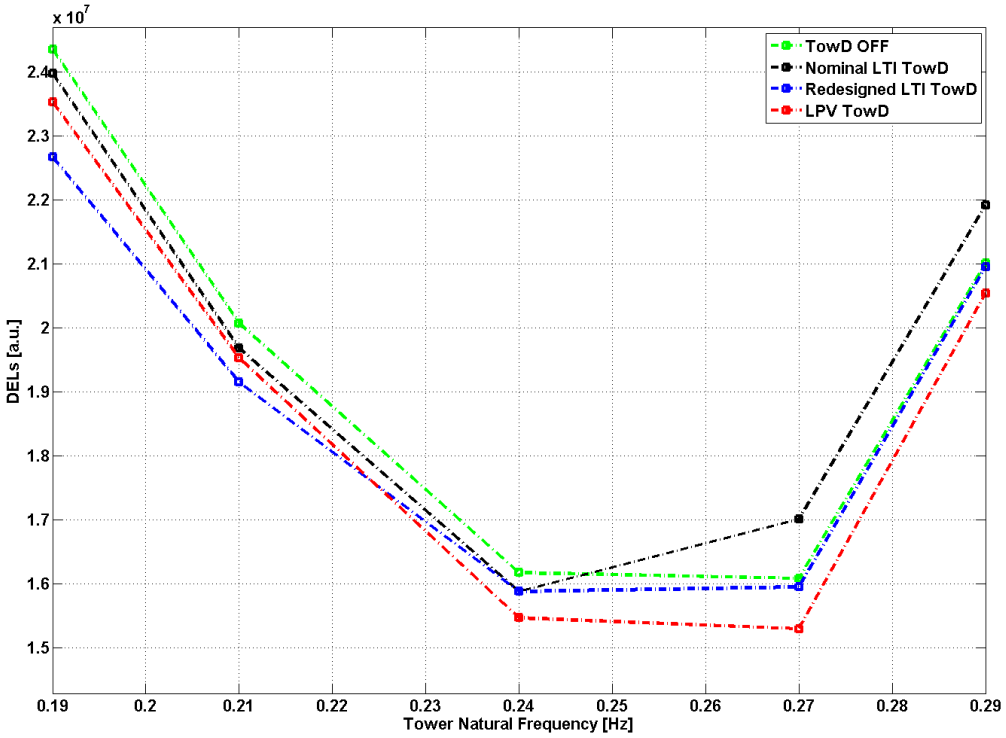

Figure 45: DEL Comparison for the ART 5 MW for Below-Rated Simulations with Different Active Tower Damping Controllers

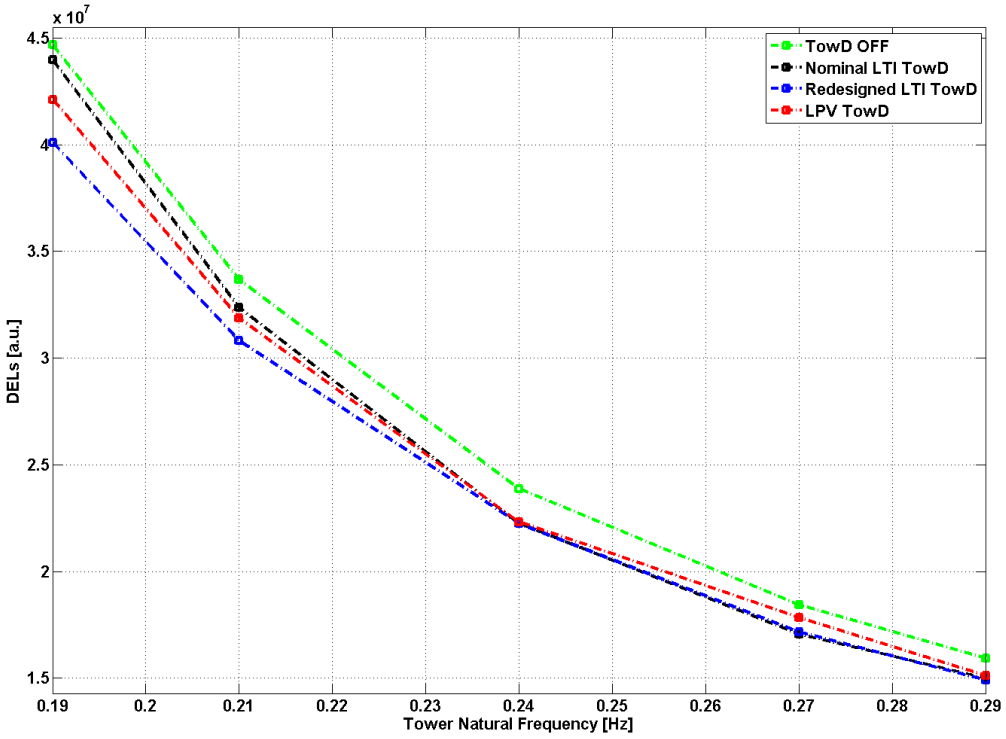

Figure 46: DEL Comparison for the ART 5 MW for Above-Rated Simulations with Different Active Tower Damping Controllers

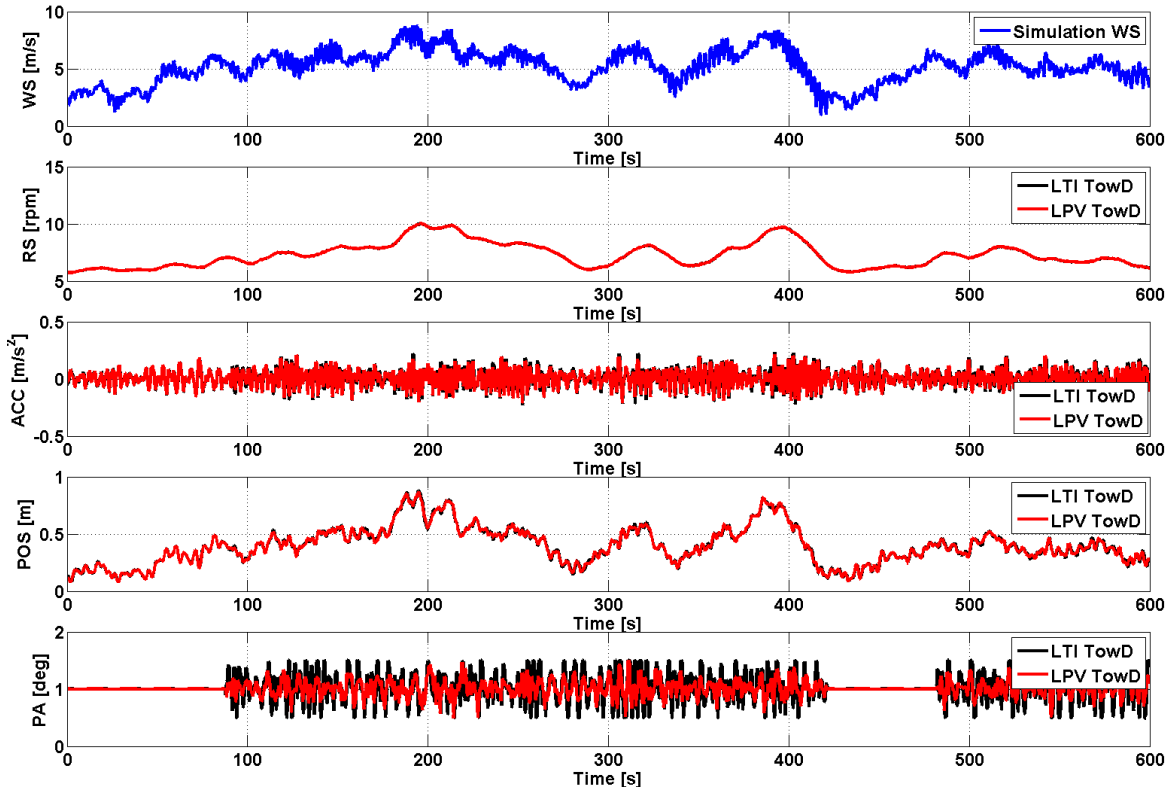

Figure 47: Time Series Comparison for Partial-Load Conditions with Nominal and Off-Spec (-20% in NF) Tower for the ART 5 MW

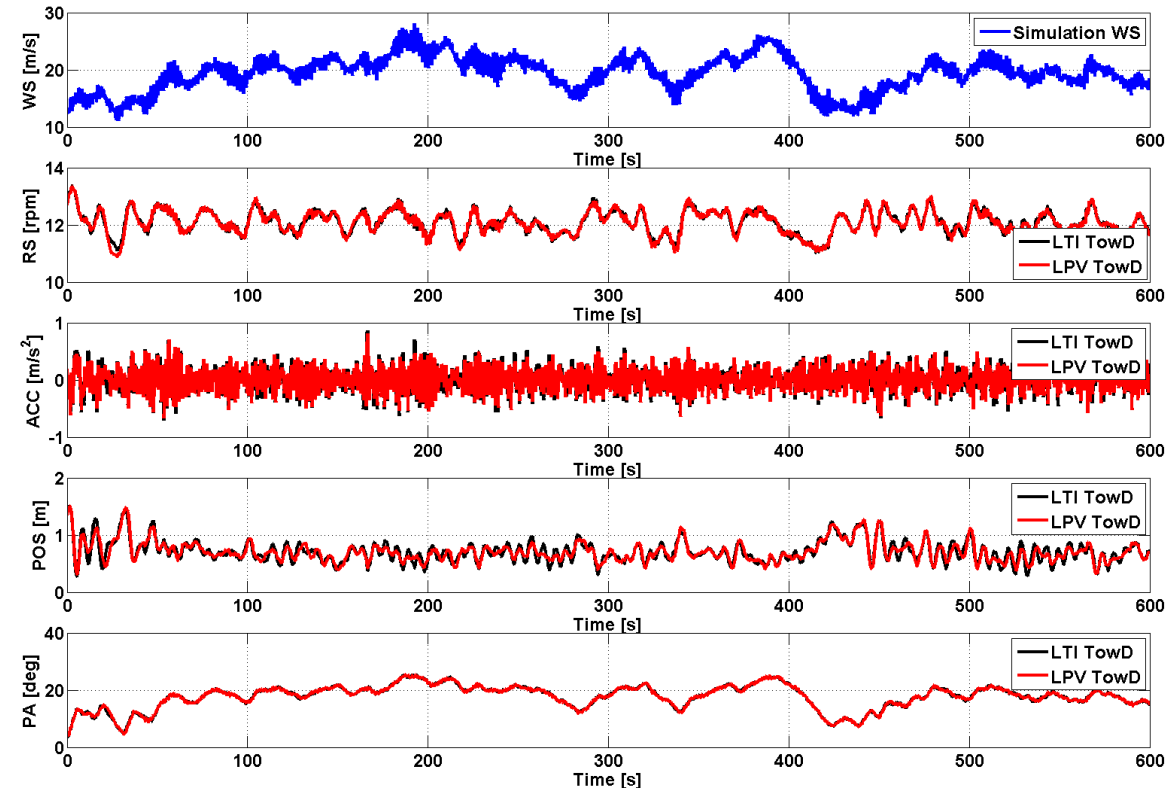

Figure 48: Time Series Comparison for Full-Load Conditions with Nominal and Off-Spec (-20% in NF) Tower for the ART 5 MW

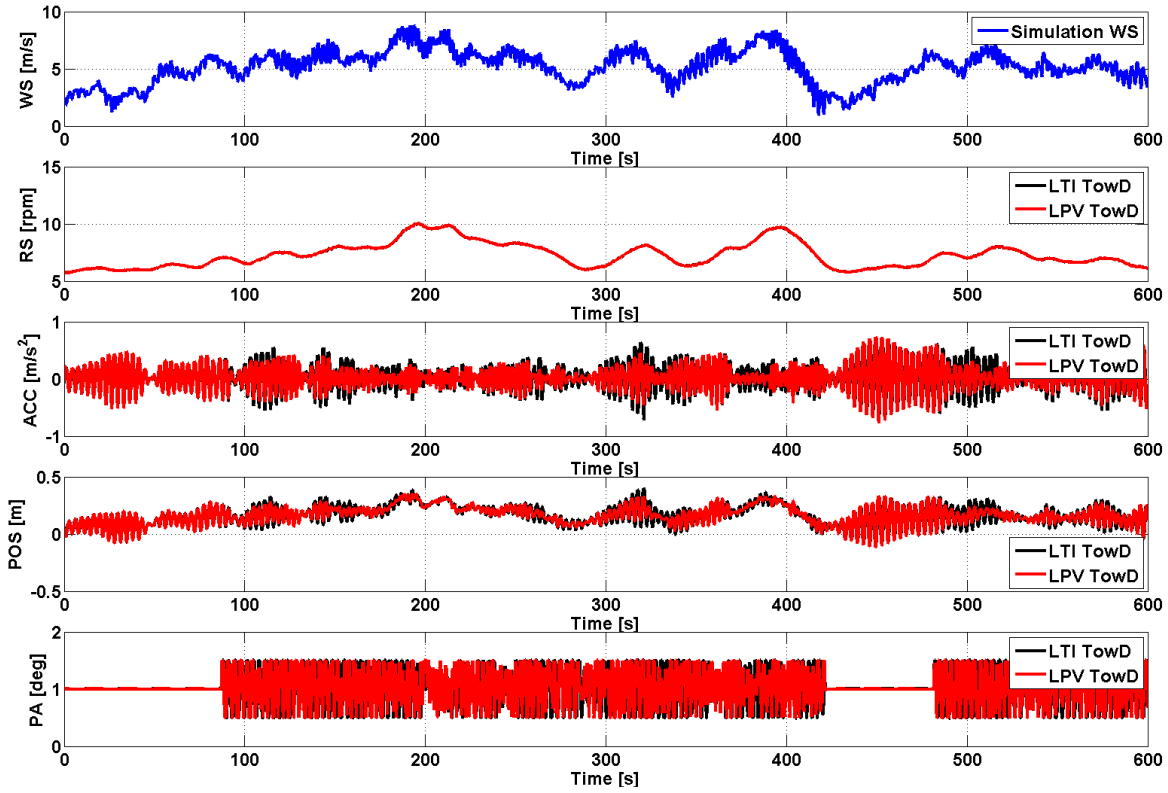

Figure 49: Time Series Comparison for Partial-Load Conditions with Nominal and Off-Spec (+20% in NF) Tower for the ART 5 MW

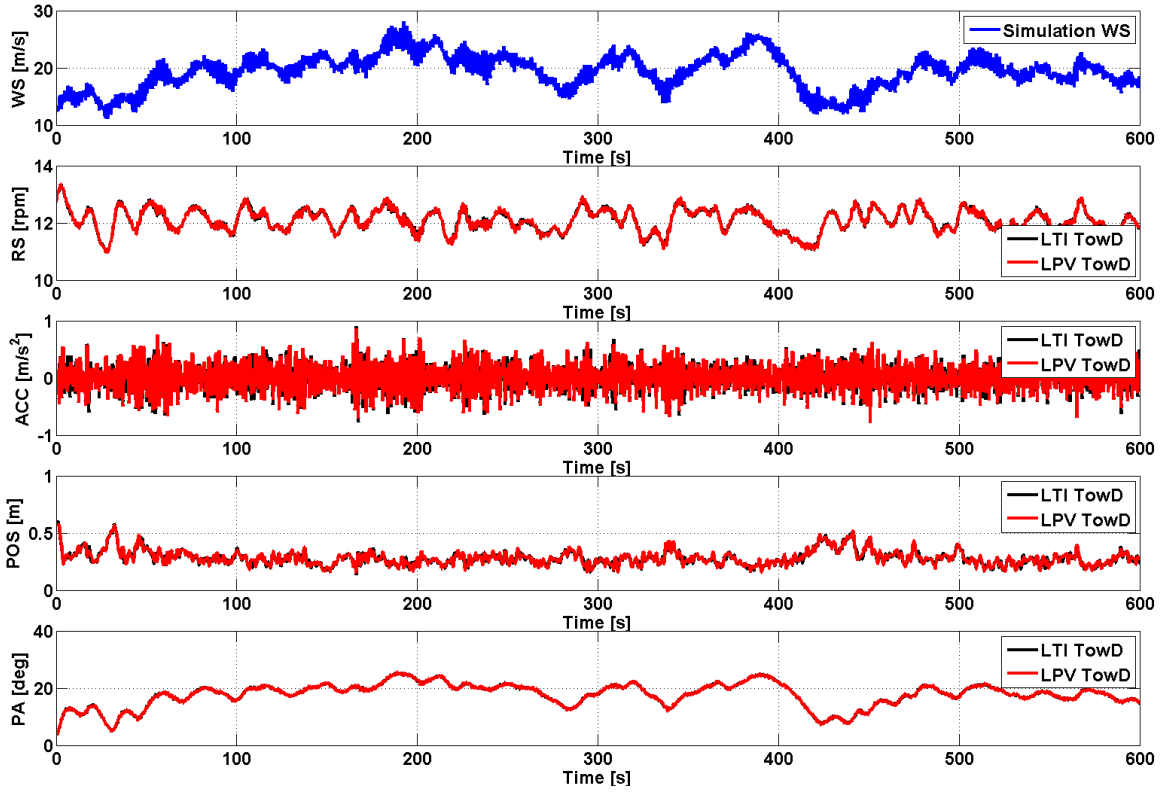

Figure 50: Time Series Comparison for Full-Load Conditions with Nominal and Off-Spec (+20% in NF) Tower for the ART 5 MW

5

Assessment and Recommendations

As an assessment of the reported work from **Chapter 3** and **Chapter 4** laid in the framework of **Chapter 2**, this chapter gives an overview of the presented material and a personal reflection on the formulated objectives of the project from **Chapter 1**. In relation to these, several propositions are made regarding possibilities for further improvements. The main goal of this brief account is to clearly delineate under what circumstances the considered design uncertainty in the aerodynamic and support structure properties of the wind turbine the can indeed be accounted for during the design phase from the perspective of control systems.

5.1 Reflection on Formulated Objectives and Evaluation

The performed work has been motivated by the current need of reducing the associated cost of energy from offshore wind farms by an overall reduction of uncertainties [66]. As has been explained, given the fact that the potential of wind at sea is considerable and yet the aspects triggered by wind turbine operation in such harsh environments tend to limit system performance, this approach towards the reduction of the cost of energy is indeed legitimate.

This specific project has aimed at revisiting a specific class of advanced control methodologies that can make explicit use of known uncertainty regarding wind turbine operation towards addressing these challenges; consequently, the framework of the project has been positioned within the robust and linear parameter-varying control theories.

In **Chapter 2** wind turbine control systems have been presented from the design and simulation point of view in relation to the project goals; subsequently, in **Chapter 3** sources of uncertainty in wind turbine operation have been investigated investigated in terms of the aerodynamic subsystem and the wind turbine support structure: while the considered factors, namely ice accretion wind turbine blades and deviations of the modal support structure characteristics from their designed values, have all shown to limit system performance, the chapter has also revealed which of these can indeed be addressed within the proposed framework. **Chapter 4** has described how linear parameter-varying control theory can be applied towards solving the encountered practical problem regarding the active tower damping control loop, yielding an improved performance of this loop of up to 9% compared to a design which does not account for the deviations in the modal characteristics of the turbine support structure.

The formulated goals of the assignment are considered to be achieved given the fact that knowledge has been derived regarding the amount to which the claimed factors do play a role in control system performance and also due to the subsequent improvement of the active tower damping control loop; both these areas of knowledge have the potential of reducing the cost of offshore wind energy if accounted for at future times.

5.2 Recommendations for Future Work

Though the goals of the project are considered to have been achieved, several detected existing problems have not been addressed, primarily due to time constraints. These problems are revisited below and remarks are made regarding possible methods of dealing with them.

Ice accretion on wind turbine rotors has been shown to be both very likely to happen in practice and problematic for wind turbine operation; this situation can be addressed as follows:

- **Ice Accommodation Control Systems**: As has been presented in the mentioned literature and also derived within the reported work, ice accretion on wind turbine blades drastically changes the power and thrust coefficient curves. For both considered ice accretion geometries this has been seen to represent a problem also for the turbine control systems, especially in terms of the power regulation and rotor speed control loop that does need to have an accurate model of the aerodynamic behaviour of the rotor for optimal control action. Energy losses, while mainly due to the accretion itself, can also occur due to the fact that the controllers do not account for these changes at all. Auxiliary control loops e.g. start-up control have also been seen to be affected. These can all be improved by using different control approaches than the ones within this project's framework; suitable alternative approaches are the ones that do allow for adapting the control action based on the changes that ice accretion implies [44, 50].

Additional solutions such as ice prevention systems mounted inside the turbine blades [60] also represent a possibility towards improved wind turbine power performance, yet, although attractive from a practical perspective, discussing such possibilities is outside the goals of the current project.

Variations in the support structure dynamics due to either environmental conditions or installation have also been seen to pose problems; these can addressed as follows:

- **Extensive Tower Damping Control Design**: The LPV approach to active tower damping control design has brought forward a method of reducing tower DELs compared to the worst case situation by explicitly accounting for the changes in the modal characteristics of the support structure and adapting the controller parameters according to such changes. However, these improvements are in practice limited by the following factors pertaining to the design itself: the methodology introduces some moderate conservatism in the design which could be investigated with respect to the allowed performance in terms of DELs and, furthermore, the manner in which the control objective function is formulated can be equally relevant for the design e.g. allowing for more aggressive pitch control action can result in further reduction of DELs at the potential price of less produced energy and higher DELs for the turbine blades or drivetrain, respectively. It is here considered that all these factors need to be appropriately balanced in the design of tower damping controllers, even for those scheduled based on the natural tower frequency proposed within this thesis;
- **Improved Tower Design and Installation**: As has been explained in the previous chapter, the increase in DELs for turbine support structures that are far from the designed characteristics can be attributed both to the employed controller whose design is typically carried in terms of the nominal system model and due to the form of the changed support structure dynamics themselves. For example, observe that in all cases where the natural tower frequency had dropped below the 1P frequency, the DELs seem to have grown considerably; in such cases, there would be very little that the considered control methodologies could do to improve the situation. It is, therefore, equally important for wind turbine manufacturers to ensure that the natural tower frequencies, even if different from their designed values, are not within the proximity of such dangerous regions.

As a final recommendation, the combined analysis of both ice accretion on turbine blades and changes in support structure properties can prove to be revealing of further potential issues.

Appendix A: Robust and Linear Parameter-Varying Control Theory

In this appendix, LMI-based robust and linear parameter-varying (LPV) control theory is briefly reviewed for setting the advanced control design background within which the formulated goals of the thesis have been achieved. These methodologies are able to make explicit use of uncertainty regarding a system model in order to provide reliable control designs of only moderate conservatism. First, a unified framework for the modeling of uncertain dynamical systems for robust and LPV control design is developed. The usefulness of LMI-based approaches for the control of the proposed system class is then shown. Further presented material covers both static state-feedback synthesis and dynamic output-feedback synthesis; based on the outlined topics, a full derivation for the synthesis that corresponds to the problem formulated in **Chapter 4** is given. As already discussed in **Chapter 4**, the control objective is formulated as a generalized $\mathcal{H}_2$ norm minimization problem.

A Framework for Modeling Uncertain Dynamical Systems

Most real-life processes behave globally as generic nonlinear systems [55]. However, when modeling the dynamics of a process for control design, simplifications are made either due to the fact that some phenomena are not relevant in practice or because the control design task becomes intractable if the model is overly complex - this usually leads to more specific descriptions [75]. During this modeling phase a mathematical description of the desired performance in the operation of this process also becomes available and is appended to its description - this gives rise to a so-called *generalized plant*. A generic framework available for the mathematical description of such plants relies on associating finite-dimensional continuous-time state-space models:

$$\left\{\begin{array}{rcl} \dot{x}_P(t) & = & f(x_P(t), u(t), w(t), t) \\ y(t) & = & g(x_P(t), u(t), w(t), t) \\ z(t) & = & h(x_P(t), u(t), w(t), t) \end{array}\right. \tag{1}$$

to them, where $f : \mathbb{R}^{n_p+m+o+1} \to \mathbb{R}^{n_p}$, $g : \mathbb{R}^{n_p+m+o+1} \to \mathbb{R}^{p}$ and $h : \mathbb{R}^{n_p+m+o+1} \to \mathbb{R}^{l}$ are smooth nonlinear functions of their variables:

$$\left\{\begin{array}{rcll} x_P(t) & \in & \mathbb{R}^{n_p} & \text{(state vector)} \\ u(t) & \in & \mathbb{R}^{m} & \text{(input vector)} \\ w(t) & \in & \mathbb{R}^{o} & \text{(generalized disturbance vector)} \\ t & \in & \mathbb{R}^{+} & \text{(continuous time)} \end{array}\right. \tag{2}$$

and where $y(t) \in \mathbb{R}^p$ and $z(t) \in \mathbb{R}^l$ represent the output/measurements vector and the performance outputs vector, respectively; these are all functions of the continuous time t. As mentioned, the generalized plant is a model of the process together with all the design specifications e.g. knowledge about the vector of generalized disturbances $w(t)$ or about the way in which the measurements $y(t)$ are produced, performance specifications on $z(t)$ or restrictions on the control signal $u(t)$. Although the representation (1) is convenient for a global definition of the underlying dynamics of the generalized plant, it is more common to express these as:

$$P : \left\{\begin{array}{rcl} \dot{x}_P(t) & = & A_P(\delta)x_P(t) + B_{P_u}(\delta)u(t) + B_{P_w}(\delta)w(t) \\ y(t) & = & C_{P_y}(\delta)x_P(t) + D_{P_{uy}}(\delta)u(t) + D_{P_{wy}}(\delta)w(t) \\ z(t) & = & C_{P_z}(\delta)x_P(t) + D_{P_{uz}}(\delta)u(t) + D_{P_{wz}}(\delta)w(t) \end{array}\right. \tag{3}$$

with $\delta \triangleq \delta(t)$ being used as a convenient notation; as there is usually no direct transfer from $u(t)$ to $y(t)$, the matrix $D_{P_{uy}}(\delta)$ is assumed to satisfy $D_{P_{uy}}(\delta) = 0, \forall \delta \in \Delta$. Nonlinear systems (1) can be transformed into systems of the form (3) either by following traditional *Jacobian-based methods of derivation*, where the linearization is performed explicitly along equilibrium operating trajectories, or by hiding away the nonlinearities in the system and including them in δ, which represents the so-called *quasi-LPV derivation*. Such models (3) are called linear parameter-dependent systems; these are linear state-space systems where all matrices are parametrized in terms of some parameter $\delta \in \mathbb{R}^{n_\delta}$, often called the *(scheduling) parameter vector* e.g. δ could define the operating trajectory of that carries (1) to (3). In this thesis, however, the parameter δ has been defined to be $\delta \triangleq \omega_n^{tow}$.

The parameter δ, assumed to be online-available, is only known *a priori* only up to a certain extent i.e. it is known to lie in some compact set $\Delta \subset \mathbb{R}^{n_\delta}$. Additionally, its rate of variation is assumed to be limited $\dot{\delta} \in \dot{\Delta} \triangleq \prod_{i=1}^{n_\delta} [\dot{\delta}_i^{inf}, \dot{\delta}_i^{sup}]$. Note that $\dot{\Delta}$ is an n_δ-dimensional convex polytope. Because δ is completely known at every time instant during operation, the system (3) is called an LPV system; if only part of the parameter vector were known, it would be called an uncertain LPV system. Finally, if the parameter vector is not known at all (3) becomes an uncertain system. LPV systems have been introduced in [79, 80] as an attempt of addressing the theoretical gaps in *ad-hoc* gain-scheduled control design methods for nonlinear systems [81, 57, 73]. Depending on the variation of δ with time, (3) can represent either a linear time-invariant (LTI) system if δ is independent of the time t i.e. $\dot{\delta}_i = 0, \forall i = \overline{1, n_\delta}$ or a linear time-varying (LTV) system if δ depends explicitly on t. Note that (3) can also be interpreted as an uncertain linear system whose realization depends on the parameter δ - the so-called *parametric uncertainty* structure. As can be seen, this framework is particularly flexible and can potentially fit many practical problems where real-life systems have been modeled first as in (1), then as in (3) - several reputed examples are given in [12, 17, 95] and within the current thesis this flexibility also plays an important role. Its relevance is also visible in the light of the fact that by making explicit use of such knowledge about the parameter vector, either of *a priori* type or *real-time* information, designed controllers - be them *static state-feedback*:

$$K: \quad u(t) \quad = \quad D_K(\delta) x_P(t) \tag{4}$$

with matrix $D_K(\delta)$ of appropriate dimensions or *dynamic output-feedback*:

$$K: \left\{ \begin{array}{rcl} \dot{x}_K(t) & = & A_K(\delta) x_K(t) + B_K(\delta) y(t) \\ u(t) & = & C_K(\delta) x_K(t) + D_K(\delta) y(t) \end{array} \right. \tag{5}$$

with $x_K(t) \in \mathbb{R}^{n_k}$ and matrices $A_K(\delta), B_K(\delta), C_K(\delta), D_K(\delta)$ of appropriate dimensions - can be robust in some sense, while only moderately conservative. These issues will be exhaustively explained throughout this appendix. Other possible approaches for the design of robust controllers are described extensively in e.g. [101, 14, 83], yet will not be considered here due to the fact that they do not provide a unified framework for tackling all possible systems within the class (3) and customizing the design problem based on the particular system type; these methodologies would trade optimality for robustness and therefore introduce unnecessary conservatism.

Closed-Loop Dynamical Systems and Relation to LMIs

The next step that needs to be taken after a control problem has been formulated as in (3) is to design a controller that guarantees the desired *closed-loop* behaviour - typically, the process within the generalized plant needs to be guaranteed to function safely and to have certain characteristics of operation; in systems-theoretic terms the former property could be called *stability* and the latter *performance*. The achievement of these properties is possible by using feedback control i.e. by creating an interconnection as shown in Figure 51, where the closed-loop system T is comprised of the *generalized plant* denoted by P and the *controller* K. The controller generates command signals $u(t)$ based on $x_P(t)$ or $y(t)$, respectively, with a goal of reducing the effects of the generalized disturbances $w(t)$ on the performance signals $z(t)$. In this part of the appendix, *stability* and *performance* conditions for continuous-time systems T are

derived in terms of LMIs; the obtained relations are at the core of the associated control design algorithms i.e. should these prospective algorithms be implemented and yield some optimal solution K for a given plant P, then both stability and performance of the closed-loop are guaranteed, subject to the imposed design criteria. For reasons of conciseness and ease of understanding, the discrete-time systems case is not explicitly covered.

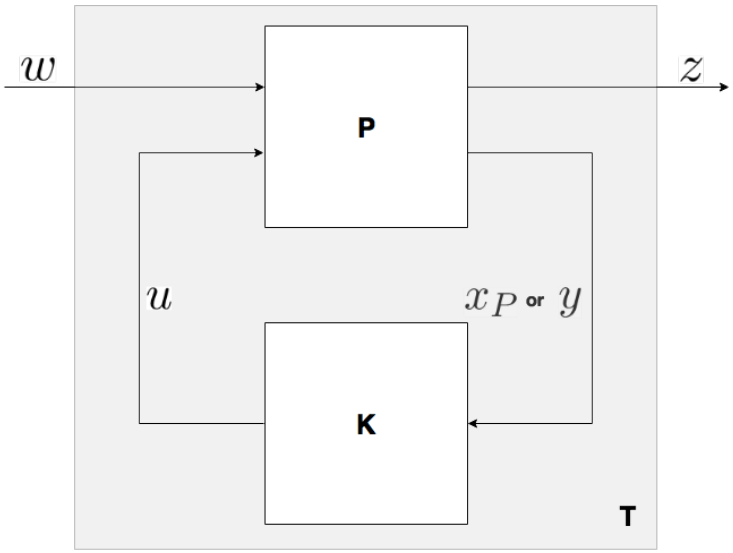

Figure 51: Generalized Feedback Interconnection (LFT)

The closed-loop system T, formed with generalized plant (3) and controller (4) or (5), is given by:

$$T : \begin{cases} \dot{x}(t) &= A(\delta)x(t) + B(\delta)w(t) \\ z(t) &= C(\delta)x(t) + D(\delta)w(t) \end{cases} \tag{6}$$

with $x^T(t) \triangleq x_P^T(t)$ for static state-feedback control or $x^T(t) \triangleq \begin{bmatrix} x_P^T(t) & x_K^T(t) \end{bmatrix}$ for dynamic output-feedback control and matrices $A(\delta), B(\delta), C(\delta), D(\delta)$ computed by forming the linear fractional interconnection (LFT).

The issue of closed-loop stability is considered first: T is said to be *quadratically stable* if there exists a (quadratic) function $\mathcal{V}_{stab} : \mathbb{R}^{n_p+n_k} \to \mathbb{R}$, $\mathcal{V}_{stab}(x(t)) = x^T(t)Xx(t)$ with $X = X^T$, called *Lyapunov stability function*, such that [75]:

$$\begin{cases} X &\succ 0 \\ A^T(\delta)X + XA(\delta) &\prec 0 \end{cases} \tag{7}$$

for $\forall \delta \in \Delta$. This convenient particular form for the Lyapunov stability function follows immediately from the classical stability analysis methods of Aleksandr Lyapunov for linear systems [61] and will continue to reflect system linearity [96, 97] in (6). Note that the requirement of having a single Lyapunov matrix for the entire set Δ is very conservative and also introduces *stability robustness* against arbitrarily-fast changes in the parameter $\delta \in \Delta$ (i.e. considers $\dot{\Delta} = \mathbb{R}^{n_\delta}$, see e.g. [76]). In practice, this may be undesirable and, as explained later, will be avoidable by making further requirements on the form of the Lyapunov function $\mathcal{V}_{stab}$.

As a second control design task, it is important to ensure that the signal $w(t)$ is attenuated by the closed-loop system T such that its effects on $z(t)$ are limited: this property of the closed-loop system is called $dissipativity$. The fact

that (6) should be *dissipative with respect to a supply rate* $s(w(t), z(t))$ means that there exists a differentiable function $\mathcal{V}_{dissip} : \mathbb{R}^{n_p+n_k} \to \mathbb{R}$, called *Lyapunov storage function*, such that [75]:

$$\frac{\partial}{\partial x}\mathcal{V}_{dissip}(x(t)) \preceq s(w(t), z(t)) \tag{8}$$

along all possible state trajectories $x(t)$. For a physical interpretation of this property, a system which satisfies the *differential dissipation inequality* (8) will always have internally less energy than it has been supplied or, at the most, the exact same amount; part of the energy supplied to the system is stored and part of it is dissipated. By following the same reasoning as previously, a convenient relevant choice for the supply rate $s(w(t), z(t))$ is to have it quadratic:

$$s(w(t), z(t)) = \begin{bmatrix} w(t) \\ z(t) \end{bmatrix}^T \begin{bmatrix} Q & S \\ S^T & R \end{bmatrix} \begin{bmatrix} w(t) \\ z(t) \end{bmatrix} \tag{9}$$

with symmetric matrices $Q \in \mathbb{R}^o$ and $R \in \mathbb{R}^l$ (this holds only if the pair $(A(\delta), B(\delta))$ is controllable for $\forall\delta \in \Delta$). Note that the proposed supply rate $s(w(t), z(t))$ in (9) can also be written in terms of the internal state $x(t)$ and the exogenous input $w(t)$ as:

$$s(w(t), z(t)) = \begin{bmatrix} x(t) \\ w(t) \end{bmatrix}^T \begin{bmatrix} 0 & I \\ C(\delta) & D(\delta) \end{bmatrix}^T \begin{bmatrix} Q & S \\ S^T & R \end{bmatrix} \begin{bmatrix} 0 & I \\ C(\delta) & D(\delta) \end{bmatrix} \begin{bmatrix} x(t) \\ w(t) \end{bmatrix} \tag{10}$$

With this quadratic supply rate, the requirement for the satisfaction of the dissipation inequality (8) becomes: the system (6) is dissipative with respect to the supply rate (10) if the controllable system T admits a quadratic Lyapunov storage function $\mathcal{V}_{dissip}(x(t)) = x^T(t)Xx(t)$ with $X = X^T$ such that:

$$\begin{bmatrix} A^T(\delta)X + A(\delta)X & XB(\delta) \\ B^T(\delta)X & 0 \end{bmatrix} - \begin{bmatrix} 0 & I \\ C(\delta) & D(\delta) \end{bmatrix}^T \begin{bmatrix} Q & S \\ S^T & R \end{bmatrix} \begin{bmatrix} 0 & I \\ C(\delta) & D(\delta) \end{bmatrix} \preceq 0 \tag{11}$$

Just as in (7), this approach is conservative and the single Lyapunov matrix X will also introduce *performance robustness* against arbitrarily-fast δ parameter changes. For now, by satisfying both (7) and (11) simultaneously, the closed-loop system is both robustly quadratically stable and achieves some robust quadratic performance criteria. Although stability is easily characterized, in general, performance can be specified in many different ways [101]. One particular type of closed-loop performance specifications of interest in this thesis is the *generalized $\mathcal{H}_2$ performance* or the so-called *energy-to-peak* gain of the system T, see e.g. [77, 28, 32, 100, 31]. Should $w(t)$ be a random signal with a Gaussian probability density function (PDF) and constant power spectral density (PSD), often called a white noise signal, this performance type describes the asymptotic variance of the output $z(t)$:

$$\|T\|_2^2 \triangleq \lim_{t\to\infty} E\left\{z^T(t)z(t)\right\} \tag{12}$$

for a given realization of $w(t)$; as a similar (but deterministic) interpretation, it can be said that (12) summarizes the effect of the signal $w(t)$ on the energy sum of transients in the signal $z(t)$. If $A(\delta)$ is stable and $D(\delta) = 0$ in (6) for $\forall\delta \in \Delta$, then $\|T\|_2$ is finite and can be equivalently described by [76]:

$$\|T\|_2 = \sup_{0<\|w\|_2<\infty} \frac{\|Tw\|_\infty}{\|w\|_2} \tag{13}$$

An attenuation of finite level γ of the signal $w(t)$ by T towards $z(t)$ will hence be denoted by $\|T\|_2 < \gamma$; it will be achievable for the system (6) with $A(\delta)$ stable and $D(\delta) = 0$ either if there exists a matrix $X = X^T$ such that:

$$\begin{cases} trace(C(\delta)XC(\delta)^T) & < & \gamma^2 \\ A(\delta)X + XA^T(\delta) + B(\delta)B^T(\delta) & \prec & 0 \end{cases} \tag{14}$$

or, equivalently, if there exists a matrix $Y = Y^T$ so that:

$$\begin{cases} trace(B(\delta)^T Y B(\delta)) & < & \gamma^2 \\ A^T(\delta)Y + YA(\delta) + C^T(\delta)C(\delta) & \prec & 0 \end{cases} \tag{15}$$

Analogous derivations can be conducted for discrete-time closed-loop systems:

$$T : \begin{cases} x(k+1) & = & A(\delta)x(k) + B(\delta)w(k) \\ z(k) & = & C(\delta)x(k) + D(\delta)w(k) \end{cases} \tag{16}$$

formed with the discrete-time equivalents of the generalized plant (3) and of the controller (4) or (5) and the mentioned customizations and assumptions; here $k \in \mathbb{Z}^+$ will represent the discrete time instants of which all signals are functions e.g. even $\delta \triangleq \delta(k)$. Similar inequalities to (7), (11), (14) and (15) would then be arrived at and the equivalent interpretations could be given, *mutatis mutandis*. One such example will be considered in the next section.

All inequalities (7), (11), (14) and (15) are actually LMIs parametrized in terms of δ and they capture the desired characteristics of the closed-loop system also from a computational point of view; such inequalities are very attractive due to their many interesting properties. Mathematically, they are part of LMI optimization, which is a subfield of semidefinite programming (SDP) with the objective customized to finding some vector $\kappa \in \mathbb{R}^{n_\kappa}$ such that:

$$F(\kappa) \triangleq F_0 + \sum_{i=1}^{n_\kappa} \kappa(i) F_i \succeq 0 \tag{17}$$

for symmetric matrices $F_0 \in \mathbb{R}^{n_F \times n_F}$ and $F_i \in \mathbb{R}^{n_F \times n_F}$, $i = \overline{1, n_\kappa}$. For instance, considering (14) again, κ will contain the independent entries of the symmetric matrix X.

While LMIs do have a long history in both systems and control theory, their use has become especially popular during the past two decades due to the availability of computationally-efficient methods applicable to solving semidefinite programs [65, 16, 43]. For a detailed, although not up-to-date review, the reader is referred to [19].

Reducing the Conservatism

As mentioned, the relations (7), (11), (14) and (15) characterize robustness of both closed-loop stability and performance for all possible parameters $\delta \in \Delta$ and against arbitrarily-fast parameter changes; controllers designed such that these conditions are guaranteed to be met are called *robust controllers*. Although attractive from some points of view, this type of controllers tends to yield an unreasonable compromise between stability and performance.

In practice, it may be desirable to allow for a more balanced trade-off between these two properties of the closed-loop system; this is possible within the presented framework by allowing for parameter-dependent Lyapunov functions (PDLFs) which is still a conservative approach, but not as much as the previous one.

The presented relations then specialize to:

$$(7) \quad \overset{PDLFs}{\Longrightarrow} \quad \begin{cases} X(\delta) & \succ & 0 \\ A^T(\delta)X(\delta) + X(\delta)A(\delta) + \dot{X}(\delta) & \prec & 0 \end{cases}$$

$$(11) \quad \overset{PDLFs}{\Longrightarrow} \quad \begin{bmatrix} A^T(\delta)X(\delta) + A(\delta)X(\delta) + \dot{X}(\delta) & X(\delta)B(\delta) \\ B^T(\delta)X(\delta) & 0 \end{bmatrix} - \begin{bmatrix} 0 & I \\ C(\delta) & D(\delta) \end{bmatrix}^T \begin{bmatrix} Q & S \\ S^T & R \end{bmatrix} \begin{bmatrix} 0 & I \\ C(\delta) & D(\delta) \end{bmatrix} \preceq 0$$

$$(14) \quad \overset{PDLFs}{\Longrightarrow} \quad \begin{cases} trace(C(\delta)X(\delta)C(\delta)^T) & < & \gamma^2 \\ A(\delta)X(\delta) + X(\delta)A^T(\delta) + \dot{X}(\delta) + B(\delta)B^T(\delta) & \prec & 0 \end{cases}$$

$$(15) \quad \overset{PDLFs}{\Longrightarrow} \quad \begin{cases} trace(B(\delta)^T Y(\delta)B(\delta)) & < & \gamma^2 \\ A^T(\delta)Y(\delta) + Y(\delta)A(\delta) + \dot{Y}(\delta) + C^T(\delta)C(\delta) & \prec & 0 \end{cases}$$

Under some further assumptions on the parameter dependency, synthesis methods for guaranteeing that these new conditions are met generically lead to *LPV controllers*.

Allowing for Numerical Tractability

Although presented as LMIs in their respective variables, the relations (7), (11), (14) and (15) as well as their PDLF-based counterparts are, as has been mentioned, parametrized in terms of δ; given that no explicit dependence has been assumed on the parameter δ, every LMI will be *infinite-dimensional*; what is more, because of the fact that these conditions need to hold true at all points $\delta \in \Delta$, an *infinite number* of LMIs will arise for each individual inequality. These two facts make the associated optimization problems numerically intractable [9]. To address the infinite-dimensionality issue, the system matrices are assumed to be *affinely-dependent* on the parameter δ:

$$\begin{cases} A(\delta) & = & A_0 & + & \sum_{i=1}^{n_\delta} \delta_i A_i \\ B(\delta) & = & B_0 & + & \sum_{i=1}^{n_\delta} \delta_i B_i \\ C(\delta) & = & C_0 & + & \sum_{i=1}^{n_\delta} \delta_i C_i \\ D(\delta) & = & D_0 & + & \sum_{i=1}^{n_\delta} \delta_i D_i \end{cases} \tag{18}$$

This can happen either natively or by replacing the initially considered parameter with another one that does allow for this formulation. Note that the previous requirement for the validity of (14) and (15) implies that $D_i = 0,\ i = \overline{1, n_\delta}$ and $D_0 = 0$. For LPV synthesis it is typically imposed that the Lyapunov matrices satisfy the same parametrization:

$$\begin{cases} X(\delta) & = & X_0 & + & \sum_{i=1}^{n_\delta} \delta_i X_i \\ Y(\delta) & = & Y_0 & + & \sum_{i=1}^{n_\delta} \delta_i Y_i \end{cases} \tag{19}$$

and these will imply $\dot{X}(\delta) = \sum_{i=1}^{n_\delta} \dot{\delta}_i X_i$ and $\dot{Y}(\delta) = \sum_{i=1}^{n_\delta} \dot{\delta}_i Y_i$, respectively.

For addressing the issue of infinite number of LMI relations, one tries to exploit convenient properties of LMIs. Should it hold true that, after substituting these mentioned affine forms of the matrices in the LMIs associated with the derived conditions for closed-loop stability and performance, these will depend affinely on the parameter δ, then the solution is trivial: one approximates the given set Δ by some n_δ-dimensional convex polytope $\boldsymbol{\Delta}$ with $N_{\boldsymbol{\Delta}}$ vertices $\{\Gamma_1, \Gamma_2, ..., \Gamma_{N_{\boldsymbol{\Delta}}}\}$ i.e. a closed set of points $\delta \in \mathbb{R}^{n_\delta}$ that lie in the convex hull of $\{\Gamma_1, \Gamma_2, ..., \Gamma_{N_{\boldsymbol{\Delta}}}\}$ and satisfy $\delta = \sum_{j=1}^{N_{\boldsymbol{\Delta}}} \alpha_j \Gamma_j$ with $\alpha_j \geq 0, \forall j = \overline{1, N}_{\boldsymbol{\Delta}}$ and $\sum_{j=1}^{N_{\boldsymbol{\Delta}}} \alpha_j = 1$ (see e.g. [20]) and checks the corresponding LMI conditions only at the vertices of the joint definition polytope $\boldsymbol{\Delta} \times \dot{\Delta}$. However, this will only be possible for the robust synthesis case; for LPV synthesis the obtained LMIs will no longer be affine in δ, hence it would be necessary to introduce dummy parameters to hide away the non-affine dependencies, extend the parameter vector and bound the associated space

of the extended parameter vector by some other convex polytope - this is, yet again, potentially conservative [8, 7, 6]. The multi-convexity property could be used as an alternative but only in some special cases [42, 84].

One other possibility, solving both issues mentioned above, is to grid $\boldsymbol{\Delta}$ and check that the LMI conditions for every grid point within the defined grid are satisfied [99, 13]; note that all the parameter-dependent matrices in the grid are convex combinations of their correspondents at the vertices of the convex polytope Δ; this procedure does, however, only provide guarantees for the defined grid and the associated points, therefore the grid density needs to be iteratively increased in order to have reliable obtained results - this, in turn, dramatically increases the number of LMIs; what is more, a very fine grid can even make the LMI system infeasible, in which case the grid density should be decreased.

One final alternative is the so-called probabilistic approach [86, 22, 67, 41] which relies on the use of randomized iterative algorithms; these converge in a finite number of steps only if the problem is feasible; this approach can provide guarantees for all possible parameter values yet it requires a very large number of iterations for this, a fact which makes it less practical.

For the remaining part of this appendix, as well as for **Chapter 4** the following statements will hold true regarding the framework used for controller synthesis:

- the parameter dependency of (3) on $\delta \triangleq \omega_n^{tow}$ is natively affine; for **reduced conservatism** LPV controller design is desired, therefore all Lyapunov matrices are imposed to be affinely parameter-dependent;

- for **numerical tractability** the gridding approach will be used with as fine a grid as possible;

- to allow for **direct implementation** without the risk of loss of performance due to controller post-design discretization, the synthesis is carried in discrete-time; for this (3) first needs to be discretized appropriately; this is partly explained in the last part of this appendix and partly explained in **Chapter 4**.

LPV Dynamic Output-Feedback Control: The Discrete-Time Case

In this part of the appendix, one possible derivation of a solution to the generalized $\mathcal{H}_2$ LPV dynamic output-feedback control synthesis problem for discrete-time systems is shown from the same LMI viewpoint previously introduced. As already mentioned, it will be assumed throughout this exposition that the parameter δ natively belongs to a convex polytope $\boldsymbol{\Delta}$. Moreover, the rate of variation of all its components is considered to be very slow $\dot{\delta}_i \cong 0, \forall i = \overline{1, n_\delta}$ and hence $\dot{\Delta} = 0_{n_\delta}$ due to practical reasons regarding the mentioned choice of δ; this will imply that $\dot{X}(\delta) = 0$ and $\dot{Y}(\delta) = 0$. The system matrices will be assumed to be parameter-dependent $A(\delta), B(\delta), C(\delta)$ with the exception of $D(\delta) = 0$. For LPV synthesis affine parameter dependence is used in the Lyapunov matrices as previously explained; as expected, the obtained LPV controller K will in fact denote a parametrized family of controllers, scheduled on the values that δ takes. As will be seen, whereas initially an unsuitable synthesis problem arises, by a suitable change of variables it can be conveniently recast towards implementation.

For the case of dynamic output-feedback LPV control, the LFT interconnection previously shown in Figure 51, now formed with the discrete-time generalized plant P:

$$P : \left\{ \begin{array}{rcl} x_P(k+1) & = & A_P(\delta)x_P(k) + B_{P_u}(\delta)u(k) + B_{P_w}(\delta)w(k) \\ y(k) & = & C_{P_y}(\delta)x_P(k) + D_{P_{uy}}(\delta)u(k) + D_{P_{wy}}(\delta)w(k) \\ z(k) & = & C_{P_z}(\delta)x_P(k) + D_{P_{uz}}(\delta)u(k) + D_{P_{wz}}(\delta)w(k) \end{array} \right. \tag{20}$$

and discrete-time dynamic output-feedback controller K:

$$K : \left\{ \begin{array}{rcl} x_K(k) & = & A_K(\delta)x_K(k) + B_K(\delta)y(k) \\ u(k) & = & C_K(\delta)x_K(k) + D_K(\delta)y(k) \end{array} \right. \tag{21}$$

will be given as shown in Figure 52. Note that the measurements vector $y(k)$ is part of the generalized plant P and the controller only has access to the measured output $y(k)$. The matrices (16) of the closed-loop system T are in this case given by:

$$\left\{ \begin{array}{rcl} A(\delta) & = & \begin{bmatrix} A_P(\delta) + B_{P_u}(\delta)D_K(\delta)C_{P_y}(\delta) & B_{P_u}(\delta)C_K(\delta) \\ B_K(\delta)C_{P_y}(\delta) & A_K(\delta) \end{bmatrix} \\ B(\delta) & = & \begin{bmatrix} B_{P_w}(\delta) + B_{P_u}(\delta)D_K(\delta)D_{P_{wy}}(\delta) \\ B_K(\delta)D_{P_{wy}}(\delta) \end{bmatrix} \\ C(\delta) & = & \begin{bmatrix} C_{P_z}(\delta) + D_{P_{uz}}(\delta)D_K(\delta)C_{P_y}(\delta) & D_{P_{uz}}(\delta)C_K(\delta) \end{bmatrix} \\ D(\delta) & = & \begin{bmatrix} D_{P_{wz}}(\delta) + D_{P_{uz}}(\delta)D_K(\delta)D_{P_{wy}}(\delta) \end{bmatrix} \end{array} \right. \tag{22}$$

Several remarks are first in order: because $D(\delta) = 0$ is to be imposed for generalized $\mathcal{H}_2$ synthesis, as previously mentioned, $D_{P_{wz}}(\delta) = 0$ in (22) as usual; what is more, because no further assumptions are now made regarding $D_{P_{uz}}(\delta)$ and/or $D_{P_{wy}}(\delta)$ in (22), when implemented for control design, the proposed optimization problem will always deliver $D_K(\delta) = 0$ for the same reason. These two are, hence, omitted in Figure 52.

For solving the synthesis problem i.e. finding a controller K in such that the closed-loop system has $\|T\|_2 < \gamma$ for all $\delta \in \boldsymbol{\Delta}$, it is necessary to find feasible solutions $X(\delta) = X^T(\delta)$ and $Q = Q^T$ to the optimization problem:

$$\begin{array}{ll} \text{min} & \gamma^2 \\ \text{over all} & \delta \in \boldsymbol{\Delta} \\ \text{subject to} & \left\{ \begin{array}{rcl} \begin{bmatrix} X(\delta) & X(\delta)A(\delta) & X(\delta)B(\delta) \\ \star & X(\delta) & 0 \\ \star & \star & I \end{bmatrix} & \prec & 0 \\ \begin{bmatrix} Q & C(\delta) \\ \star & X(\delta) \end{bmatrix} & \succ & 0 \\ trace(Q) & < & \gamma^2 \end{array} \right. \end{array} \tag{23}$$

As specified, the Lyapunov matrix $X(\delta)$ is affinely-dependent on the parameter δ i.e. $X(\delta) = X_0 + \sum_{i=1}^{n_\delta} \delta_i X_i$. Notice that the constraints associated to the optimization problem (23) are not convex due to products between the Lyapunov matrix $X(\delta)$ and the controller matrices $A_K(\delta)$, $B_K(\delta)$, $C_K(\delta)$ and $D_K(\delta)$ in the closed-loop system matrices $A(\delta)$ and $B(\delta)$, respectively. However, if $X(\delta)$ is partitioned as:

$$X(\delta) = \begin{bmatrix} R(\delta) & U(\delta) \\ U^T(\delta) & Z(\delta) \end{bmatrix} \tag{24}$$

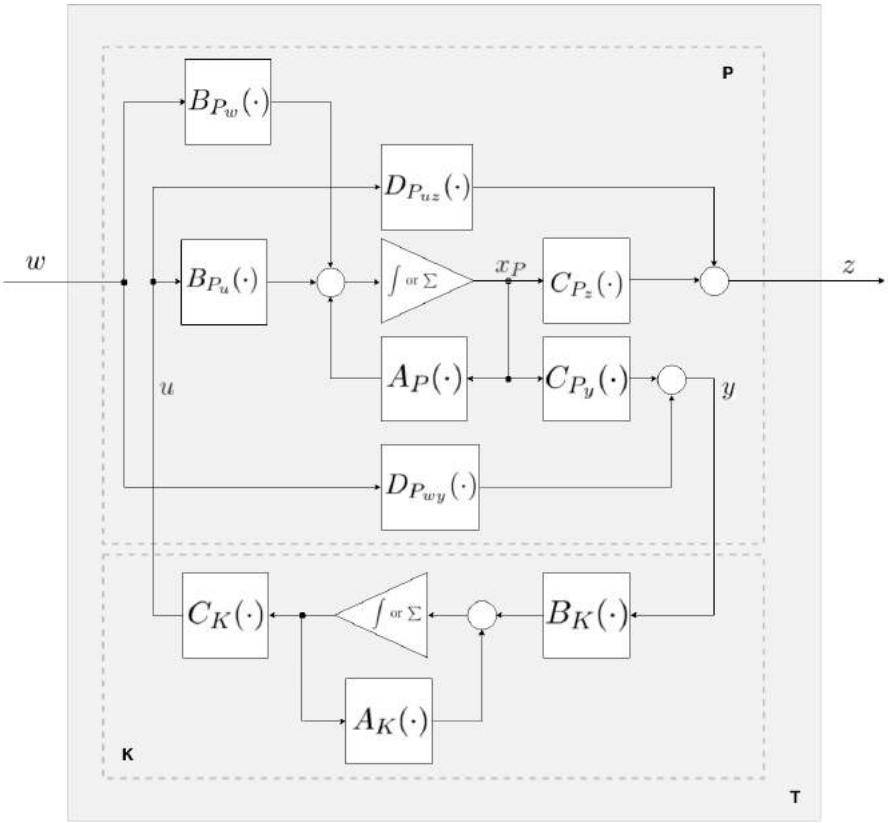

Figure 52: LFT Interconnection for $\mathcal{H}_2$ Dynamic Output-Feedback Control

then $X^{-1}(\delta)$ is given by a similar partitioning:

$$X^{-1}(\delta) = \begin{bmatrix} S(\delta) & V(\delta) \\ V^T(\delta) & W(\delta) \end{bmatrix} \tag{25}$$

and by further introducing the matrix variable $Y(\delta)$:

$$Y(\delta) = \begin{bmatrix} S(\delta) & I \\ V^T(\delta) & 0 \end{bmatrix} \tag{26}$$

the following change of variables becomes suitable:

$$\begin{bmatrix} K(\delta) & L(\delta) \\ M(\delta) & N(\delta) \end{bmatrix} = \begin{bmatrix} U(\delta) & R(\delta)B_{P_u}(\delta) \\ 0 & I \end{bmatrix} \begin{bmatrix} A_K(\delta) & B_K(\delta) \\ C_K(\delta) & D_K(\delta) \end{bmatrix} \begin{bmatrix} V^T(\delta) & 0 \\ C_{P_y}(\delta)S(\delta) & I \end{bmatrix} + \begin{bmatrix} R(\delta)A_P(\delta)S(\delta) & 0 \\ 0 & 0 \end{bmatrix} \tag{27}$$

for rendering the problem convex. This is achieved by the left-side and right-side matrix multiplication of the LMI

constraints in (23):

$$\begin{bmatrix} Y^T(\delta) & 0 & 0 \\ \star & Y^T(\delta) & 0 \\ \star & \star & Y^T(\delta) \end{bmatrix} \cdot \underbrace{\begin{bmatrix} X(\delta) & X(\delta)A(\delta) & X(\delta)B(\delta) \\ \star & X(\delta) & 0 \\ \star & \star & I \end{bmatrix} \prec 0}_{\text{part of } (23)} \cdot \begin{bmatrix} Y(\delta) & 0 & 0 \\ \star & Y(\delta) & 0 \\ \star & \star & Y(\delta) \end{bmatrix} \tag{28}$$

and:

$$\begin{bmatrix} I & 0 \\ \star & Y^T(\delta) \end{bmatrix} \cdot \underbrace{\begin{bmatrix} Q & C(\delta) \\ \star & X(\delta) \end{bmatrix} \succ 0}_{\text{part of } (23)} \cdot \begin{bmatrix} I & 0 \\ \star & Y(\delta) \end{bmatrix} \tag{29}$$

the LMI constraints in (23) then become affine in the unknowns $S(\delta)$, $R(\delta)$, $K(\delta)$, $L(\delta)$, $M(\delta)$, $N(\delta)$ and Q:

$$\begin{bmatrix} S(\delta) & I & A_P(\delta)S(\delta)+B_{P_u}(\delta)M(\delta) & A_P(\delta)+B_{P_u}(\delta)N(\delta)C_{P_y}(\delta) & B_{P_w}(\delta)+B_{P_u}(\delta)N(\delta)D_{P_{wy}}(\delta) \\ \star & R(\delta) & K(\delta) & S(\delta)A_P(\delta)+L(\delta)C_{P_y}(\delta) & S(\delta)B_{P_w}(\delta)+L(\delta)D_{P_{wy}}(\delta) \\ \star & \star & S(\delta) & I & 0 \\ \star & \star & \star & R(\delta) & 0 \\ \star & \star & \star & \star & I \end{bmatrix} \prec 0$$

$$\begin{bmatrix} Q & C_{P_z}(\delta)S(\delta)+D_{P_{uz}}(\delta)M(\delta) & C_{P_z}(\delta)+D_{P_{uz}}(\delta)N(\delta)C_{P_y}(\delta) \\ \star & S(\delta) & I \\ \star & \star & R(\delta) \end{bmatrix} \succ 0$$

$$trace(Q) < \gamma^2 \tag{30}$$

Note that although all synthesis matrices are imposed to be affinely parameter-dependent:

$$\begin{cases} S(\delta) = S_0 + \sum_{i=1}^{n_\delta} \delta_i S_i \\ R(\delta) = R_0 + \sum_{i=1}^{n_\delta} \delta_i R_i \\ K(\delta) = K_0 + \sum_{i=1}^{n_\delta} \delta_i K_i \\ L(\delta) = L_0 + \sum_{i=1}^{n_\delta} \delta_i L_i \\ M(\delta) = M_0 + \sum_{i=1}^{n_\delta} \delta_i M_i \\ N(\delta) = N_0 + \sum_{i=1}^{n_\delta} \delta_i N_i \end{cases} \tag{31}$$

The LMI constraints (30) are still not affine in the parameter δ, therefore the gridding approach will be used to solve the optimization problem (23) with constraints (30), as mentioned.

From the previous synthesis relations (30), the controller matrices are arrived at by performing the reverse substitutions, one by one:

$$\begin{cases} D_K(\delta) &= N(\delta) \\ C_K(\delta) &= \left(M(\delta) - D_K(\delta)C_{P_y}(\delta)S(\delta)\right)V^{-T}(\delta) \\ B_K(\delta) &= U^{-1}(\delta)\left(L(\delta) - R(\delta)B_{P_u}(\delta)D_K(\delta)\right) \\ A_K(\delta) &= U^{-1}(\delta)\left[\left(K(\delta) - L(\delta)C_{P_y}(\delta)S(\delta) - R(\delta)A_P(\delta)S(\delta)\right)V^{-T}(\delta) - R(\delta)B_{P_u}(\delta)C_K(\delta)\right] \end{cases} \tag{32}$$

Note here that $U(\delta)$ and $V^T(\delta)$ are required, yet not directly available from the solution of the optimization problem; however, by making use of the fact that $X(\delta)X^{-1}(\delta) = I$ and of the partitioning (24) and (25) of $X(\delta)$ and $X^{-1}(\delta)$, respectively, these can be obtained e.g. by performing an SVD:

$$U(\delta)V^T(\delta) = \underbrace{I - R(\delta)S(\delta)}_{\Xi(\delta)\Sigma(\delta)\Psi^T(\delta)} \tag{33}$$

and choosing $U(\delta) = \Xi(\delta)\Sigma(\delta)$ and $V^T = \Psi^T$.

The following algorithm gives an overview of how the synthesis procedure presented in this section can be used for **Chapter 4**:

Step 1 (Offline) : define $\delta \triangleq \omega_n^{tow}$ and choose a range for $\delta \in \boldsymbol{\Delta} \triangleq \left[\omega_{n,inf}^{tow}, \omega_{n,sup}^{tow}\right]$;

Step 2 (Offline) : choose a fine grid of points for the parameter space $\boldsymbol{\Delta}$;

Step 3 (Offline) : for every grid point find the associated set of polytopic scheduling weights;

Step 4 (Offline) : for every set of polytopic scheduling weights find the generalized plant (3) by using on the current value of δ and discretize it using e.g. a sampling period T_s and ZOH discretization; this leads to one system (20) for every grid point defined;

Step 5 (Offline) : for all defined grid points construct the full optimization problem (23) by stacking the associated constraints (30) for every grid point and solve it using e.g. [43]; a set of matrices $S(\delta)$, $R(\delta)$, $K(\delta)$, $L(\delta)$, $M(\delta)$, $N(\delta)$ is arrived at for every vertex of the defined parameter polytope Δ;

Step 6 (Online) : at time instant k determine ω_n^{tow} and use $\delta = \omega_n^{tow}$; find the associated set of polytopic scheduling weights;

Step 7 (Online) : based on the polytopic set of scheduling weights at discrete-time instant k, find the current plant (3) by using on the current value of δ and discretize it using e.g. a sampling period T_s and ZOH discretization; extract matrices A_P, B_{P_u} and C_{P_y} for later use;

Step 8 (Online) : based on the polytopic set of scheduling weights at time discrete-time instant k, find the current synthesis matrices $S(\delta)$, $R(\delta)$, $K(\delta)$, $L(\delta)$, $M(\delta)$, $N(\delta)$ from (31);

Step 9 (Online) : based on the current values of $S(\delta)$ and $R(\delta)$, find the current values of $U(\delta)$ and $V^T(\delta)$ in a time-efficient manner e.g. by setting $U(\delta) = I - R(\delta)S(\delta)$ and $V^T(\delta) = I$ in (33);

Step 10 (Online) : use the reverse substitution (32) to find the current controller matrices based on the calculated $A_P(\delta)$, $B_{P_u}(\delta)$, $C_{P_y}(\delta)$, $S(\delta)$, $R(\delta)$, $K(\delta)$, $L(\delta)$, $M(\delta)$, $N(\delta)$, $U(\delta)$ and $V^T(\delta)$.

Note that although optimized, in general the described procedure can be time-consuming depending on the size of the generalized plant P and the spatial dimension of $\boldsymbol{\Delta}$. Given the choice of δ used within this report, the latter problem does no longer represent an issue. Nonetheless, care must still be taken in choosing an appropriate sampling period when discretizing the continuous-time parameter-dependent generalized plant [87, 88] such that all operations can be done in a *real-time* manner. Moreover, based on the controller matrices at every time instant k, the control signal in (21), given as the output of an adaptive filter, also requires special attention towards implementation [33], yet this is outside the scope of the currently-presented material. This concludes **Appendix A**.

Appendix B: Definition of the ART 5 MW Reference Wind Turbine

The ART 5 MW is a VS-VP bottom-supported monopile reference offshore wind turbine based on the design of the National Renewable Energy Laboratory's reference wind turbine [48]. The turbine is depicted conceptually in Figure 53 and has been improved by the Energy Research Centre of the Netherlands [58].

The ART 5 MW is designed to operate under nominal gravity conditions, air densities of around ρ=1.226 [kg/m^3], water depths of around H_{wat}=20 [m] and water densities of approximately ρ_{wat}=1000 [kgm^3]. Within the current report, the turbine model has been used for control design and simulation purposes together with the reference control design tool ACT [52].

The following tables offer the main characteristics for the ART 5 MW subsystems, in accordance with both the presented information in **Chapter 2** and the corresponding definitions as part of ACT [52, 51], as well as the customized designed operational curve properties used throughout this report.

Figure 53: Conceptual View of the ART 5 MW Reference Wind Turbine

	Assigned Mathematical Notation	Numerical Value within ART 5 MW Turbine
Number of Blades	B	3 [blades]
Top-Relative Rotor Center	$[x, y, z]$	[-5,0,0] [m]
Rotor Cone Angle	Φ_{ROT}	-2.5 [deg]
Rotor Radius	R	64.14 [m]
Rotor Inertia	J_r	37960000 [kgm^2/rad^2]
Blade Root Radius	R_{BRoot}	1.5 [m]
Blade Mass	m_{bla}	17400 [kg]
Edgewise Natural Frequency	$\omega_{n,edge}^{blade}$	1.07 [Hz]
Edgewise Damping Ratio	ζ_{edge}^{blade}	0.0048 [a.u.]
Leadwise Natural Frequency	$\omega_{n,lead}^{blade}$	0.69 [Hz]
Leadwise Damping Ratio	ζ_{lead}^{blade}	0.0048 [a.u.]

Table 7: Main Rotor Characteristics for the ART 5 MW Wind Turbine

	Assigned Mathematical Notation	Numerical Value within ART 5 MW Turbine
Pure Delay	τ_{pt}	0.1 [s]
Natural Frequency	ω_{pt}	3.1831 [Hz]
Damping Ratio	ζ_{pt}	0.5 [a.u.]
Pitch Angle Constraints	$[\theta_{min}, \theta_{max}]$	[-90,90] [deg]
Pitch Speed Constraints	$[\dot{\theta}_{min}, \dot{\theta}_{max}]$	[-6,6] [deg/s]
Pitch Acceleration Constraints	$[\ddot{\theta}_{min}, \ddot{\theta}_{max}]$	[-12,12] [deg/s^2]

Table 8: Main Pitch Actuator Characteristics for the ART 5 MW Wind Turbine

	Assigned Mathematical Notation	Numerical Value within ART 5 MW Turbine
Tilt Angle	Θ_{dt}	5 [deg]
Torsional Stiffness	s_{dt}	2 [GNm/rad^2]
Torsional Natural Frequency	ω_n^{dt}	2.14 [Hz]
Torsional Damping Ratio	ζ^{dt}	0.03 [a.u.]
Generator/Fast Shaft Inertia	$J_{g/fs}$	534 [kgm^2/rad^2]
Coulomb Friction Torque	T_C	0 [Nm/rad]
Generalized Friction Torque Loss	T_T	0.0287 [a.u.]
Viscous Friction Torque Loss	T_V	0 [Nms/rad^2]

Table 9: Main Drivetrain Characteristics for the ART 5 MW Wind Turbine

	Assigned Mathematical Notation	Numerical Value within ART 5 MW Turbine
Generator Type	N/A	DFIG
Generator Inertia	J_g	534 [kgm^2/rad^2]
Generator Natural Frequency	ω_g	15.91 [Hz]
Generator Damping Ratio	ζ_g	0.7 [a.u.]
Generator Torque Constraints	$[T_{gen}^{min}, T_{gen}^{max}]$	[0,460] [kNm/rad]
Generator Electrical Losses	$T_{el,g}$	0.0287 [a.u.]

Table 10: Main Electrical Generator Characteristics for the ART 5 MW Wind Turbine

	Assigned Mathematical Notation	Numerical Value within ART 5 MW Turbine
Tower Top Height	H	110 [m]
Tower Base Diameter	Φ_{base}	6 [m]
Tower Top Diameter	Φ_{top}	3.8 [m]
Tower Top Equivalent Mass	m_t	520000 [kg]
Tower Top Equivalent Stiffness	s_t	1181200 [N/m]
Tower Top Equivalent Damping	d_t	31.34 [Ns/m]

Table 11: Main Support Structure Characteristics for the ART 5 MW Wind Turbine

	Assigned Mathematical Notation	Numerical Value within ART 5 MW Turbine
Rated Electrical Power	P_{rat}	5 [MW]
Rated Rotor Speed	$\Omega_{r,rat}$	12.1 [rpm]
Minimum Rotor Speed	$\Omega_{r,min}$	6 [rpm]
Maximum Rotor Speed	$\Omega_{r,max}$	15 [rpm]
Rated Wind Speed	v_{rated}	12.5 [m/s]
Cut-In Wind Speed	v_{cutin}	3 [m/s]
Cut-Out Wind Speed	v_{cutout}	25 [m/s]
Low Exclusion Wind Speed	$v_{excl,low}$	10.5 [m/s]
High Exclusion Wind Speed	$v_{excl,high}$	12.5 [m/s]

Table 12: Operation Characteristics for the ART 5 MW Wind Turbine

References

[1] T. Ackermann (Editor). *Wind Power in Power Systems*. John Wiley & Sons Ltd., Chichester, UK, 2005.

[2] Danish Energy Agency. Code for Practice for Loads and Safety of Wind Turbine Construction (DS472). Technical report, Danish Energy Agency, 1992.

[3] International Energy Agency. *Contributions of Renewables to Energy Security*. International Energy Agency (IEA), 2007.

[4] B.D.O. Anderson and J.B. Moore. *Optimal Filtering*. Dover Publications, New York, U.S.A., 2005.

[5] B.D.O. Anderson and J.B. Moore. *Optimal Control: Linear Quadratic Methods*. Dover Publications, New York, U.S.A., 2007.

[6] P. Apkarian and R.J. Adams. Advanced Gain-Scheduling Techniques for Uncertain Systems. *IEEE Transactions on Control Systems Technology*, 6(1):21–32, 1998.

[7] P. Apkarian and P. Gahinet. A Convex Characterization of Gain-Scheduled $\mathcal{H}_\infty$ Controllers. *IEEE Transactions on Automatic Control*, 40(5):853–864, 1995.

[8] P. Apkarian, P. Gahinet, and G. Becker. Self-Scheduled $\mathcal{H}_\infty$ Control of Linear Parameter-Varying Systems: A Design Example. *Automatica*, 31(9):1251–1261, 1995.

[9] P. Apkarian and H.D. Tuan. Parametrized LMIs in Control Theory. *SIAM Journal of Control and Optimization*, 38(4):1241–1264, 2000.

[10] American Wind Energy Association. *Wind Energy Basics*. American Wind Energy Association (EWEA), 2010.

[11] K.A. Ästrom and B. Wittenmark. *Computer-Controlled Systems: Theory and Design*. Dover Publications, New York, U.S.A., 2011.

[12] G. Balas. Linear Parameter-Varying Control and Its Application to Aerospace Systems. *Proceedings of the 2002 International Council of Aeronautical Sciences (ICAS) Congress*, 541:1–9, 2002.

[13] G. Balas. Linear, Parameter-Varying Control and Its Applications to a Turbofan Engine. *International Journal of Robust and Nonlinear Control*, 12:763–796, 2002.

[14] G. Balas, J.C. Doyle, K. Glover, A. Packard, and R. Smith. *μ-Analysis and Synthesis Toolbox: For Use with MATLAB*. The MathWorks, Natick, Massachusetts, 2001.

[15] L. Battisti. *Wind Turbines in Cold Climates*. Springer International Publishing, New York, 2015.

[16] A. Ben-Tal and A. Nemirovski. *Lecture Notes on Modern Convex Optimization: Analysis, Algorithms and Engineering Applications*. SIAM, Philadelphia, 2001.

[17] F.D. Bianchi, H. De Battista, and R.J. Mantz. *Wind Turbine Control Systems: Principles, Modelling and Gain Scheduling Design*. Springer-Verlag, London, 2007.

[18] S. Biswas, P. Taylor, and J. Salmon. A Model of Ice Throw Trajectories from Wind Turbines. *Wind Energy*, 15(1):889–901, 2012.

[19] S. Boyd, L. El Ghaoui, E. Feron, and V. Balakrishnan. *Linear Matrix Inequalities in System and Control Theory*. Springer-Verlag, Philadelphia, 1994.

[20] S. Boyd and L. Vandenberghe. *Convex Optimization*. Cambridge University Press, Cambridge, 2004.

[21] T. Burton, D. Sharpe, N. Jenkins, and E. Bossanyi. *Wind Energy Handbook*. John Wiley & Sons Ltd., Chichester, UK, 2001.

[22] G.C. Calafiore, F. Dabbene, and R. Tempo. Randomized Algorithms for Probabilistic Robustness with Real and Complex Structured Uncertainty. *IEEE Transactions on Automatic Control*, 45(12):2218–2335, 2000.

[23] International Electrotechnical Commission. Wind Turbines - Part 13: Measurement of Mechanical Loads (IEC 61400-13 TS). Technical report, International Electrotechnical Commission, 2001.

[24] International Electrotechnical Commission. Wind Turbines - Part 1: Design Requirements (IEC 61400-1). Technical report, International Electrotechnical Commission, 2005.

[25] International Electrotechnical Commission. Wind Turbines - Part 25: Communications for Monitoring and Control of Wind Power Plants (IEC 61400-25). Technical report, International Electrotechnical Commission, 2006.

[26] International Electrotechnical Commission. Wind Turbines - Part 22: Conformity Testing and Certification of Wind Turbines (IEC 61400-22 TS). Technical report, International Electrotechnical Commission, 2008.

[27] International Electrotechnical Commission. Wind Turbines - Part 3: Design of Offshore Wind Turbines (IEC 61400-3). Technical report, International Electrotechnical Commission, 2008.

[28] C. Courties and J. Bernussou. LPV Control by Dynamic Output Feedback. *Proceedings of the American Control Conference*, 23(5):2267–2271, 1999.

[29] M. Damgaard, J.K.F. Andersen, L.B. Ibsen, and L.V. Andersen. Natural Frequency and Damping Estimation of an Offshore Wind Turbine Structure. *Proceedings of the 22nd International Offshore and Polar Engineering Conference*, 2(1):300–307, 2012.

[30] M. Damgaard, J.K.F. Andersen, L.B. Ibsen, and L.V. Andersen. Time-Varying Dynamic Properties of Offshore Wind Turbines Evaluated by Modal Testing. *Proceedings of the 18th International Conference on Soil Mechanics and Geotechnical Engineering*, 1(1):93–97, 2013.

[31] C.E. de Souza and A. Trofino. Gain-Scheduled $\mathcal{H}_2$ Controller Synthesis for Linear Parameter Varying Systems via Parameter-Dependent Lyapunov Functions. *International Journal of Robust and Nonlinear Control*, 16(1):243–257, 2006.

[32] C.E. de Souza, A. Trofino, and J. de Oliveira. Parametric Lyapunov Function Approach to $\mathcal{H}_2$ Analysis and Control of Linear Parameter-Dependent Systems. *Proceedings of the IEEE Conference on Control Theory and Applications*, 21(3):501–508, 2003.

[33] P.S.R. Diniz. *Adaptive Filtering: Algorithms and Practical Implementation*. SIAM, New York, U.S.A., 2012.

[34] D. Duckwitz and M. Shan. A Survey on Control Concepts for the Reduction of Tower Loads (Conference Poster). *The Science of Making Torque From Wind (TORQUE 2012) Conference*, 2012.

[35] D. Duckwitz and M. Shan. Active Tower Damping and Pitch Balancing - Design, Simulation and Field Test. *The Science of Making Torque From Wind (TORQUE 2012) Conference*, 555(1):1–11, 2012.

[36] M. Etemaddar, M.O.L. Hansel, and T. Moan. Wind Turbine Aerodynamic Response Under Atmospheric Icing Conditions. *Wind Energy*, 17(1):241–265, 2014.

[37] E. Feron, V. Balakrishnan, S. Boyd, and L. El Ghaoui. Numerical Methods for $\mathcal{H}_2$-Related Problems. *Proceedings of the 1992 American Control Conference*, 4(1):2921–2922, 1992.

[38] B. Fischer and M. Shan. *A Survey on Control Methods for the Mitigation of Tower Loads*. Number Report No. 01/104256. Fraunhofer IWES - Institute for Wind Energy and Energy Systems Technology, 2013.

[39] T. Fischer, W. de Vries, P. Rainey, B. Schmidt, K. Argyriadis, and M. Kühn. Offshore Support Structure Optimization by Means of Integrated Design and Controls. *Wind Energy*, 15(1):99–117, 2012.

[40] B. Friedland. *Control System Design: An Introduction to State-Space Methods*. Dover Publications, New York, U.S.A., 2005.

[41] Y. Fujisaki, F. Dabbene, and R. Tempo. Probabilistic Design of LPV Control Systems. *Automatica*, 32(7):1007–1014, 2003.

[42] P. Gahinet, P. Apkarian, and M. Chilali. Affine Parameter-Dependent Lyapunov Functions and Real Parametric Uncertainty. *IEEE Transactions on Automatic Control*, 41(3):436–442, 1996.

[43] P. Gahinet, A. Nemirovski, A.J. Laub, and M. Chilali. The LMI Control Toolbox. *Proceedings of the IEEE Conference on Decision and Control*, 4(3):2038–2041, 1994.

[44] A. Ghaffari, M. Krstić, and S. Seshagiri. Power Optimization and Control in Wind Energy Conversion Systems using Extremum Seeking. *Proceedings of the 2013 Americal Control Conference*, 2(1):2241–2246, 2013.

[45] C. Hochart, G. Fortin, and J. Peron. Wind Turbine Performance under Icing Conditions. *Wind Energy*, 11(1):319–333, 2007.

[46] M. Homola, M.S. Virk, P.J. Nicklasson, and P.A. Sundsbø. Performance Losses Due to Ice Accretion for a 5 MW Wind Turbine. *Wind Energy*, 15(1):379–389, 2012.

[47] S.J. Johnson, C.P. van Dam, and D.E. Berg. *Active Load Control Techniques for Wind Turbines*. Number SAND2008-4809. SANDIA National Laboratories, 2008.

[48] J. Jonkman, S. Butterfield, W. Musial, and G. Scott. *Definition of a 5-MW Reference Wind Turbine for Offshore System Development*. Number NREL/TP-500-38060. NREL, 2009.

[49] J. Kaimal, J. Wyngaard, Y. Izumi, and O. Coté. Spectral Characteristics of Surface Layer Turbulence. *Quarterly Journal of Royal Meteorology Society*, 98(4):563–598, 1972.

[50] S. Kanev. *Control Methods for Increasing Power Production under Model Uncertainty*. Number ECN-X-13-113. ECN, 2013.

[51] S. Kanev. *Functional Description of ACT Controller*. Number ECN-X-13-077. ECN, 2013.

[52] S. Kanev, F. Savenije, D. Wouters, and W. Engels. *Control Design Tool Upgrade (CDTup) Project: Confidential Final Report*. Number ECN-X-12-086. ECN, 2012.

[53] S. Kanev and T. van Engelen. Wind Turbine Extreme Gust Control. *Wind Energy*, 13(1):18–35, 2010.

[54] S. Kanev, T. van Engelen, W. Engels, X. Wei, J. Dong, and M. Verhaegen. *Sustainable Control: A New Approach to Operate Wind Turbines*. Number ECN-E-12-028. ECN, 2012.

[55] H.K. Khalil. *Nonlinear Systems*. Prentice Hall, New Jersey, 2001.

[56] A.G. Kraj and E.L. Bibeau. Phases of Icing on Wind Turbine Blades Characterized by Ice Accumulation. *Renewable Energy*, 35(2):966–972, 2010.

[57] D.J. Leith and W.E. Leithead. Survey of Gain-Scheduling Analysis and Design. *International Journal of Control*, 73:1001–1025, 1999.

[58] C. Lindenburg. *Comparison of PHATAS Versions and the Wind Turbine Module*. Number ECN-E-11-066. ECN, 2011.

[59] Germanischer Lloyd. Regulation of the Certification of Wind Energy Conversion Systems, Rules and Regulations IV: Non-Marine Technology (Part I). Technical report, Germanischer Lloyd, 2003.

[60] N. Luo, Yolanda Vidal, and L. (Editors) Acho. *Wind Turbine Control and Monitoring*. Springer International Publishing, New York, 2014.

[61] A. Lyapnuov. The General Problem of the Stability of Motion. Doctoral Dissertation, University of Kharkiv, 1892.

[62] P.A. Lynn. *Onshore and Offshore Wind Energy*. John Wiley & Sons Ltd., Chichester, UK, 2012.

[63] J.F. Manwell, J.G. McGowan, and A.L. Rogers. *Wind Energy Explained: Theory, Design and Application*. John Wiley & Sons Ltd., West Sussex, England, 2009.

[64] S. Mesic, V. Verdult, M. Verhaegen, and S. Kanev. Estimation and Robustness Analysis of Actuator Faults Based on Kalman Filtering. *Proceedings of the 5th Symposium of Fault Detection, Supervision and Safety for Technical Processes (SAFEPROCESS 2003)*, 3(2):34–52, 2003.

[65] Yu. Nesterov and A. Nemirovski. *Interior-Point Polynomial Methods in Convex Programming*. SIAM, Philadelphia, 1994.

[66] Energy Research Centre of the Netherlands (ECN). *Design for Reliable Power Performance (D4REL) Project Proposal*. Dutch Top Consortium for Knowledge and Innovation in Offshore Wind (TKI Wind op Zee), 2014.

[67] Y. Oishi and H. Kimura. Randomized Algorithms to Solve Parameter-Dependent Linear Matrix Inequalities and their Computational Complexity. *Transactions of the IEEE Conference on Decision and Control*, 5(2):2025–2030, 2001.

[68] K.Z. Østergaard, P. Brath, and J. Stoustrup. Estimation of Effective Wind Speed. *Proceedings of the Conference of Making Torque from Wind*, 1(2):123–132, 2007.

[69] P. Ragan and L. Manuel. Comparing Estimates of Wind Turbine Fatigue Loads Using Time-Domain and Spectral Methods. *Wind Engineering*, 31(2):83–99, 2007.

[70] REN21. *Renewables 2014: Global Status Report*. Renewable Energy Policy Network for the 21st Century (REN21), 2014.

[71] Erica A. Rendon and L. Manuel. Long-Term Loads for a Monopile-Supported Offshore Wind Turbine. *Wind Energy*, 17(1):209–223, 2014.

[72] P. Rosas. Dynamic Influences of Wind Power in Wind Power Systems. Doctoral Dissertation, Technical University of Denmark, 2003.

[73] W.J. Rugh and J.S. Shamma. Research on Gain Scheduling. *Automatica*, 36:1401–1425, 2000.

[74] T. Samad and A.M. Annaswamy (Editors). The Impact of Control Technology: Overview, Success Stories and Research Challenges. Technical report, IEEE Control Systems Society, 2011.

[75] S. Sastry. *Nonlinear Systems: Analysis, Stability and Control*. Springer-Verlag, New York, 1999.

[76] C. Scherer and S. Weiland. *Linear Matrix Inequalities in Control*. Lecture Notes from the Dutch Institute for Systems and Control (DISC), 2008.

[77] C.W. Scherer. Robust Generalized $\mathcal{H}_2$ Control for Uncertain and LPV Systems with General Scalings. *Proceedings of the IEEE Conference on Decision and Control*, 34(4):3970–3975, 1996.

[78] K. Selvam, S. Kanev, J.W. van Wingerden, T. van Engelen, and M. Verhaegen. Feedback-Feedforward Individual Pitch Control for Wind Turbine Load Reduction. *International Journal of Robust and Nonlinear Control*,

19(1):72–91, 2009.

[79] J. Shamma and M. Athans. Analysis of Gain Scheduled Control for Nonlinear Plants. *IEEE Transactions on Automatic Control*, 35(8):898–907, 1990.

[80] J. Shamma and M. Athans. Guaranteed Properties of Gain Scheduled Control for Linear Parameter-Varying Plants. *Automatica*, 27(3):559–564, 1991.

[81] J. Shamma and M. Athans. Gain Scheduling: Potential Hazards and Possible Remedies. *IEEE Control Systems Magazine*, 12(3):101–107, 1992.

[82] M. Shan, J. Jacobsen, and S. Adelt. Field Testing and Practical Aspects of Load Reducing Pitch Control Systems for a 5 MW Offshore Wind Turbine. *Proceedings of the 2013 European Wind Energy Association Event*, 2(1):632–641, 2013.

[83] S. Skogestad and I. Postlethwaite. *Multivariable Feedback Control: Analysis and Design*. John Wiley & Sons Ltd., West Sussex, England, 2007.

[84] A.G. Sparks. Analysis of Affinely Parameter-Varying Systems using Parameter-Dependent Lyapunov Functions. *Proceedings of the IEEE Conference on Decision and Control*, 1(2):990–991, 1997.

[85] B. Tammelin, M. Cavaliere, H. Holttinen, C. Morgan, H. Seifert, and K Sänti. *Wind Energy Production in Cold Climate (WECO) Technical Report*. Number JOR3-CT95-0014. Finnish Meteorological Institute, 1998.

[86] R. Tempo, E.W. Bai, and F. Dabbene. Probabilistic Robustness Analysis: Explicit Bounds for the Minimum Number of Samples. *Systems and Control Letters*, 30:237–242, 1997.

[87] R. Tóth, M. Lovera, P.S.C. Heuberger, M. Corno, and P.M.J. Van den Hof. *On the Discretization of Linear Fractional Representations of LPV Systems*. Number R-11-037. TU Delft, 2011.

[88] R. Tóth, M. Lovera, P.S.C. Heuberger, M. Corno, and P.M.J. Van den Hof. On the Discretization of Linear Fractional Representations of LPV Systems. *IEEE Transaction on Control Systems Technology*, 20(6):1473–1489, 2012.

[89] E. van der Hooft, T. van Engelen, J. Pierik, and P. Schaak. *Real-Time Process Simulator for Evaluation of Wind Turbine Systems: Modelling and Implementation*. Number ECN-E-07-046. ECN, 2007.

[90] I. van der Hoven. Power Spectrum of Horizontal Wind Speed in the Frequency Range from 0.0007 to 900 Cycles per Hour. *Journal of Meteorology*, 14(2):160–164, 1957.

[91] J. van der Temple, M.B. Zaaijer, and H. Subroto. The Effects of Scour on the Design of Offshore Wind Turbines. *Third International Conference on Marine Renewable Energy*, 4(2):53–62, 2004.

[92] T. van Engelen. Design Model and Load Reduction Assessment for a Multi-Rotational Mode Individual Pitch Control (Higher Harmonics Control). *Proceedings of the European Wind Energy Conference*, 3(2):1–8, 2006.

[93] Det Norske Veritas. Design and Manufacture of Wind Turbine Blades Blades, Offshore and Onshore Wind Turbines (DNV-JS-102). Technical report, Det Norske Veritas, 2006.

[94] J. Walker and N. Jenkins. *Wind Energy Technology*. John Wiley & Sons Ltd., Chichester, UK, 1997.

[95] A. P. White, G. Zhu, and J. Choi. *Linear Parameter-Varying Control for Engineering Applications*. Springer-Verlag, London, 2013.

[96] J.C. Willems. Dissipative Dynamical Systems Part I: General Theory. *Archive for Rotational Mechanics and Analysis*, 45(5):321–351, 1972.

[97] J.C. Willems. Dissipative Dynamical Systems Part II: Linear Systems with Quadratic Supply Rates. *Archive for Rotational Mechanics and Analysis*, 45(5):352–393, 1972.

[98] Jennifer C. Wilson and M. Elliott. The Habitat-Creation Potential of Offshore Wind Farms. *Wind Energy*, 12(1):203–212, 2009.

[99] F. Wu, X.H. Yang, A. Packard, and G. Becker. Induced $\mathcal{L}_2$-norm Control for LPV Systems with Bounded Parameter Variation Rates. *International Journal of Robust and Nonlinear Control*, 6:983–998, 1996.

[100] W. Xie. $\mathcal{H}_2$ Gain-Scheduled State-Feedback for LPV System with New LMI Formulation. *Proceedings of the IEEE Conference on Control Theory Applications*, 152(6):693–697, 2005.

[101] K. Zhou, J.C. Doyle, and K. Glover. *Robust and Optimal Control*. Prentice Hall, Upper Saddle River, New Jersey, 1996.

ECN

Westerduinweg 3
1755 LE Petten
The Netherlands

P.O. Box 1
1755 ZG Petten
The Netherlands

T: +31 88 5154949
info@ecn.nl
www.ecn.nl